UNIVERSITAT POLITECNICA DE CATALUNYA

ENERGY PROCESSING BY MEANS OF POWER GYRATORS

By

ANGEL CID-PASTOR

B. Eng. Rovira i Virgili University, Tarragona, Spain, 1999
M. Eng. Rovira i Virgili University, Tarragona, Spain, 2002
D.E.A. Institut National des Sciences Appliquées, Toulouse, France 2003

THESIS

Submitted as a partial fulfillment of the requirements for the degree of Doctor of Philosophy in Electronics Engineering in the Department of Electronics Engineering of the Technical University of Catalonia (UPC) at Barcelona, 2005

Thesis Supervisor: LUIS MARTINEZ-SALAMERO

Barcelona, Spain

Als meus pares, Angel i Pilar

A la meua companya Laura

ACKNOWLEDGEMENT (In Catalan)

En primer lloc, vull expressar la meua gratitud a Luis Martinez Salamero, director d'aquesta tesi, pels seus consells, orientació, per tot el que he après treballant al seu costat i per la seua generositat.

Gràcies també a Francesc Guinjoan Gispert membre del Department d'Enginyeria Electrònica de la Universitat Politècnica de Catalunya per la tutoria d'aquesta tesi. Igualment, gràcies a Corinne Alonso del *Laboratoire d'Analyse et d'Architecture des Systèmes* de Toulouse i a Jean Alzieu i Guy Schweitz d'*Electricité de France R&D* per permetre'm realitzar aquest treball de recerca en les millors condicions.

Destacaré aquí la professionalitat de tots els professors del Departament d'Enginyeria Electrònica Elèctrica i Automàtica de l'Escola Tècnica Superior d'Enginyeria de l'Universitat Rovira i Virgili que m'han proporcionat els coneixements necessaris per dur a terme aquesta tesi.

Un record especial per als membres del Grup d'Automàtica i Electrònica Industrial de l'ETSE-URV amb els quals vaig tenir la sort de treballar com a tècnic de laboratori entre els anys 1999 i 2002.

Vull agrair l'ajuda i col·laboració que m'han ofert Bruno Estibals, Alain Salles i Fairid Boudjellal i el recolzament de tots els companys del LAAS-CNRS. A tots, moltes gràcies.

TABLE OF CONTENTS

TABLE OF CONTENTS (Continued)

LISTE OF TABLES

LIST OF FIGURES

LIST OF ABBREVIATIONS

AC	Alternating Current
BIF	Buck converter with Input Filter
BOF	Boost converter with Output Filter
DC	Direct Current
EMI	Electromagnetic Interference
MPPT	Maximum Power Point Tracking
POPI	Power Output = Power Input
PV	Photovoltaic
PWM	Pulse Width Modulation

ABSTRACT

In this thesis, a systematic approach to the synthesis of power gyrators is presented. Based on this approach, several gyrator structures can be generated and classified. Each of these gyrators has its own features and is suitable of different applications.

From a circuit standpoint, a power gyrator is a two-port structure characterized by any of the following two set of equations

$$\begin{aligned} I_1 &= gV_2 \\ I_2 &= gV_1 \end{aligned} \tag{1}$$

$$\begin{aligned} V_1 &= rI_2 \\ V_2 &= rI_1 \end{aligned} \tag{2}$$

Where I_1, V_1, and I_2, V_2 are DC values of current and voltage at input and output ports respectively and g (r) is the gyrator conductance (resistance). In this thesis, power gyrator structures are classified by the manner they transform an excitation source at the input port into its dual representation at the output port. Based on this classification, there exist three types of power gyrators: 1) power gyrators of type G, 2) power gyrators of type G with controlled input current and 3) power gyrators of type R. Categories 1 and 2 are the two possible synthesis solutions to the set of equations (1) while category 3 corresponds to the synthesis solution of (2).

Thus far, no systematic works have been done starting at the definition equations and ending at the experimental verification. In this thesis, the analysis and design for the disclosed power gyrators are presented. The analysis covers exhaustingly the study of both static and dynamic behavior of the reported power gyrators. These power gyrators presented can be considered as canonical structures for power processing.

Thus, some basic power processing functions done by the presented power gyrators are reported. Namely, voltage to current conversion, current to voltage conversion, impedance matching and voltage regulation.

The performance characteristics of a power gyrator depend not only on the circuit topology but also depend on the converter control operation.

Hence, two main control schemes are investigated, namely, sliding-mode control schemes and zero-dynamics-based PWM nonlinear control. Therefore, the proposed gyrator structures can operate indistinctly at constant or at variable switching frequency.

In addition, experimental and computer simulation results of the power gyrators presented are given in order to verify the theoretical predictions.

CHAPTER 1

1 INTRODUCTION

INTRODUCTION

The gyrator is an ideal circuit element that, unlike the other four elements (resistor, inductor, capacitor and ideal transformer) that directly arise from modeling electromagnetic phenomena, was originally postulated, without immediate experimental verification, as the most simple linear, passive and non-reciprocal element. The term gyrator was introduced by Tellegen [1] who developed the gyrator theory and designed possible realizations without achieving feasible solutions. It was Hogan [2] the first to design a device that operating at microwave frequencies approximated the behavior of an ideal gyrator. The physical principle of the first gyrator was the Faraday rotation in biased ferrites, solution essayed previously by Tellegen unsuccessfully at low frequencies where the non-reciprocal properties of ferrites are not observed. Some years later, the non-reciprocal behavior was obtained by means of active elements, this leading to the gyrator realization at low frequencies [3]. Since then, the use of gyrators at low frequencies is mainly constrained to active filtering due to its facility to emulate inductors with high quality factor [4]-[6].

The introduction of the gyrator concept in power processing circuits is due to Singer [7]-[9] who related the power gyrator to a general class of circuits named POPI (power output = power input) describing the ideal behavior of a switched-mode power converter. Later, the notion of power gyrator was used to model an inverse dual converter [10], and double bridge converters were reported to naturally behave as gyrators [11]. More recently, a gyrator realization based on the combination of a transmission line and a switching network was reported in [12].

On the other hand, the increasing importance of modularity in many applications of power electronics like, for example, UPS realizations or photovoltaic installations, leads one way or another to connect in parallel the output ports of power converters. Paralleling switching converters increases the power processing capability and improves the reliability since stresses are better distributed and fault tolerance is guaranteed. In this context, a power gyrator with good static and dynamic performances could be a useful canonical element in certain cases of converters paralleling. This hypothesis is based on the gyrator nature, i.e., on the fact that the output current is proportional to the input voltage, and that, in turn, the input current is proportional to the output voltage with the same proportionality factor. However, selecting a power converter for an eventual transformation into a power gyrator is not a simple task since, so far, there are no systematic studies establishing the most appropriate switching structure in terms of static and dynamic behavior. As a matter of fact, in Singer's paper [8] there are some important hints that will be used in this thesis. For example, in [8] the possibility of implementing a power gyrator using a buck converter with input filter (BIF) operating in a hysteretic mode is suggested but the corresponding analysis and design are not carried out. Also, in [8], the experimental results of a PWM Cuk push-pull power stage operating as a gyrator for dc-ac conversion are shown but no parametric design criteria are given. This sparse information involving structures and applications required a new interpretation almost twenty years later using today's well-known nonlinear analytical tools that were mostly unknown within the power electronics community at the end of the eighties. Thus, the buck converter with input filter (BIF) and the Cuk converter will be systematically analyzed in this thesis by means of sliding-mode approach and by means of nonlinear PWM operation with the constraints imposed by the desired behavior of the gyrator.

As above stated, the research in power converter paralleling could benefit from the existence of reliable power gyrators transforming input voltage sources into output current sources. However, the definition of such goal requires a top to down analysis covering exhaustingly all the steps going from the definition to the experimental results without disregarding all possible design solutions.

Therefore, in this thesis, a unified approach to the synthesis of a power gyrators is proposed. Based on the power gyrator equations, it will be shown that two main families of power gyrators can be defined, i.e., G-gyrators and R-gyrators as they have been classified in the thesis. Moreover, it will also shown that the synthesis procedure implicitly implies a classification mechanism through which a new set of power structures can be generated. These new power gyrators can be thought as canonical elements for power processing architectures.

In Chapter 2, a systematic approach to the synthesis of power gyrators will be described. Power gyrators will be classified by the manner in which a voltage (current) source at the input of the two-port is transformed into a current (voltage) source at the output port. Based on this classification, there exist three types of power gyrators: 1) G-gyrators; 2) G-gyrators with controlled input current; 3) R-gyrators. It will be shown that the buck converter with input filter and the Cuk converter can exhibit stable gyrator characteristics of G-type operating either at constant or variable switching if damping networks are inserted and certain parametric conditions are satisfied. It will be also demonstrated that a boost converter with output filter (BOF) can behave either at constant or variable switching frequency as a power R-gyrator with stable dynamics without damping network compensation. In addition, BIF, BOF and Cuk converter are also shown to exhibit stable G-gyrator characteristics with controlled input current at either constant or variable switching frequency without damping network compensation. A final conclusion of the synthesis is the notion of semi-gyrator and the fact that a buck converter and a boost converter illustrate the most simple examples of stable semigyrators of type G and R respectively.

In Chapter 3, the realization of electronic functions in power processing by means of power gyrators will be presented. These functions are classified in two main categories, that is to say, current addition and impedance matching. It will be shown that G-gyrators are the canonical elements to parallel the output ports of power stages and that they will make possible different types of current distribution as, for example, democratic current sharing or master-slave current sharing. In addition, it will be demonstrated that the i-v conversion can be efficiently performed by means of gyrators of R-type. Combining several g-gyrators in parallel whose resulting output current is transformed into an output voltage by means of a gyrator of R-type will illustrate the most simple gyrator-based electric architecture for energy processing. In addition, the impedance matching is focused on the maximum power point tracking (MPPT) in photovoltaic arrays using power gyrators. It will be demonstrated that G-gyrators and G-gyrators with controlled input current can be used to solve the MPPT problem with similar efficiency to that of conventional solutions based on the DC-transformer approach.

In Chapter 4, the voltage regulation by means of power gyrators will be investigated. It will be demonstrated that the voltage regulation can be individually performed by only one gyrator and that it can be also carried out by means of the parallel connection of power gyrators of type G. Therefore a dynamic model of a gyrator-based voltage switching regulator will be presented. Based on this model, the feedback loop to ensure voltage regulation will be designed. The

problem of stability in a voltage regulation scheme based on the parallel connection of multiple G-gyrators will be also investigated in this chapter. The performance characteristics of a voltage regulator based either on a single gyrator or on the parallel connection of multiple G-gyrators will be derived and a design procedure as well as experimental results will be given to confirm the analytical work.

The summary and possible future work related to this thesis will be given in Chapter 5.

CHAPTER 2

2 SYNTHESIS OF POWER GYRATORS

2.1 Introduction

The objective of the synthesis is to design a two-port structure characterized by the following equations

$$I_1 = gV_2 \tag{2.1}$$

$$I_2 = gV_1 \tag{2.2}$$

where I_1, V_1, and I_2, V_2 are DC values of current and voltage at input and output ports respectively, and g is the gyrator conductance.

Equations (2.1)-(2.2) define a power gyrator of type G which can be represented by the two-port configuration of figure 2.1

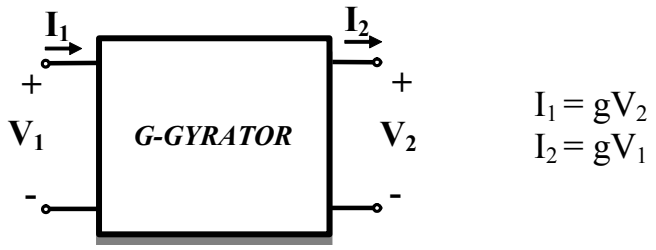

Fig. 2.1 Representation of a power gyrator of type G as a two-port

Note that equations (2.1)-(2,2) imply that the DC power absorbed at the input, i.e., V_1I_1 equals the DC power transfer to the output, i.e., V_2I_2.

Similarly, it will be a synthesis goal to find a two-port structure defined by the equations

$$V_1 = rI_2 \tag{2.3}$$

$$V_2 = rI_1 \tag{2.4}$$

where r is the gyrator resistance.

Equations (2.3)-(2.4) define a power gyrator of type R which is represented by the two-port configuration of Fig. 2.2.

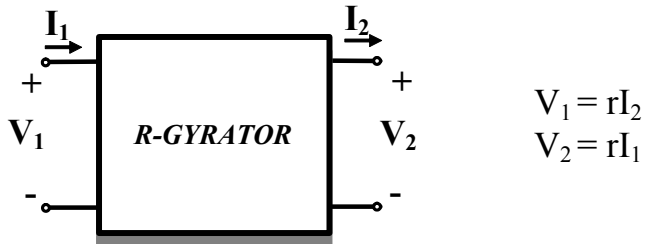

Fig. 2.2 Representation of a power gyrator of type R as a two port

From (2.3)-(2.4), it can also be deduced that the DC power output equals the DC power input.

The fact of preserving the DC power suggest that both types of gyrators should be synthesized by means of DC-to-DC switching converters which are POPI [1] structures [7]. To obtain the two-port behavior given by either equations (2.1)-(2.2) or (2.3)-(2.4) in a switching converter is not a simple task. Although variables V_1, I_1, V_2, I_2 can be straightforward identified as the steady-state averaged values of the corresponding current and voltage variables at converter input and output ports, such steady-states must be stable. In other words, they must be reachable after a stable start-up from zero initial conditions and remain bounded after the introduction of input source variations or load perturbations. Hence, the search of the appropriate switching structures and their corresponding control that eventually can result in stable steady-behaviour with G-gyrator or R-gyrator characteristics will be presented in this chapter.

2.2 Power gyrator definition

In the field of signal processing a two-port gyrator can be indistinctly described by its admittance parameters "*y*" or by its impedance parameters "*z*". Thus, a single physical circuit can be represented by two family of parameters due to the following equivalence

$$y = z^{-1} \tag{2.5}$$

where *y* and *z* are respectively given by

$$y = \begin{bmatrix} 0 & -g \\ g & 0 \end{bmatrix} \tag{2.6}$$

$$z = \begin{bmatrix} 0 & r \\ -r & 0 \end{bmatrix} \tag{2.7}$$

and $g = r^{-1}$

Therefore, the description in terms of one or other family of parameters depends on the circuit context in which the gyrator is involved and, therefore, on the analysis requirements.

On the contrary, in power processing, the synthesis of gyrators based on switching converters introduces some constraints in the design process which eliminates the versatility of the signal-processing gyrators. These constraints are imposed by the final goal that is expected by using a power gyrator, namely, the conversion of an input voltage source into a current output source and vice-versa as shown in Figs. 2.3 and 2.4.

[1] Two-port circuits in which DC Power output = DC Power input

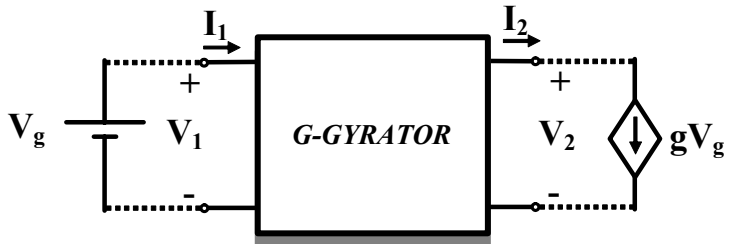

Fig. 2.3 Voltage-current conversion by means of a G-gyrator

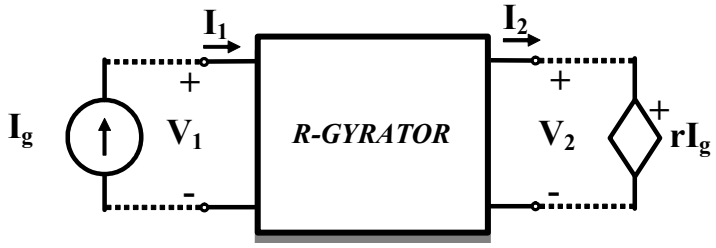

Fig. 2.4 Current-voltage conversion by means of a R-gyrator

It will be shown next that our definition of G-gyrator implies the presence of a series inductor at the input port. Such G-gyrator couldn't be excited by a current source, as in Fig. 2.4. Note that in power electronics most current sources are synthesized by means of the series connection of a voltage source and an inductor and, therefore in Fig. 2.4, two inductors would be in series at the input port, this violating the principle of compatibility in the synthesis of power converters. As a consequence, power gyrators of type G and R are different structures and their main roles, i.e., voltage to current or current to voltage conversion are not interchangeable.

2.2.1 Power gyrator of type G

Imposing equations (2.1)-(2.2) at the ports of a switching converter can be obtained by the insertion of an appropriate feedback control which can operate at variable or at fixed switching frequency. The synthesis of both cases is described in the next sections.

2.2.1.1 Power gyrator of type G with variable switching frequency

The objective of the G-gyrator synthesis is to find a switching structure characterized by the equations (2.1)-(2.2). Such equations define a power gyrator of type G which can be represented by the block diagram of Fig. 2.5. It consists of a switching converter which is controlled by means of a sliding-mode regulation loop whose switching surface is given by $S(x) = i_2 - gv_1$. In steady-state $S(x) = 0$, i.e., $I_2 = gV_1$ which automatically implies $I_1 = gV_2$, since the converter in

Fig. 1 is ideal and therefore is a POPI structure. Note that imposing a sliding-mode regime to the output current requires i_2 to be a continuous function of time [13], which implies the existence of a series inductor at the output port. On the other hand, in order to minimize EMI levels, a pulsating current will not be allowed at the input port and therefore the power G-gyrator will also require a series inductor at the input port. The most simple converters with such constraints at both ports are of fourth order, namely buck with input filter (BIF), boost with output filter (BOF), Cuk converter, and Cuk converter with galvanic isolation as illustrated in Fig. 2.6.

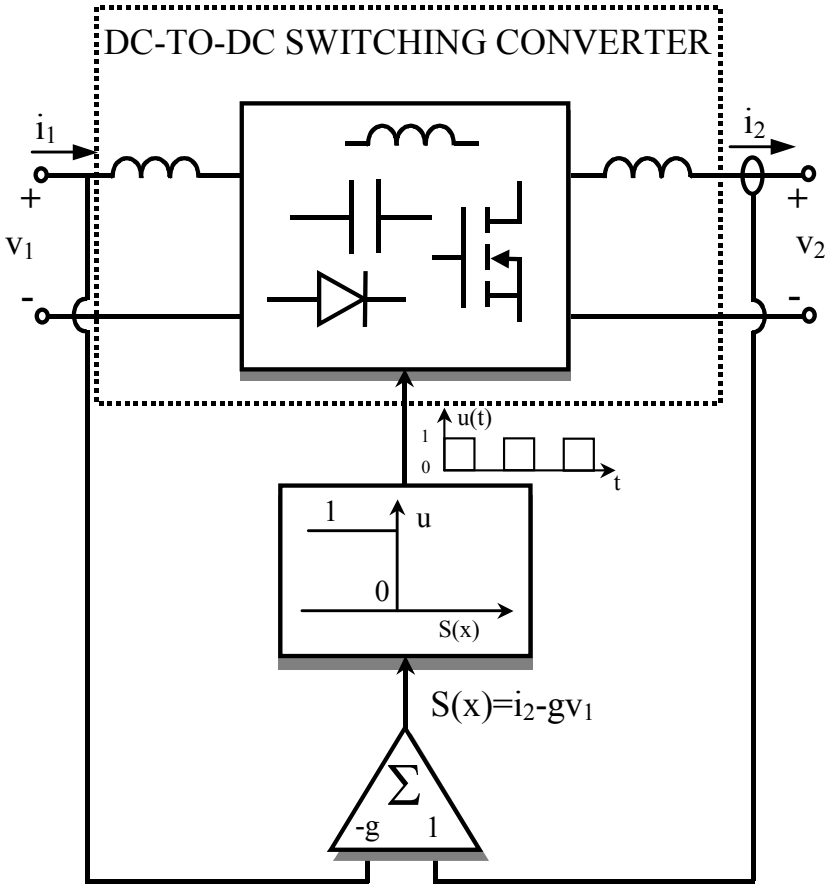

Fig. 2.5 Block diagram of a dc-to-dc switching regulator operating in sliding-mode with G-gyrator characteristics.

It has to be remarked that the presence of a comparator in the feedback loop of the switching regulator of Fig. 2.5 will result in a variable switching frequency which characterizes the sliding regimes.

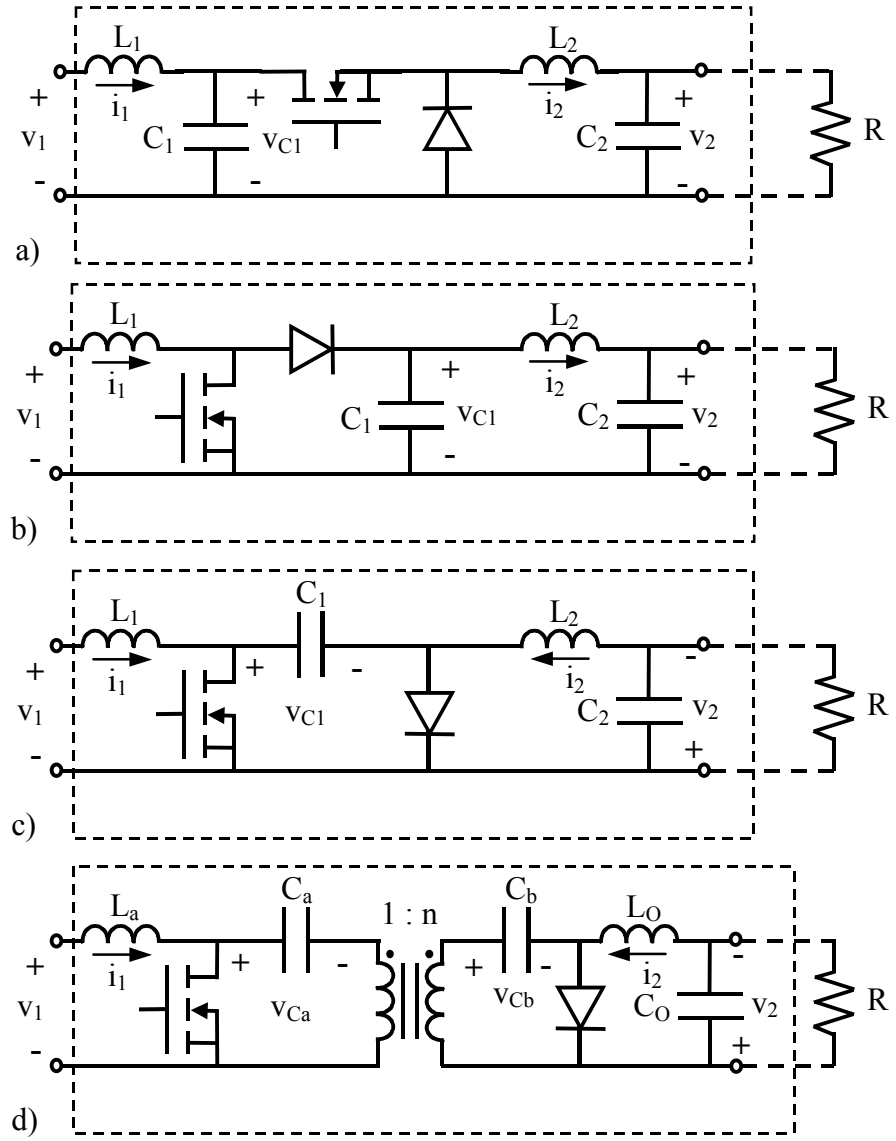

Fig. 2.6 Fourth order converters with non-pulsating input and output currents a) buck converter with input filter b) boost converter with output filter c) Cuk converter d) Cuk converter with galvanic isolation

The next step in our synthesis consists in the analysis in sliding-mode, under the constraints shown in Fig. 2.5, of each converter depicted in Fig. 2.6 except the Cuk converter with galvanic isolation whose complexity has deserved a complementary study within the frame of the research done in this thesis [30].

2.2.1.1.1 Analysis of BIF converter as a power G-gyrators with variable switching frequency

In the continuous conduction mode, the BIF converter has only one structural change during the switching period and therefore it can be represented by two piecewise-linear vector differential equations as follows

$$\dot{x} = A_1 x + B_1 \qquad \text{during } T_{ON} \tag{2.8}$$

$$\dot{x} = A_2 x + B_2 \qquad \text{during } T_{OFF} \tag{2.9}$$

where $x = [\, i_1,\, i_2,\, v_{C1},\, v_2 \,]^+$ is the state vector and matrices A_1, B_1, A_2, B_2 are given by

$$A_1 = \begin{bmatrix} 0 & 0 & -1/L_1 & 0 \\ 0 & 0 & 1/L_2 & -1/L_2 \\ 1/C_1 & -1/C_1 & 0 & 0 \\ 0 & 1/C_2 & 0 & -1/RC_2 \end{bmatrix} \quad B_1 = \begin{bmatrix} V_g/L_1 \\ 0 \\ 0 \\ 0 \end{bmatrix}$$

$$A_2 = \begin{bmatrix} 0 & 0 & -1/L_1 & 0 \\ 0 & 0 & 0 & -1/L_2 \\ 1/C_1 & -0 & 0 & 0 \\ 0 & 1/C_2 & 0 & -1/RC_2 \end{bmatrix} \quad B_2 = \begin{bmatrix} V_g/L_1 \\ 0 \\ 0 \\ 0 \end{bmatrix} \tag{2.10}$$

where it has been assumed $v_1 = V_g$.

Equations (2.8) and (2.9) can be combined in only one bilinear expression

$$\dot{X} = (A_1 X + B_1)\,u + (A_2 X + B_2)(1-u) \tag{2.11}$$

where u=1 during T_{ON} and u=0 during T_{OFF}

Equation (2.11) can be expressed as follows

$$\dot{X} = A_2 X + B_2 + (A_1 - A_2)\,X\,u + (B_1 - B_2)\,u \tag{2.12}$$

From (2.10) and (2.12), the following set of differential equations is derived:

$$\begin{aligned} \frac{di_1}{dt} &= \frac{-v_{C1}}{L_1} + \frac{v_g}{L_1} \\ \frac{di_2}{dt} &= u\frac{v_{C1}}{L_2} - \frac{v_2}{L_2} \\ \frac{dv_{C1}}{dt} &= \frac{i_1}{C_1} - \frac{u}{C_1} i_2 \\ \frac{dv_{C2}}{dt} &= \frac{i_2}{C_2} - \frac{v_2}{RC_2} \end{aligned} \tag{2.13}$$

Assuming $S(x)=i_2-gVg$ as sliding surface and imposing the invariance conditions [14] $S(x)=0$ and $\frac{dS}{dt}=0$ in (2.14) lead to the following expression of the equivalent control $u_{eq}(x)$

$$u_{eq}(x)=\frac{v_2}{v_{C1}} \tag{2.14}$$

Now, the discrete variable u is substituted by a continuous variable $u_{eq}(x)$ which can take all the values between 0 and 1. This variable $u_{eq}(x)$ represents the control law that describes the behaviour of the system restricted to the switching surface where the system motion takes place on the average. Therefore, $u_{eq}(x)$ is bounded by the minimum and maximum values of u

$$0<u_{eq}(x)<1 \tag{2.15}$$

Substituting u by $u_{eq}(x)$ in (2.13) and taking into account the constraint $i_2=gV_g$ imposed by the switching surface will result in the following ideal sliding dynamics:

$$\frac{di_1}{dt}=\frac{-v_{C1}}{L_1}+\frac{V_g}{L_1}=g_1(x) \tag{2.16}$$

$$\frac{dv_{C1}}{dt}=\frac{i_1}{C_1}-\frac{v_2}{v_{C1}}\frac{gV_g}{C_1}=g_2(x) \tag{2.17}$$

$$\frac{dv_{C2}}{dt}=\frac{gV_g}{C_2}-\frac{v_2}{RC_2}=g_3(x) \tag{2.18}$$

The coordinates of the equilibrium point $x^*=[I_1,I_2,V_{C1},V_2]^+$ are given by

$$x^*=\left[g^2RV_g,\ gV_g,V_g,gV_gR\right]^+ \tag{2.19}$$

Note that

$$I_1=gV_2 \tag{2.20}$$

$$I_2=gV_g \tag{2.21}$$

Expressions (2.20) and (2.21) define the g-gyrator characteristics in steady-state.

On the other hand, from (2.14) and (2.19), the expression of the equivalent control in the equilibrium point $u_{eq}(x^*)$ results in

$$u_{eq}(x^*)=gR \tag{2.22}$$

which is bounded by the minimum and maximum values of u

$$0<gR<1 \tag{2.23}$$

The ideal sliding dynamics given by equations (2.16)-(2.18) is nonlinear. In order to study the stability of the system, equations (2.16)-(2.18) will be linearized around the equilibrium point x^*. The corresponding Jacobian matrix J can be expressed as follows

$$J=\begin{bmatrix} \left.\frac{\partial g_1}{\partial i_1}\right|_{x^*} & \left.\frac{\partial g_1}{\partial v_{C1}}\right|_{x^*} & \left.\frac{\partial g_1}{\partial v_2}\right|_{x^*} \\ \left.\frac{\partial g_2}{\partial i_1}\right|_{x^*} & \left.\frac{\partial g_2}{\partial v_{C1}}\right|_{x^*} & \left.\frac{\partial g_2}{\partial v_2}\right|_{x^*} \\ \left.\frac{\partial g_3}{\partial i_1}\right|_{x^*} & \left.\frac{\partial g_3}{\partial v_{C1}}\right|_{x^*} & \left.\frac{\partial g_3}{\partial v_2}\right|_{x^*} \end{bmatrix} \tag{2.24}$$

where

$$\begin{array}{lll} \left.\frac{\partial g_1}{\partial i_1}\right|_{x^*}=0 & \left.\frac{\partial g_1}{\partial v_{C1}}\right|_{x^*}=\frac{-1}{L_1} & \left.\frac{\partial g_1}{\partial v_2}\right|_{x^*}=0 \\ \left.\frac{\partial g_2}{\partial i_1}\right|_{x^*}=\frac{1}{C_1} & \left.\frac{\partial g_2}{\partial v_{C1}}\right|_{x^*}=\frac{g^2R}{C_1} & \left.\frac{\partial g_2}{\partial v_2}\right|_{x^*}=\frac{-g}{C_1} \\ \left.\frac{\partial g_3}{\partial i_1}\right|_{x^*}=0 & \left.\frac{\partial g_3}{\partial v_{C1}}\right|_{x^*}=0 & \left.\frac{\partial g_3}{\partial v_2}\right|_{x^*}=\frac{-1}{RC_2} \end{array} \tag{2.25}$$

The resulting characteristic equation is given by

$$\left(s+\frac{1}{RC_2}\right)\left(s^2-\frac{g^2R}{C_1}s+\frac{1}{L_1C_1}\right)=0 \tag{2.26}$$

which corresponds to an unstable system.

The BIF regulator acting as a power gyrator can be stabilized by inserting a compensating network in the feedback loop using the technique reported in [38]. However, an important goal in our design is to minimize the complexity of the control loop, i.e., to reduce the loop to a multiplier, a linear algebraic circuit and a comparator that guarantee a sliding regime on the surface $S(x) = i_2 - gV_g$. Thus, instead of feedback compensation, a damping network R_dC_d will be connected in parallel with capacitor C_1 as shown in Fig. 2.7 [18]-[19].

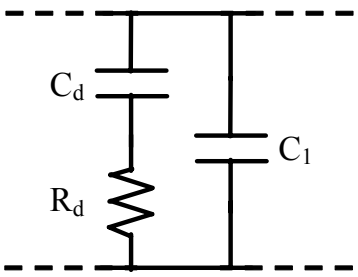

Fig. 2.7 Damping network connected in parallel with capacitor C1

It has to be pointed out that the damping network action is theoretically constrained to transient-state, keeping the converter steady-state equivalent circuit unchanged. The expression of the characteristic equation is given by

$$\left(s+\frac{1}{RC_2}\right)P(s)=0$$

where

$$P(s)=s^3+\left(\frac{1}{R_dC_d}+\frac{1}{R_dC_1}-\frac{g^2R}{C_1}\right)s^2+\left(\frac{1}{L_1C_1}-\frac{g^2R}{R_dC_dC_1}\right)s+\frac{1}{L_1C_1R_dC_d} \tag{2.27}$$

In Appendix A, the Routh's criterium is applied to the characteristic polynomial (2.27) leading to the following stability conditions

$$R_d C_d < \frac{C_1 + C_d}{g^2 R} \tag{2.28}$$

$$R_d C_d > g^2 R L_1 \tag{2.29}$$

$$g^2 R R_d{}^2 C_d{}^2 + g^2 R L_1 (C_1 + C_d) < (g^4 R^2 L_1 + C_d) R_d C_d \tag{2.30}$$

Taking into account conditions (2.28)-(2.30), the block diagram depicted in Fig. 2.5 has been implemented as shown in Fig. 2.8 where the complete converter and its control circuit are depicted in detail. Note that the sliding surface is implemented by means of an analog multiplier and an operational amplifier-based linear circuit, while the ideal comparator function is performed by a hysteretic comparator.

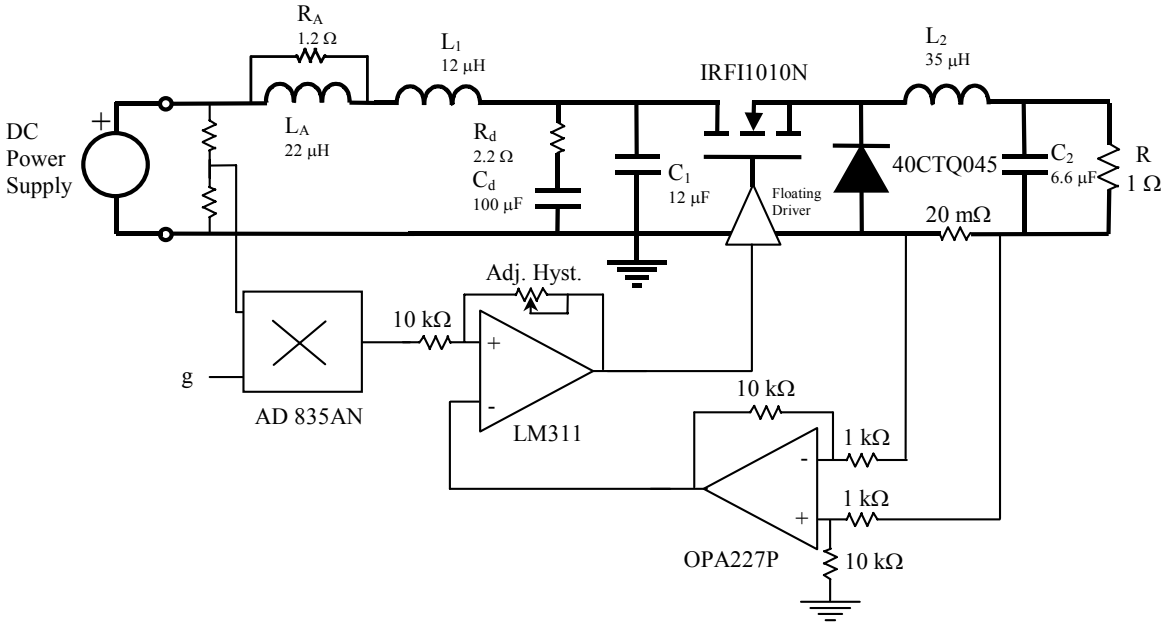

Fig. 2.8 Practical implementation of a BIF-converter-based G-gyrator L_1 =12 µH, L_2=35 µH C_1=12 µF , C_2=6.6 µF C_d=100 µF R_d=2.2 Ω, L_a=22 µH R_a=1.2 Ω, g=0.5 Ω^{-1} R=1 Ω

The parameters of the G-gyrator are given by the set of values V_g = 20 V, R = 1 Ω, g = 0.5 Ω^{-1}, L_1 = 12 µH, C_1 = 12 µF, C_d = 100 µF, R_d = 2.2 Ω, L_2 = 35 µH, and C_2 = 6.6 µF. A damping network of type shown in Fig. 2.9, with L_a=22 µH and R_a=1.2 Ω, was also inserted to improve the dynamics behaviour of the gyrator state variables

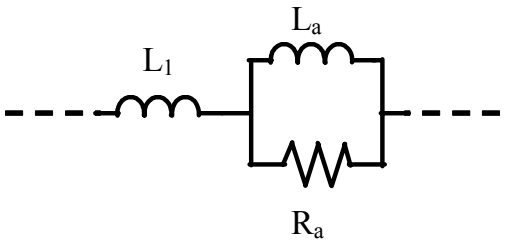

Fig. 2.9 Damping network connected in series with inductor L_1

Figures 2.10-2.15 show the P-SPICE simulated responses and the corresponding experimental results of the BIF gyrator in different cases. Thus, Figs. 2.10 and 2.11 show respectively the simulated and experimental start-up of the power gyrator

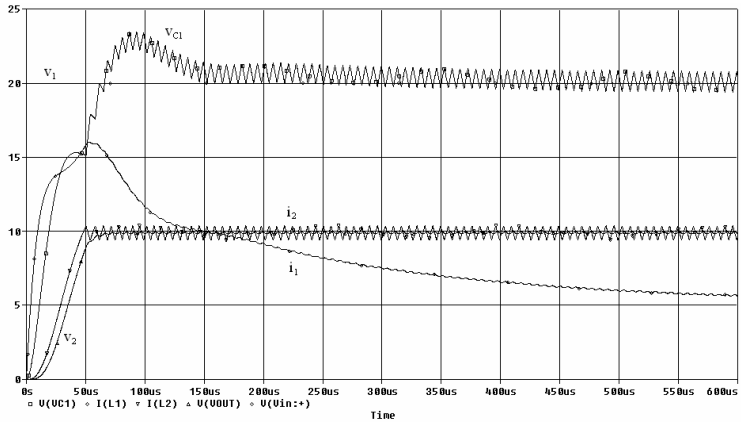

Fig. 2.10 Simulated behaviour of the BIF converter-based G-gyrator with variable switching frequency during start-up

The measured power delivered to the load in steady-state is 101 W. Which corresponds to a 90 % efficiency. It can be verified in Figs, 2.10 and 2.11 that both circuits exhibit the G-gyrator characteristics defined in equations (2.1)-(2.2). Observe that output current I_2 is 10 A for an input voltage of 20 V whereas input current I_1 is 5 A for an output voltage of 10 V approximately.

The effect of a pulsating voltage superposed to the nominal input voltage is illustrated in Fig 2.12 by simulation an in Fig. 2.13 by means of experimental results. The gyrator state variables reach a stable state after a transient-state produced by the insertion of step perturbations of ± 4 V in series with the input port. Note that in the two steady-states of Figs. 2.12-2.13, the output current is proportional to the input voltage, with a proportionality factor $g=0.5\ \Omega^{-1}$.

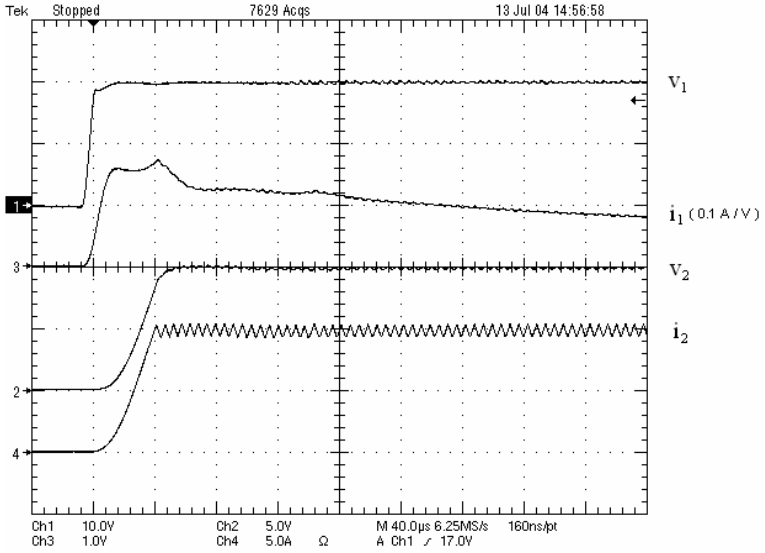

Fig. 2.11 *Experimental behavior of the BIF converter-based G-gyrator with variable switching frequency during start-up*

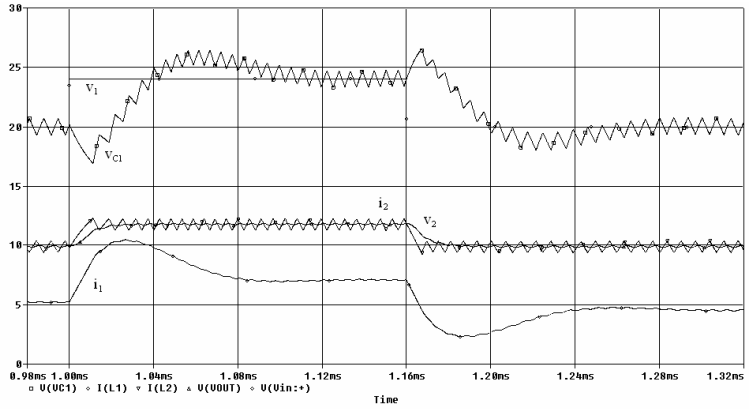

Fig. 2.12 *Simulated behavior of the BIF converter-based G-gyrator in sliding-mode for a pulsating input voltage.*

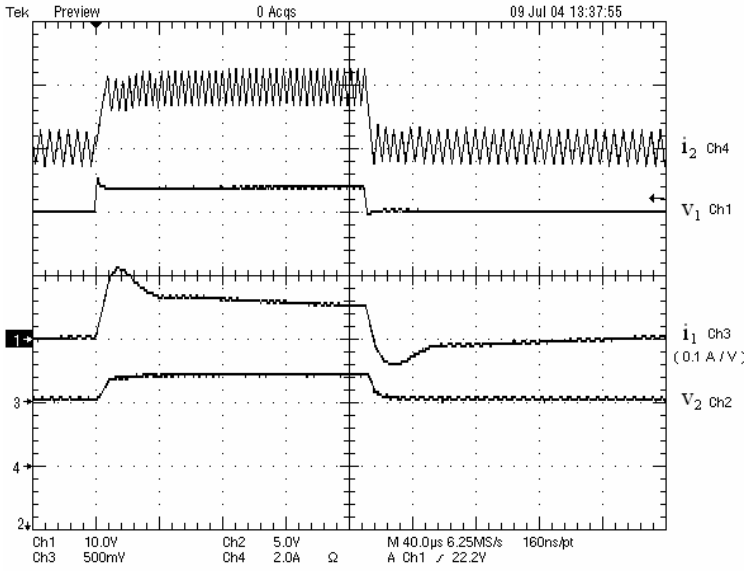

Fig. 2.13 *Experimental behavior of the BIF converter-based G-gyrator in sliding-mode for a pulsating input voltage.*

The current source nature of the output current i_2 is illustrated in Figs. 2.14-2.15 after introducing ± 50 % perturbations in the load resistance. The output voltage reproduces proportionality the pulsating behavior or the load, the proportionality constant being the output current $i_2 = 10\ A$.

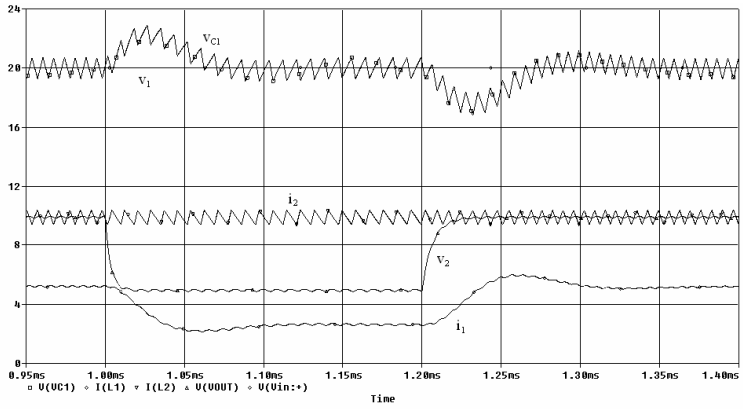

Fig. 2.14 *Simulated behaviour of the BIF converter-based G-gyrator in sliding-mode for a pulsating load*

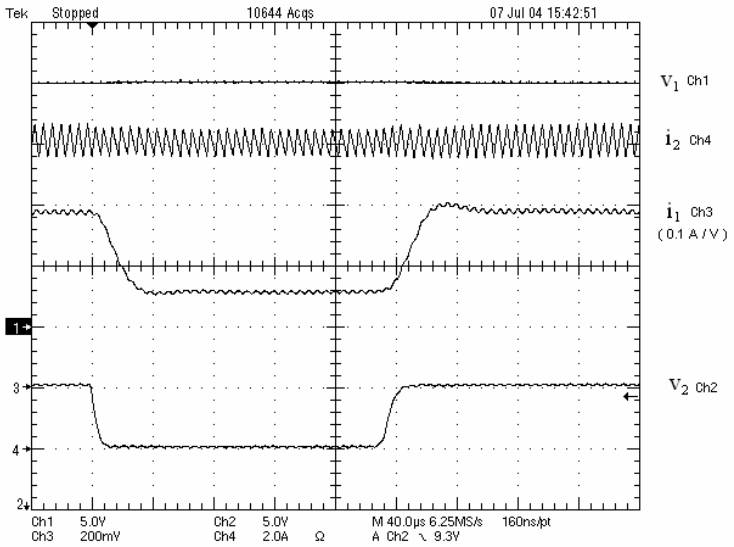

Fig. 2.15 *Experimental behavior of the BIF converter-based G-gyrator in sliding-mode for a pulsating load*

We can conclude that in all cases under study (Figs. 2.10-2.15) the experimental results are in good agreement with the simulated predictions.

2.2.1.1.2 Analysis of the BOF converter as a power G-gyrator with variable switching frequency

A similar analysis of a boost with output filter (BOF) reveals that the equilibrium point is unstable. The corresponding characteristic equation is given by

$$\left(s-\frac{1}{g^2L_1R}\right)\left(s+\frac{1}{RC_2}\right)=0 \tag{2.31}$$

The insertion of the damping network shown in Fig. 2.7 cannot stabilize the system since the new characteristic equation still corresponds to an unstable system. This equation is expressed as

$$\left(s+\frac{1}{RC_2}\right)\left(s-\frac{1}{L_1g^2R}\right)\left(s+\frac{1}{R_dC_d}\right)=0 \tag{2.32}$$

It can be observed that the damping network R_dC_d only introduces a decoupled dynamic mode characterized by the time constant R_dC_d. As a consequence, there still remains an unstable mode created by the input current i_1. In order to stabilize i_1, a damping network is inserted in series with L_1 as shown in Fig. 2.7. The resulting characteristic equation is given by

$$\left(s+\frac{1}{RC_2}\right)\left(s+\frac{1}{R_dC_d}\right)\left(s^2+s\left(\frac{R_a}{L_a}+\frac{R_a}{L_1}-\frac{1}{g^2RL_1}\right)-\left(\frac{R_a}{L_ag^2RL_1}\right)\right)=0 \tag{2.33}$$

which still corresponds to an unstable system.

2.2.1.1.3 Analysis of the Cuk converter as a power G-gyrator with variable switching frequency

The sliding-mode analysis in the Cuk converter shows that the system is also unstable, the characteristic equation being

$$\left(s^2 - \frac{g^2 R}{1+gR}\frac{1}{C_1}s + \frac{1}{L_1 C_1 (1+gR)}\right)\left(s + \frac{1}{RC_2}\right) = 0 \tag{2.34}$$

The insertion of the damping network shown in Fig. 2.7 can stabilize the system, as demonstrated in Appendix B, if the following conditions are satisfied

$$R_d C_d < \frac{(C_1 + C_d)(1+gR)}{g^2 R} \tag{2.35}$$

$$R_d C_d > g^2 R L_1 \tag{2.36}$$

$$g^2 R R_d{}^2 C_d{}^2 + g^2 R L_1 (C_1 + C_d)(1+gR) < (g^4 R^2 L_1 + C_d (1+gR)) R_d C_d \tag{2.37}$$

Using conditions (2.35)-(2.37), a Cuk converter-based power G-gyrator has been implemented as illustrated in Fig. 2.16 for the set of parameters V_g *=20 V*, *R= 1Ω* , *g=0.5* Ω^{-1} L_1 *= 34 μH*, C_1 *= 15 μF*, C_d *= 47 μF*, R_d *= 1.6 Ω*, L_2 *= 25 μH* and C_2 = 6.6 μF. The damping network shown in Fig. 2.9 with L_a *= 70 μH* and R_a *= 0.5 Ω* has been also inserted in order to improve the dynamic response.

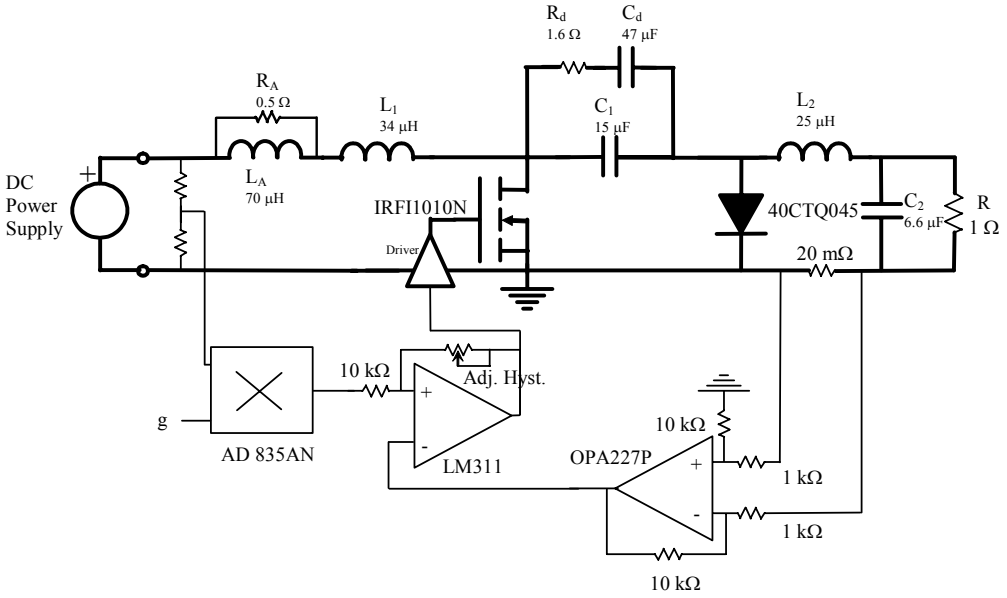

Fig. 2.16 Practical implementation of the Cuk converter-based G-gyrator. V_g *=20 V, R= 1Ω , g=0.5* Ω^{-1} L_1 *= 34 μH,* C_1 *= 15 μF,* C_d *= 47 μF,* R_d *= 1.6 Ω,* L_2 *= 25 μH,* C_2 *= 6.6 μF,* L_a *= 70 μH and* R_a *= 0.5 Ω*

Figs. 2.17 and 2.18 illustrate respectively the PSPICE simulated behavior and the corresponding experimental results of the gyrator when a pulsating load is superposed to the nominal input voltage. The gyrator delivers 65 W at the output port with a 80 % efficiency. It can be observed that input perturbation is directly followed by the output current i_2 and indirectly, through the converter action, by v_2 and i_1.

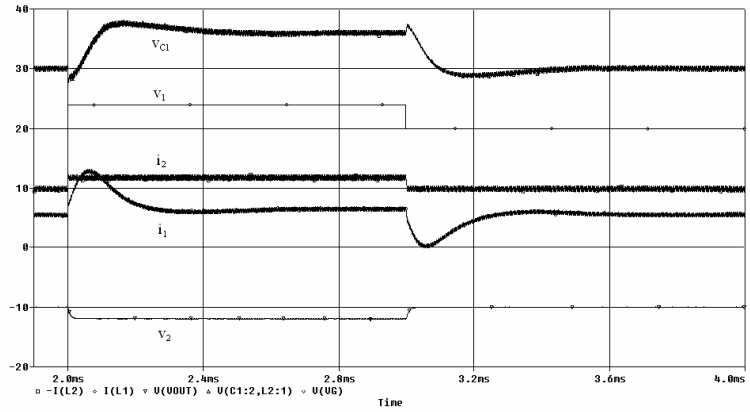

Fig. 2.17 *Simulated behavior of the Cuk converter-based G-gyrator in sliding-mode for a pulsating input voltage*

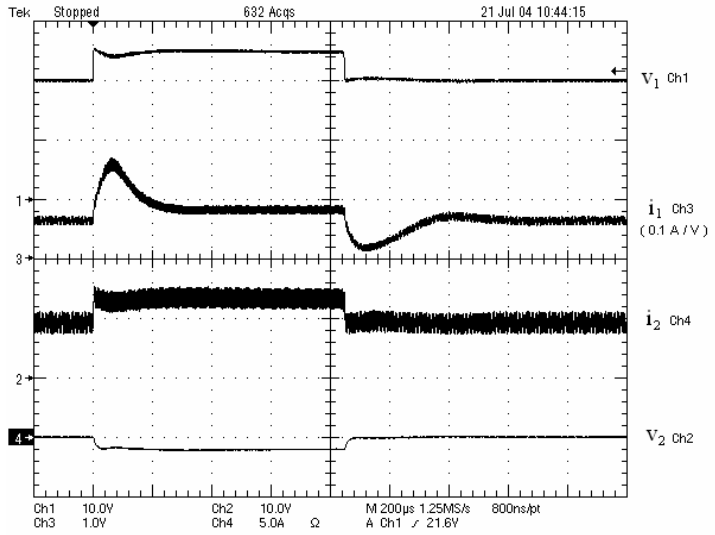

Fig. 2.18 *Experimental behavior of the Cuk converter-based G-gyrator in sliding-mode for a pulsating input voltage.*

2.2.1.2 Power gyrator of type G with constant switching frequency

The realization of a power gyrator operating at constant switching frequency will require the use of a pulse width modulation-based control (PWM). The direct search of a PWM control which guarantees a specific steady-state behavior is not simple. However, it was shown in [20]

that the PWM nonlinear control that imposes $S(x) = 0$ in the steady-state in a switching regulator was the equivalent control $u_{eq}(x)$ found in the analysis of the switching regulator in sliding-mode with a slight modification which describes the regulator start-up until the surface $S(x)$ is reached by the system trajectory. This correspondence between sliding-mode equivalent control and PWM zero-dynamics control is used in this section to derive PWM-based power G-gyrators.

Fig. 2.19 shows a block diagram of a fourth-order PWM switching regulator with potential G-gyrator characteristics. It consists of a switching converter which is controlled by means of a PWM regulation loop whose duty cycle $\Gamma(x(t))$ is a nonlinear function of the converter state variables. In the equilibrium point X^* (steady-state), the duty cycle $\Gamma(x^*)$ imposes $I_2 = g\, V_1$ which automatically implies $I_1 = g\, V_2$. Also, it has to be pointed out that

$$\Gamma(x(t))\big|_{t=nT} = \frac{T_{ON}(nT)}{T} \tag{2.38}$$

where T is the switching period, n is the n^{th} period and $T_{ON}(nT)$ is the duration of the on-state in the n^{th} period.

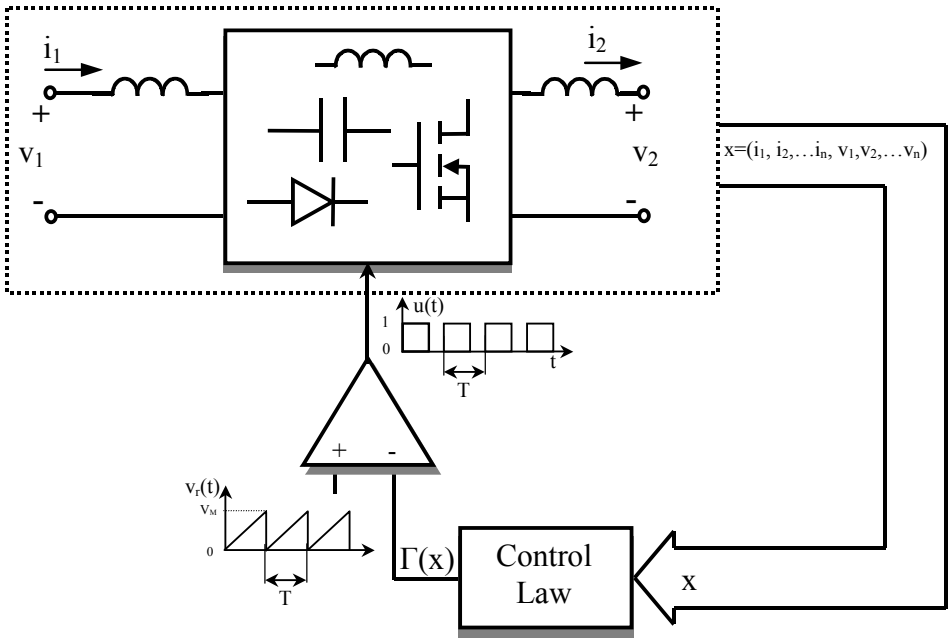

Fig. 2.19 Block diagram of a PWM-based G-gyrator

Figure 2.20 illustrates equation (2.38). It can be observed that the continuous-time function $\Gamma(x)$ will be a good approximation of the discrete-time function $\frac{T_{ON}(nT)}{T}$ if the switching period is considerably smaller than the converter time-constants.

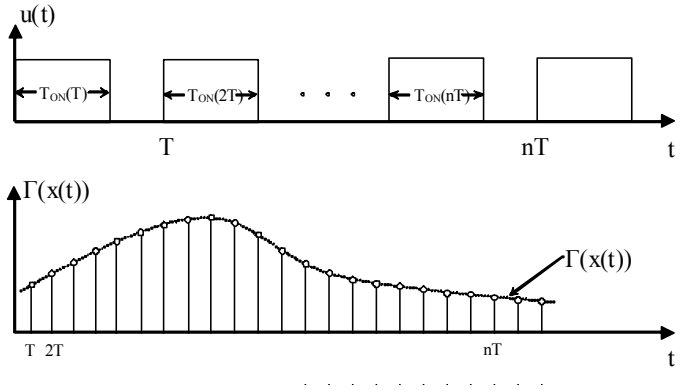

Fig. 2.20 *Equivalence between Γ(x(t)) and* $\frac{T_{ON}(nT)}{T}$ *at sampling instants.*

2.2.1.2.1 Analysis of the BIF converter as PWM-based G-gyrator

It has been shown in 2.2.1.1.1 that the insertion of the damping network of Fig. 2.7 in the BIF converter operating as G-gyrator with variable switching frequency can stabilize the system. The state equations of power stage are given by

$$\begin{aligned}
\frac{di_1}{dt} &= \frac{-v_{C1}}{L_1} + \frac{v_g}{L_1} \\
\frac{di_2}{dt} &= u\frac{v_{C1}}{L_2} - \frac{v_2}{L_2} \\
\frac{dv_{C1}}{dt} &= \frac{i_1}{C_1} + \frac{v_{CD} - v_{C1}}{R_D C_1} - \frac{i_2}{C_1}u \\
\frac{dv_{CD}}{dt} &= \frac{v_{C1}}{R_D C_D} - \frac{v_{CD}}{R_D C_D} \\
\frac{dv_2}{dt} &= \frac{i_2}{C_2} - \frac{v_2}{RC_2}
\end{aligned} \tag{2.39}$$

where *u=1* during T_{ON} and *u=0* during T_{OFF}.

Under the above mentioned conditions of a switching frequency considerably bigger than the converter natural frequencies, the discrete variable u in (2.39) can be substituted by a continuous variable *Γ(x(t))* which takes the average value of *u* in each period at the corresponding sampling instants *T, 2T, ... nT* as expressed in (2.38) and as shown in Fig. 2.20. Note that *Γ(x(t))* can take all the values between 0 and 1 and therefore is bounded by the maximum and minimum values of *u*

$$0 < \Gamma(x(t)) < 1 \tag{2.40}$$

Now, we can write the equation describing the dynamics of i_2 as follows

$$\frac{di_2}{dt} = \Gamma \frac{v_{C1}}{L_2} - \frac{v_2}{L_2} \tag{2.41}$$

If equation (2.41) could be expressed as

$$\frac{di_2}{dt} = \frac{R_K}{L_2}\left(gV_g - i_2\right) \tag{2.42}$$

equation (2.42) would result in steady-state in

$$I_2 = gV_g \tag{2.43}$$

which is the desired behavior of a G-gyrator.

Equation (2.41) will become equation (2.42) if $\Gamma(x(t))$ is expressed as

$$\Gamma(x) = \frac{v_2 + R_K\left(gV_g - i_2\right)}{v_{C1}} \tag{2.44}$$

which in the steady-state becomes

$$\Gamma(x^*) = \frac{v_2}{v_{C1}} \tag{2.45}$$

which is the equivalent control corresponding to the sliding-mode approach when the constraint $S(x) = i_2 - gVg$ is added to (2.39).

Therefore, the dynamics of the system can be separated in two types of dynamics, i.e., the dynamics of the start-up given by the time-constant $\frac{L_2}{R_K}$ and the dynamics of the system restricted to the surface $S(x) = i_2 - gVg$ where the system motion takes place on the average. The last dynamics is exactly equal to the ideal sliding dynamics analyzed in 2.2.1.1.1. Hence, the characteristic polynomial $D_{PWM}(s)$ will be expressed as

$$D_{PWM}(s) = D_{SLIDING}(s)\left(s + \frac{R_K}{L_2}\right) \tag{2.46}$$

where $D_{SLIDING}(s)$ is the characteristic polynomial found in 2.2.1.1.1 describing the ideal sliding dynamics. Hence, the system characteristic equation $D_{PWM}(s) = 0$ will be given by

$$\left(s + \frac{R_K}{L_2}\right)\left(s + \frac{1}{RC_2}\right)P(s) = 0$$

$$P(s) = s^3 + \left(\frac{1}{R_d C_d} + \frac{1}{R_d C_1} - \frac{g^2 R}{C_1}\right)s^2 + \left(\frac{1}{L_1 C_1} - \frac{g^2 R}{R_d C_d C_1}\right)s + \frac{1}{L_1 C_1 R_d C_d} \tag{2.47}$$

Therefore, the system will be stable if conditions (2.28)-(2.30) found previously in the analysis of the G-gyrator with variable switching frequency are also satisfied.

Figure 2.21 illustrates the practical implementation of the block diagram depicted in Fig. 2.19. The converter parameters satisfy conditions (2.28)-(2.30) and are given by $V_g = 20\ V$, $R = 1\ \Omega$, $g = 0.5\ \Omega^{-1}$, $L_1 = 12\ \mu H$, $C_1 = 12\ \mu F$, $C_d = 100\ \mu F$, $R_d = 2.2\ \Omega$, $R_K = 48\ \Omega$, $L_2 = 35\ \mu H$, $C_2 = 6.6\ \mu F$. The switching frequency f_s is *200 kHz*. Note that a damping network of the type shown in Fig, 2.9 with $L_a = 22\ \mu H$ and $R_a = 1.2\ \Omega$ was also inserted to improve the dynamic behavior of the gyrator state variables.

Figures 2.22-2.27 show the P-SPICE simulated responses and the corresponding experimental results of the PWM-BIF G-gyrator in different cases. Figures 2.22 and 2.23, in particular, illustrate respectively the simulated and experimental start-up of the G-gyrator. The measured power delivered to the load in steady-state is 102 W, this implying a 88 % efficiency. It can be verified in both figures that the circuit exhibits the gyrator characteristics defined in equations (2.1)-(2.2).

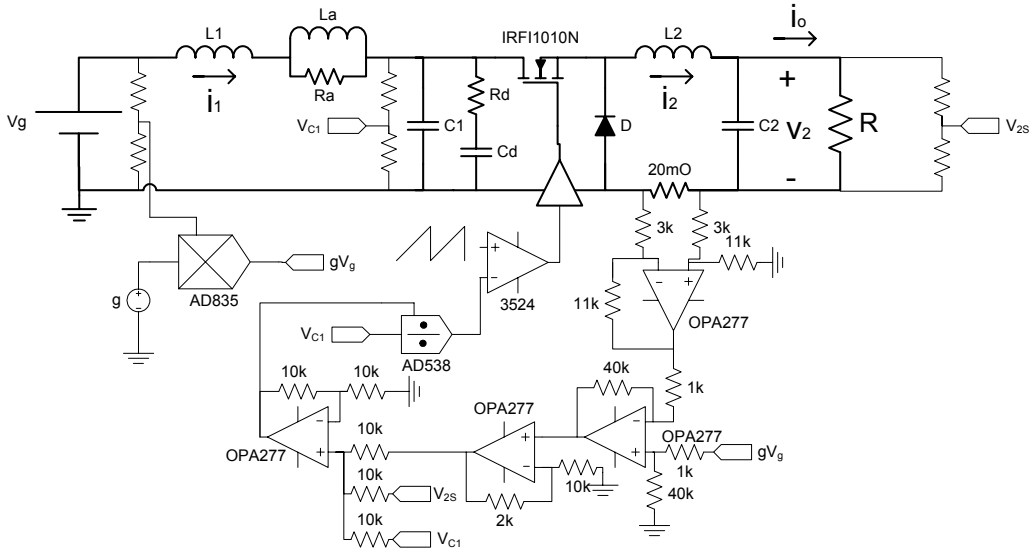

Fig. 2.21 Practical implementation of a BIF converter-based PWM G-gyrator. $V_g = 20\ V$, $R = 1\ \Omega$, $g = 0.5\ \Omega^{-1}$, $L_1 = 12\ \mu H$, $C_1 = 12\ \mu F$, $C_d = 100\ \mu F$, $R_d = 2.2\ \Omega$, $R_K = 48\ \Omega$, $L_2 = 35\ \mu H$, $C_2 = 6.6\ \mu F$, $f_s = 200\ kHz$, $L_a = 22\ \mu H$ and $R_a = 1.2\ \Omega$

The effect of a pulsating voltage superposed on the nominal input voltage is illustrated in Fig. 2.24 by simulation and in Fig. 2.25 by means of experimental results. It can be observed that the gyrator state variables reach a stable state after a transient-state produced by the insertion of step perturbations of ± 4 V in series with the input port. Note that in the two steady-states of Figs. 2.24 and 2.25 the output current is proportional to the input voltage with a proportionality factor $g = 0.5\ \Omega^{-1}$.

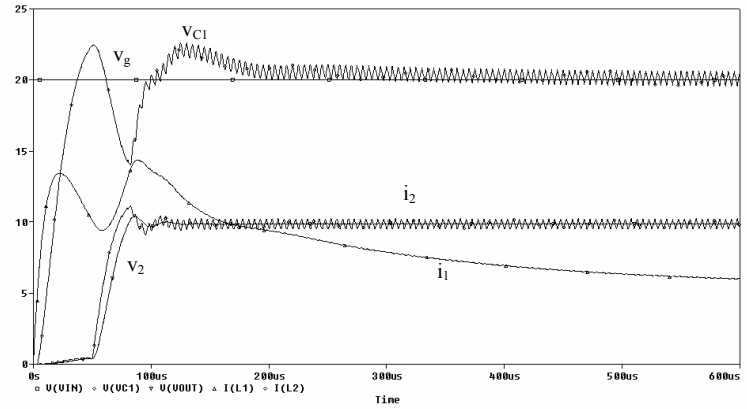

Fig. 2.22 Simulated behavior of the PWM BIF converter-based G-gyrator during start-up

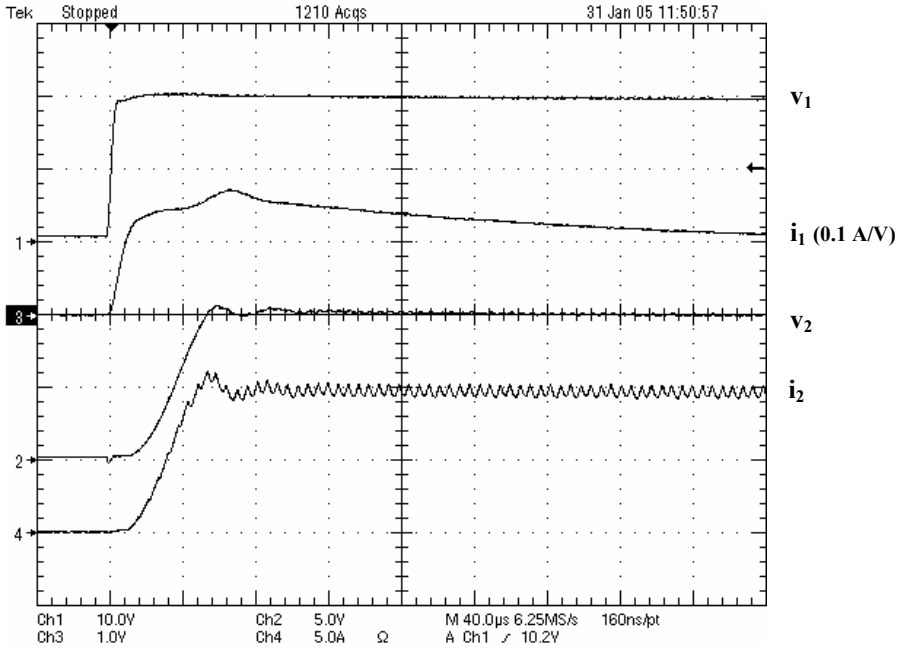

Fig. 2.23 Experimental behavior of the PWM BIF converter-based G-gyrator during start-up

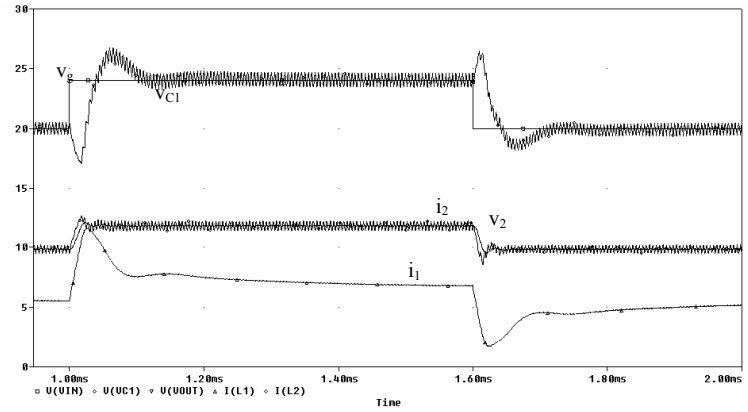

Fig. 2.24 Simulated behavior of the PWM BIF converter-based G-gyrator for a pulsating input voltage

The current source nature of the output current i_2 is illustrated in Figures 2.26 (simulation) and 2.27 (experiments) after introducing ± 50 % perturbation in the load resistance. The output voltage is proportional to the pulsating load, the proportionality constant being the output current $i_2 = 10\ A$.

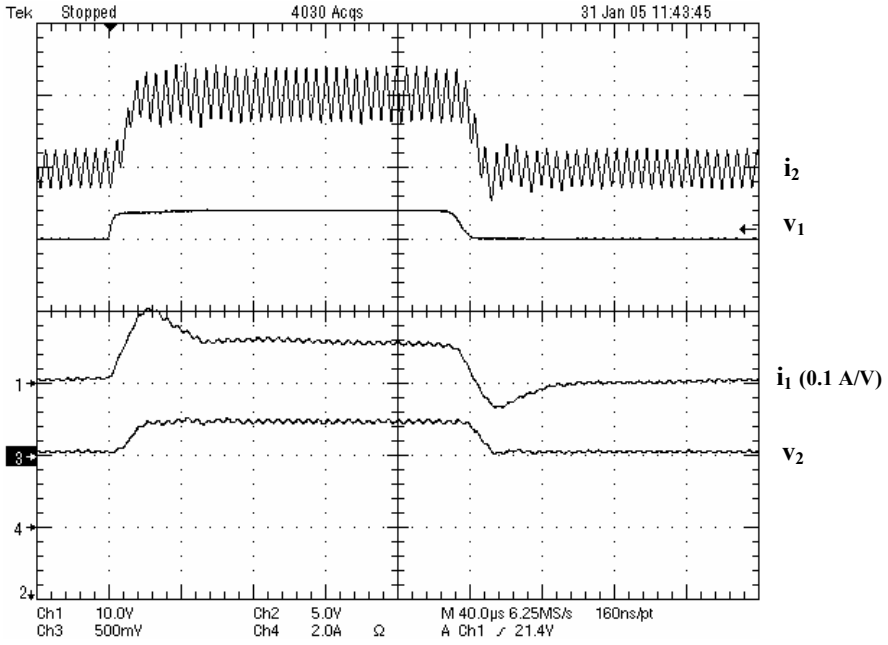

Fig. 2.25 Experimental behavior of the PWM BIF converter-based G-gyrator for a pulsating input voltage

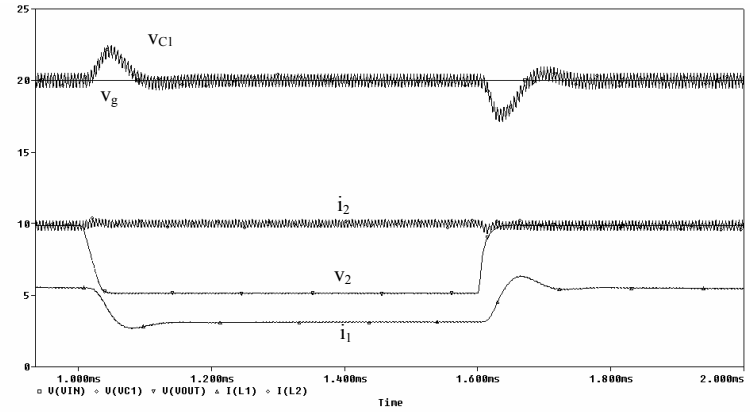

Fig. 2.26 Simulated behavior of the PWM BIF converter-based G-gyrator for a pulsating load

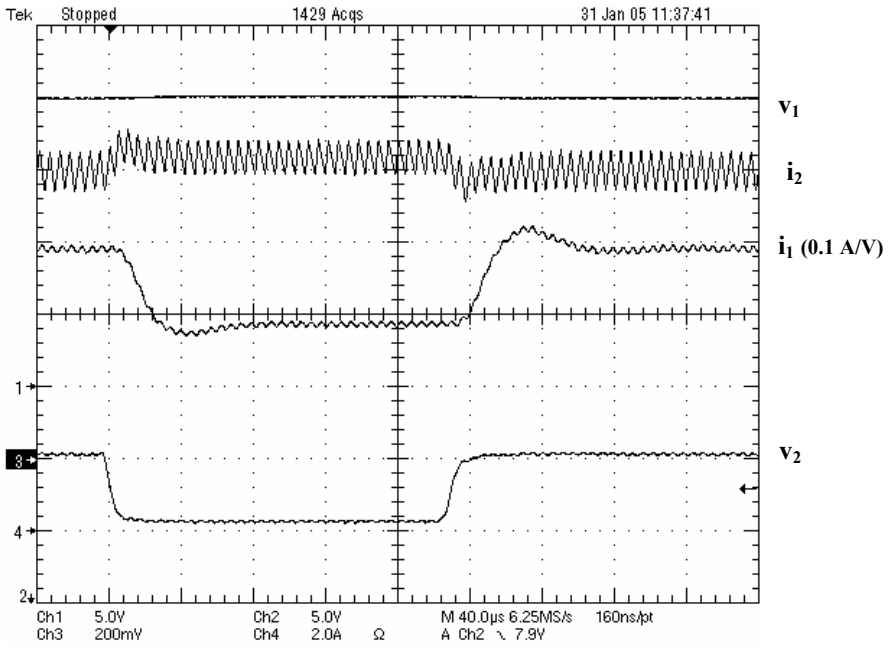

Fig. 2.27 Experimental behavior of the PWM BIF converter-based G-gyrator for a pulsating load

In all the cases depicted in Fig. 2.22-2.27 there is a good agreement between simulated and experimental results. We have to point out that the switching frequency is constant in the whole operation regime, i.e., in both transient and steady-states.

2.2.1.3 Other types of G-gyrators

Equations (2.1)-(2.2) define a power gyrator of type G which is intended to transform a voltage source at the input port into a current source at the output port.

However, we would synthesize a G-gyrator intending to transform a voltage source at the output port into a current source at the input port. In such situation, the power gyrator could be implemented as illustrated in Fig. 2.27 where a 4th order converter is also assumed in the power stage.

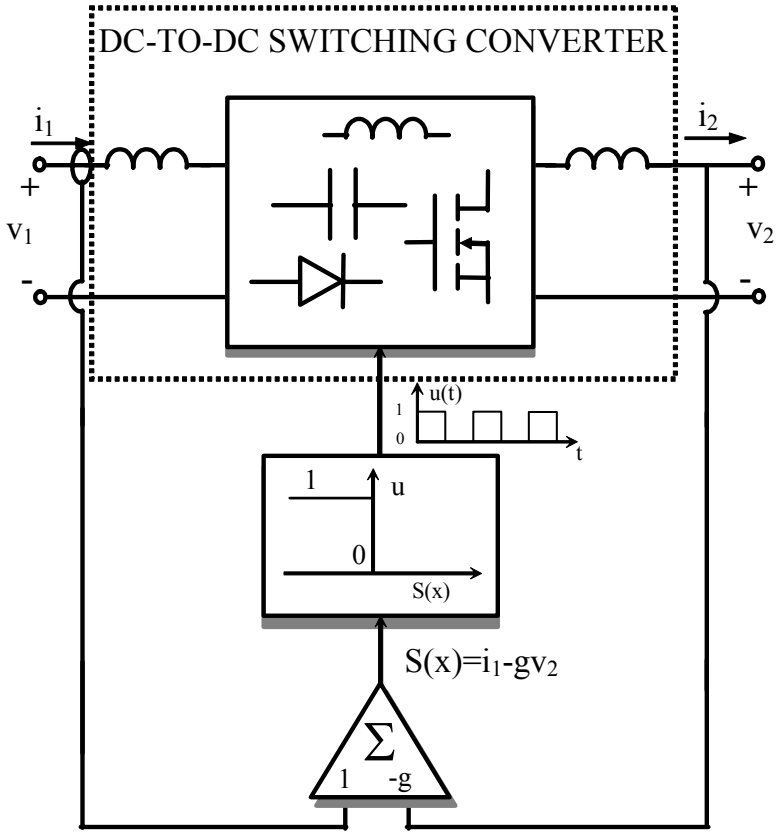

Fig. 2.28 *Block diagram of a dc-to-dc switching regulator operating in sliding-mode with G-gyrator characteristics and with i_1 as controlled variable.*

Since the regulator establishes the gyrator characteristics through the control of current i_1, we will call this class of circuits G-gyrators with controlled input current.

The fourth order converters previously studied, i.e., BIF, BOF and Cuk converter will be analyzed next in sliding-mode operation assuming $S(x) = i_1 - gv_2$, where v_2 is a constant voltage.

2.2.1.3.1 *Analysis of the BIF converter as G-gyrator with controlled input current and variable switching frequency*

The set of equations describing the BIF converter are the following

$$\begin{aligned}\frac{di_1}{dt} &= \frac{-v_{C1}}{L_1} + \frac{V_g}{L_1} \\ \frac{di_2}{dt} &= \frac{v_{C1}}{L_2}u - \frac{V_2}{L_2} \\ \frac{dv_{C1}}{dt} &= \frac{i_1}{C_1} - \frac{i_2}{C_1}u\end{aligned} \tag{2.48}$$

where V_2 is a constant voltage.

Considering $S(x) = i_1 - gv_2$ as sliding surface and imposing the invariance conditions $S(x) = 0$ and $\frac{dS}{dt} = 0$ reveals that there is no equivalent control and hence no sliding motions can be induced in the switching converter. However, it has been found by simulation that the system has a stable limit cycle if the comparator shown in Fig. 2.28 is a hysteretic comparator. Fig. 2.29 shows the PSIM simulations of a BIF converter-based G-gyrator with controlled input current during start-up for the set of parameters $V_g = 20\ V$, $V_2 = 12$ V, $g = 0.5\ \Omega^{-1}$, $L_1 = 12\ \mu H$, $C_1 = 12\ \mu F$, $C_d = 100\ \mu F$, $R_d = 2.2\ \Omega$, $L_2 = 35\ \mu H$, $L_a = 22\ \mu H$ and $R_a = 1.2\ \Omega$.

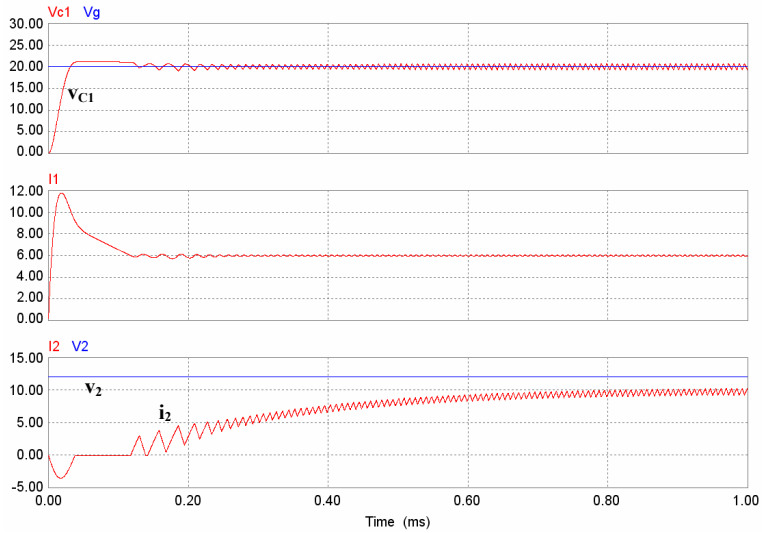

Fig. 2.29 *Simulated behavior of a BIF converter-based G-gyrator with controlled input current during start-up*

Also figure 2.30 illustrates the PSIM simulations of the gyrator behavior for a pulsating input voltage.

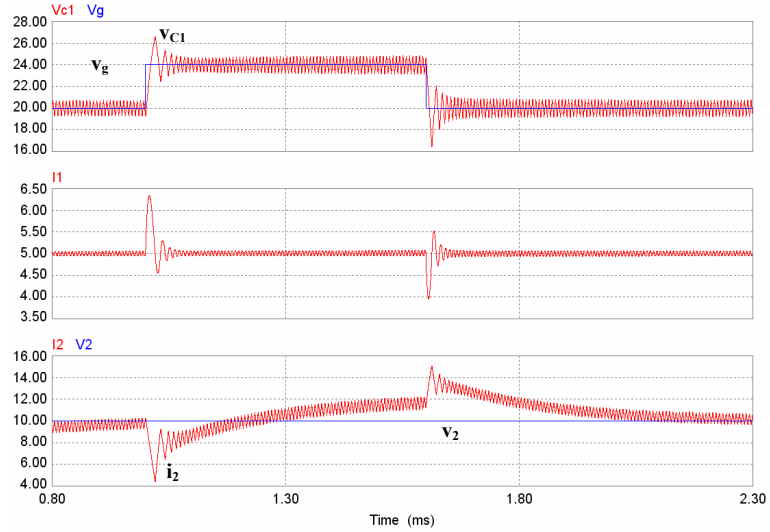

Fig. 2.30 *Simulated behavior of a BIF converter-based G-gyrator with controlled input current for a pulsating input voltage*

It has to be pointed out that in both figures the circuit exhibits stable G-gyrator characteristics.

2.2.1.3.2 Analysis of the Cuk converter as G-gyrator with controlled input current and variable switching frequency

The equations describing the Cuk converter are in this case

$$\begin{aligned}\frac{di_1}{dt} &= \frac{-v_{C1}}{L_1} + \frac{v_{C1}}{L_1}u + \frac{V_g}{L_1} \\ \frac{di_2}{dt} &= \frac{v_{C1}}{L_2}u - \frac{V_2}{L_2} \\ \frac{dv_{C1}}{dt} &= \frac{i_1}{C_1} - \frac{i_1}{C_1}u - \frac{i_2}{C_1}u\end{aligned} \tag{2.49}$$

where V_2 is a constant voltage.

Assuming $S(x) = gv_2 - i_1$ as a describing surface and imposing the invariance conditions $S(x)=0$ and $\frac{dS}{dt} = 0$ in (2.49) leads to the equivalent control

$$u_{eq}(x) = \frac{v_{C1} - V_g}{v_{C1}} \tag{2.50}$$

Introducing (2.50) in (2.49) and assuming $S(x)=0$ result in the following ideal sliding dynamics

$$\frac{di_2}{dt} = \frac{v_{C1} - V_g}{L_2} - \frac{V_2}{L_2} = g_1(x) \tag{2.51}$$

$$\frac{dv_{C1}}{dt} = \frac{gV_2}{C_1} - \frac{gV_2}{C_1}\frac{v_{C1} - V_g}{v_{C1}} - \frac{i_2}{C_1}\frac{v_{C1} - V_g}{v_{C1}} = g_2(x) \tag{2.52}$$

The coordinates of the equilibrium point of the ideal sliding dynamics are

$$x^* = [I_1, I_2, V_{C1}]^+ = [gV_2, gV_g, V_2 + V_g]^+ \tag{2.53}$$

where it can be observed that $I_1 = gV_2$ and $I_2 = gV_g$ which corresponds to a steady-state gyrator behavior.

The linearization of equation (2.51) around the equilibrium point (2.52) yields the Jacobian matrix

$$J = \begin{bmatrix} \left.\frac{\partial g_1}{\partial i_2}\right|_{x^*} & \left.\frac{\partial g_1}{\partial v_{C1}}\right|_{x^*} \\ \left.\frac{\partial g_2}{\partial i_2}\right|_{x^*} & \left.\frac{\partial g_2}{\partial v_{C1}}\right|_{x^*} \end{bmatrix} = \begin{bmatrix} 0 & \frac{1}{L_2} \\ \frac{-1}{C_1}\left(\frac{V_2}{V_2 + V_g}\right) & \frac{-gV_g}{C_1(V_2 + V_g)} \end{bmatrix} \tag{2.54}$$

Hence, the characteristic equation is given by

$$s^2 + s\frac{gV_g}{C_1(V_2 + V_g)} + \frac{1}{L_2}\frac{V_2}{C_1(V_2 + V_g)} = 0 \tag{2.55}$$

which corresponds to a stable system.

Figs. 2.31-2.34 show the PSIM simulations of a Cuk converter-based G-gyrator with controlled input current with the set of parameters V_g=*15 V,* L_1 = *75*μ*H,* C_1 = *10* μ*F,* L_2 = *75* μ*H,* g = *0.5* Ω^{-1} *,*V_2 = *24 V* and *12 V*. The G-gyrator characteristics are clearly illustrated in all the cases simulated in Figs. 2.31-2.34

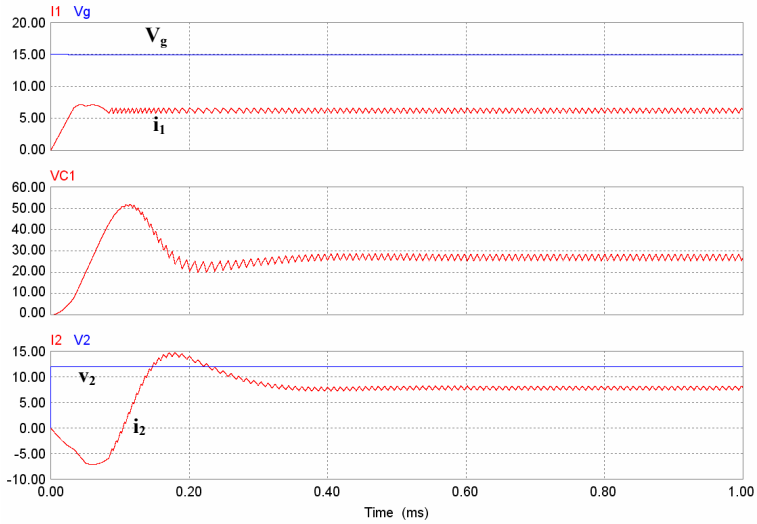

Fig. 2.31 *Simulated behavior of a Cuk converter-based G-gyrator with controlled input current during start-up (V_2=12 V)*

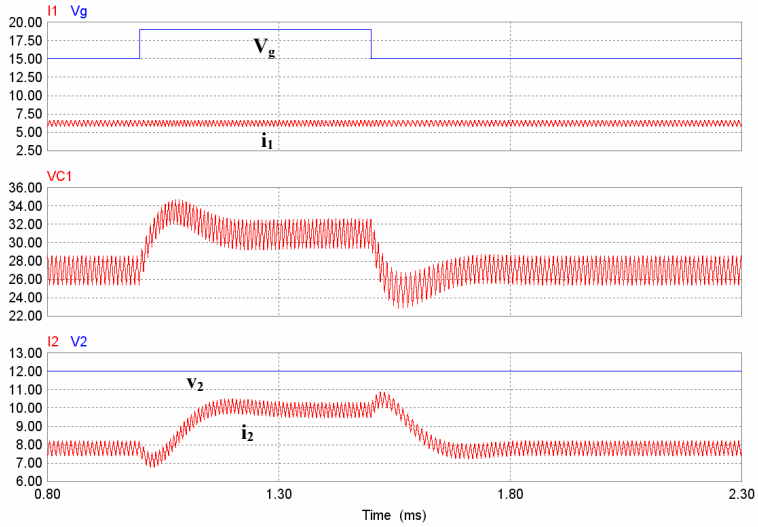

Fig. 2.32 *Simulated response of a Cuk converter-based G-gyrator with controlled input current for a pulsating input voltage (V_2=12 V)*

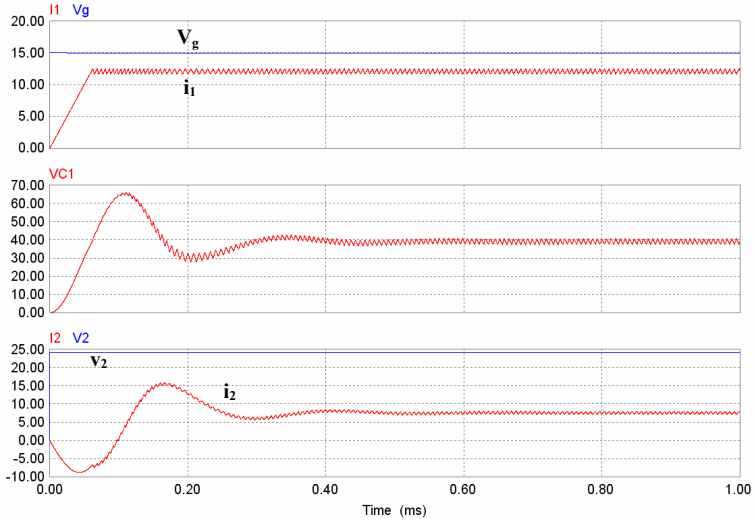

Fig. 2.33 *Simulated behavior of a Cuk converter-based G-gyrator with controlled input current during start-up (V_2=24 V)*

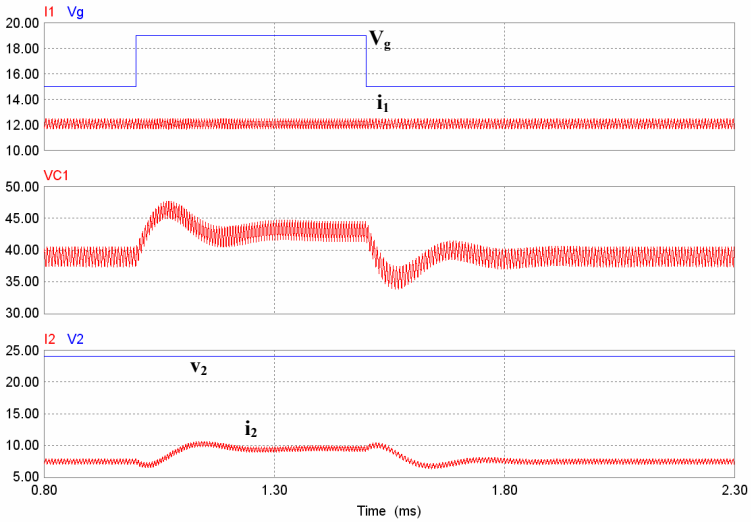

Fig. 2.34 *Simulated behavior of a Cuk converter-based G-gyrator with controlled input current for a pulsating input voltage (V_2=24 V)*

The Cuk converter-based power G-gyrator with controlled input current has been implemented as illustrated in Fig. 2.35 for the set of parameters V_g =15 V, L_1 = 75μH, C_1 = 10 μF, L_2 = 75 μH, g = 0.25 Ω^{-1} (0.5 Ω^{-1}), V_{BAT} = 24 V (12V).

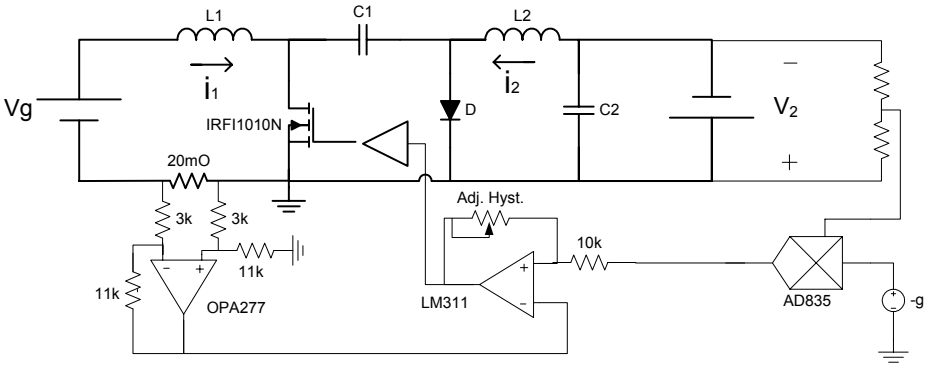

Fig. 2.35 *Practical implementation of the Cuk converter-based G-gyrator with controlled input current. V_g=15 V, L_1 = 75μH, C_1 = 10 μF, L_2 = 75 μH, g = 0.25 Ω^{-1} (0.5 Ω^{-1}) ,V_{BAT} = 24 V (12V).*

Figures 2.36 and 2.37 show the experimental behavior of the gyrator during start-up for V_2 = *12 V* and V_2 = *24 V* respectively. The gyrator response to ± 4 V input voltage perturbations of step type is illustrated in Figs. 2.38 and 2.39 for V_2 = *12 V* and V_2 = *24 V* respectively. The experimental results are in good agreement with the simulations previously shown. The gyrator delivers to the 12 V battery 75 W with a 82 % efficiency and the same power to the 24 V battery with 83 % efficiency.

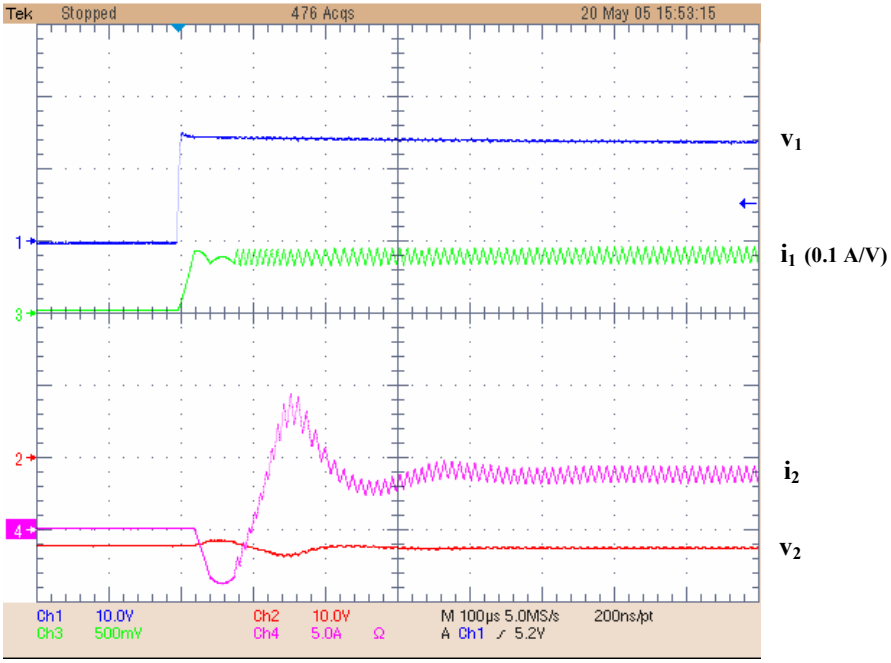

Fig. 2.36 *Experimental behavior of a Cuk converter-based G-gyrator with controlled input current during start-up (V_2=12 V)*

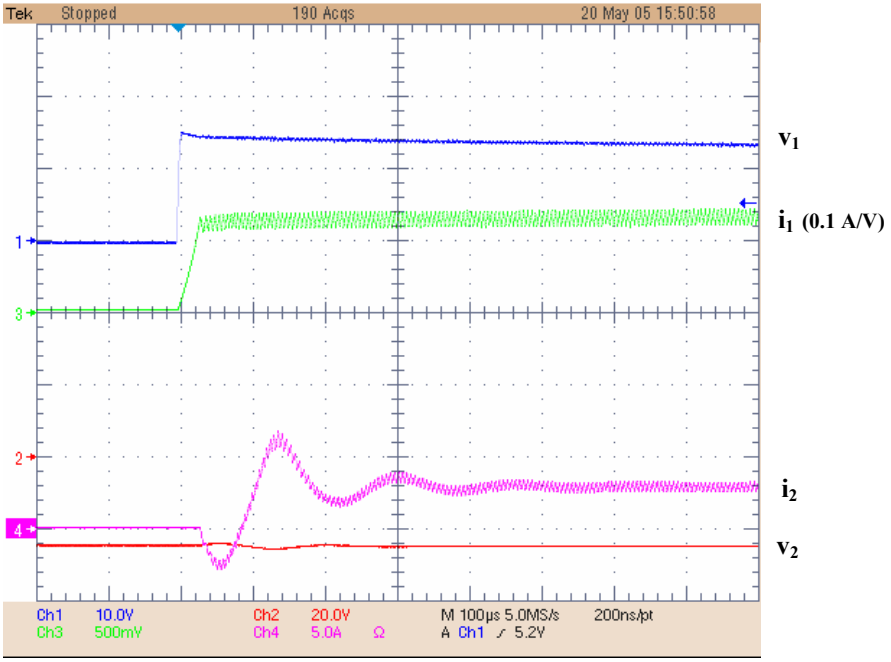

Fig. 2.37 *Experimental behavior of a Cuk converter-based G-gyrator with controlled input current during start-up (V_2=24 V)*

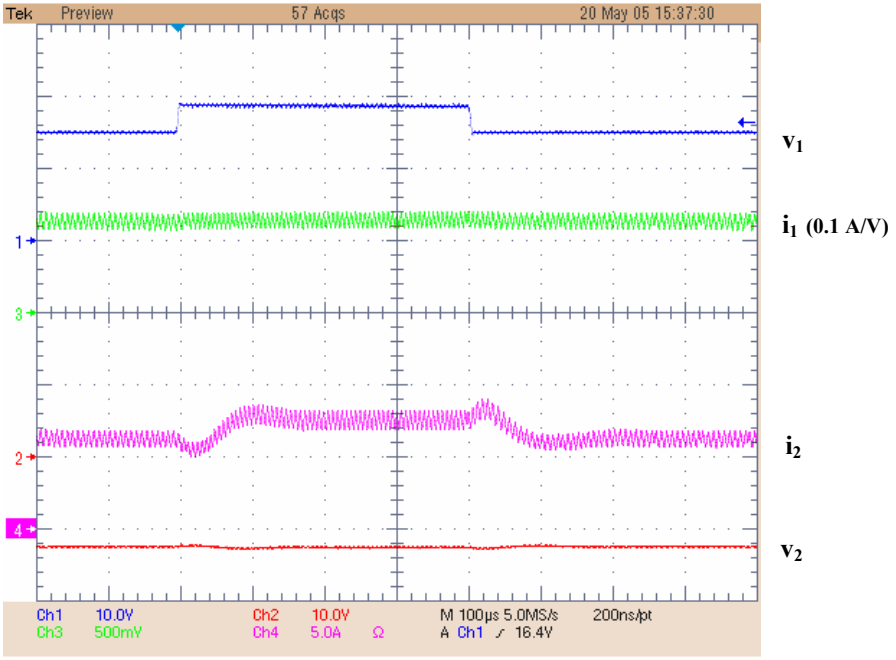

Fig. 2.38 *Experimental response of a Cuk converter-based G-gyrator with controlled input current to a pulsating input voltage (V_2=12 V)*

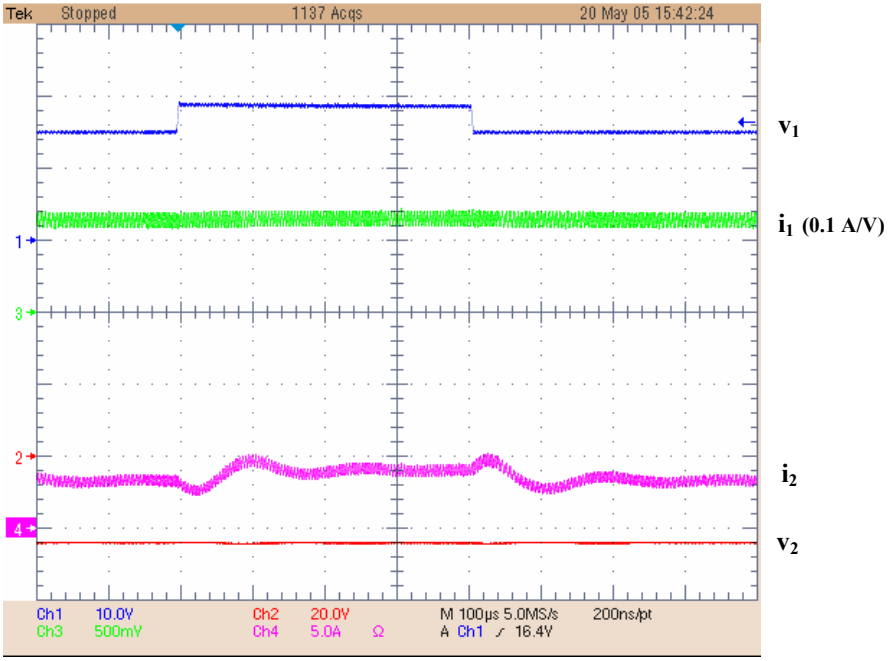

Fig. 2.39 *Experimental response of a Cuk converter-based G-gyrator with controlled input current to a pulsating input voltage (V_2=24 V)*

2.2.1.3.3 Analysis of the BOF converter as G-gyrator with controlled input current and variable switching frequency

The BOF converter can be represented by the following set of differential equations

$$\begin{aligned} \frac{di_1}{dt} &= \frac{v_{C1}}{L_1}(u-1)+\frac{V_g}{L_1} \\ \frac{di_2}{dt} &= \frac{v_{C1}}{L_2}-\frac{V_2}{L_2} \\ \frac{dv_{C1}}{dt} &= \frac{i_1}{C_1}-\frac{i_1}{C_1}u-\frac{i_2}{C_1} \end{aligned} \qquad (2.55)$$

where V_2 is a constant voltage

Assuming $S(x) = gV_2\text{-}i_1$ as a switching surface and imposing the invariance conditions $S(x) = 0$ and $\frac{dS}{dt} = 0$ in (2.55) results in the equivalent control

$$u_{eq}(x) = \frac{v_{C1}-V_g}{v_{C1}} \qquad (2.56)$$

The introduction of (2.56) in (2.55) leads to the following ideal sliding dynamics

$$\frac{di_2}{dt} = \frac{v_{C1}}{L_2} - \frac{V_2}{L_2} = g_1(x)$$

$$\frac{dv_{C1}}{dt} = \frac{gV_2}{C_1} - \frac{gV_2}{C_1}\frac{v_{C1} - V_g}{v_{C1}} - \frac{i_2}{C_1} = g_2(x) \tag{2.57}$$

The coordinates of the equilibrium point are

$$x^* = [I_1, I_2, V_{C1}]^+ = [gV_2, gV_g, V_2 + V_g]^+ \tag{2.58}$$

where it can be observed that $I_1 = gV_2$ and $I_2 = gV_g$, this representing the steady-state gyrator equations.

Linearizing (2.57) around the equilibrium point (2.58) yields the Jacobian matrix

$$J = \begin{bmatrix} \left.\frac{\partial g_1}{\partial i_2}\right|_{x^*} & \left.\frac{\partial g_1}{\partial v_{C1}}\right|_{x^*} \\ \left.\frac{\partial g_2}{\partial i_2}\right|_{x^*} & \left.\frac{\partial g_2}{\partial v_{C1}}\right|_{x^*} \end{bmatrix} = \begin{bmatrix} 0 & \frac{1}{L_2} \\ \frac{-1}{C_1} & \frac{-gV_g}{C_1V_2} \end{bmatrix} \tag{2.59}$$

Finally, the characteristic equation corresponding to (2.59) is given by

$$s^2 + s\frac{gV_g}{C_1V_2} + \frac{1}{L_2C_1} = 0 \tag{2.60}$$

which represents a stable system.

Figs. 2.40 and 2.41 illustrates by means of PSIM simulation the BOF behavior as a G-gyrator with controlled input current for the set of parameters V_g=15 V, g = 0.5 Ω^{-1}, L_1 = 50μH, C_1 = 10 μF, L_2 = 65 μH, V_2 = 24 V. Fig. 2.40 shows the power gyrator start-up while Fig. 2.41 depicts the gyrator response to a pulsating input voltage.

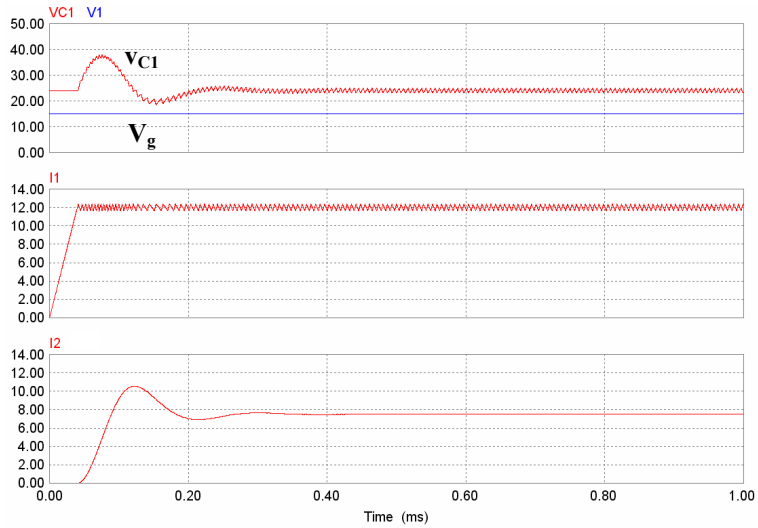

Fig. 2.40 *Simulated behavior of a BOF converter-based G-gyrator with controlled input current during start-up (V_2=24 V)*

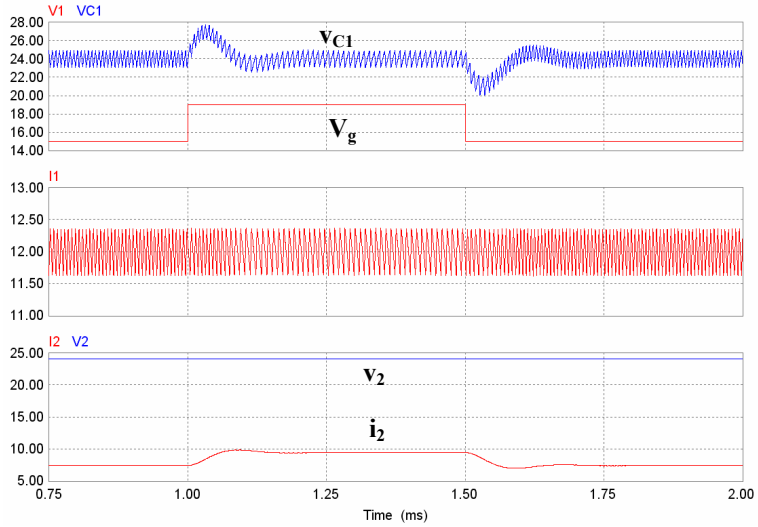

Fig. 2.41 *Simulated behavior of a BOF converter-based G-gyrator with controlled input current for a pulsating input voltage (V_2=24 V)*

2.2.2 Power gyrator of type R

The synthesis goal of a power R-gyrator is designing a switching structure characterized by the following steady-state equations

$$V_1 = rI_2 \tag{2.61}$$

$$V_2 = rI_1 \tag{2.62}$$

where r is the gyrator resistance.

As stated previously, switching structures used in the design of power gyrators are not versatile, i.e., a G-gyrator cannot be adapted to perform R-gyrator functions. It has to be pointed out that a current source at the input port of the circuit depicted in Fig. 2.5 is not compatible with the series inductor and therefore such circuit cannot be used for the current-voltage transformation. Hence, the block diagram of a power R-gyrator can be represented as shown in Fig. 2.42 where i_g is the input current source to be transformed into an output voltage source by means of the gyrator action. It can be observed that $S(x) = 0$ in steady-state, i.e., $V_2 = rI_g$ which implies $V_1 = rI_2$.

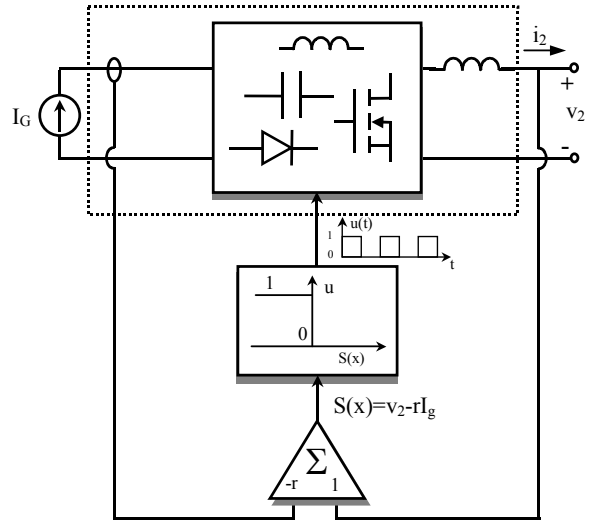

Fig. 2.42 *Block diagram of a dc-to-dc switching regulator operating in sliding-mode with R-gyrator characteristics.*

The most simple converters with the topological constraints depicted in the block diagram of Fig. 2.42 are shown in Fig. 2.43. Such converters are derived by slight modification of the BOF converter, Cuk converter and Cuk converter with galvanic isolation. Note that series connection of a voltage source and an inductor at the input port of the BOF and Cuk converters depicted in Fig. 2.6 has been substituted by a current source, this implying a dynamic order reduction to a third-order system.

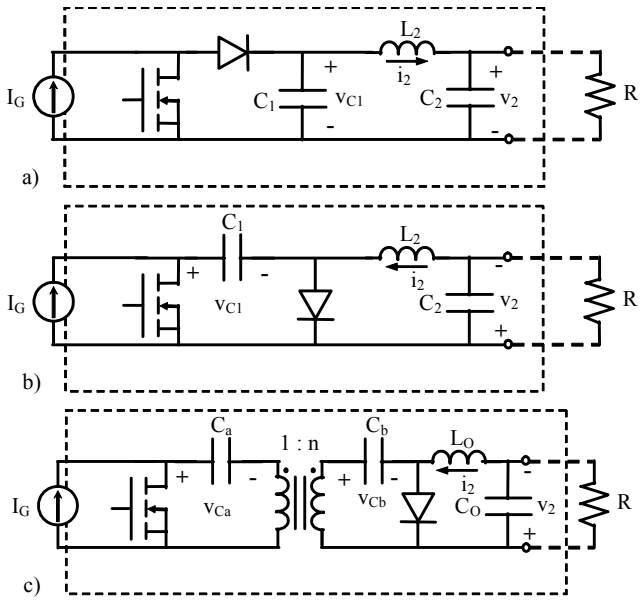

Fig. 2.43 *Current to voltage dc-to-dc switching converters with non-pulsating input and output currents a) boost converter with output filter b) Čuk converter c) Čuk converter with galvanic isolation*

2.2.2.1 Power gyrator of type R with variable switching frequency

In this section we will analyze the BOF converter and the Cuk converter in sliding-mode with the constraint imposed by the R-gyrator equation $S(x) = v_2 - rI_g$.

2.2.2.1.1 Analysis of the BOF converter as a power R-gyrator with variable switching frequency

In the continuous conduction mode, the BOF converter depicted in Fig. 2.38 can be represented in compact form by the following set of differential equations

$$\begin{aligned} \frac{di_2}{dt} &= \frac{v_{C1} - v_2}{L_2} \\ \frac{dv_{C1}}{dt} &= \frac{I_g}{C_1}(1-u) - \frac{i_2}{C_1} \\ \frac{dv_2}{dt} &= \frac{i_2}{C_2} - \frac{v_2}{RC_2} \end{aligned} \tag{2.63}$$

It can be easily shown that assuming $S(x) = v_2 - rI_g$ as sliding surface does not result in sliding motions in the system described by (2.63) since the transversal condition for the existence of equivalent control is not accomplished. Although no sliding motions can be induced on the surface $S(x)=v_2 - rI_g$, it has been proved empirically by means of simulations that the system can exhibit stable limit cycle behavior of the type reported [37] for certain parameter values. However, considering a sliding surface such as $S(x) = v_{C1} - rI_g$ results in an equivalent control $u_{eq}(x) = 1 - \frac{i_2}{I_g}$ which eventually yields a stable dynamic behavior with R-gyrator characteristics. The resulting characteristic equation is given by

$$s^2 + s\frac{1}{RC_2} + \frac{1}{L_2C_2} = 0 \tag{2.64}$$

which corresponds to a stable system.

Figures 2.44-2.46 show the PSPICE simulations of a BOF converter-based R-gyrator with the set of parameters $I_g = 10$ A, $R = 5\ \Omega$, $r = 2\ \Omega$, $C_1 = 20\ \mu$F, $L_2 = 12\ \mu$H and $C_2 = 2\ \mu$F. Figure 2.44 illustrates the gyrator start-up. It can be observed that the circuit has gyrator characteristics in steady-state given by $V_2 = rI_g$. Figure 2.45 shows the gyrator response to ± 2 A input current variations of step type superposed on the nominal input current I_g. Note that v_2 follows proportionally the input current evolution as it can be expected. Finally, figure 2.46 illustrates the voltage source nature of the system output voltage by showing that capacitor voltage v_{C1} remains constant in spite of the ± 50 % load changes of step type.

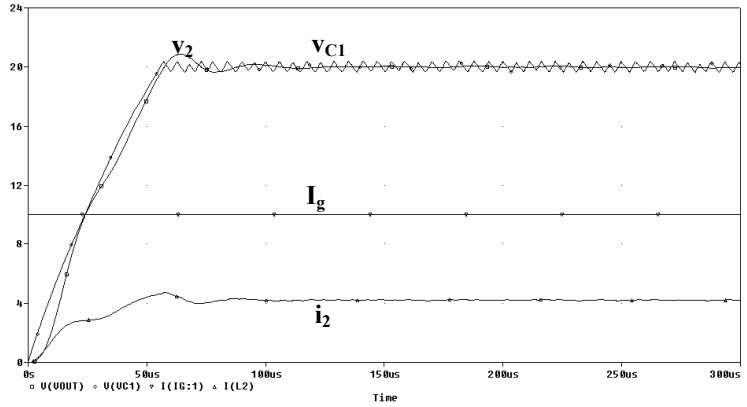

Fig. 2.44 *Simulated behavior of a BOF converter-based R-gyrator during start-up*

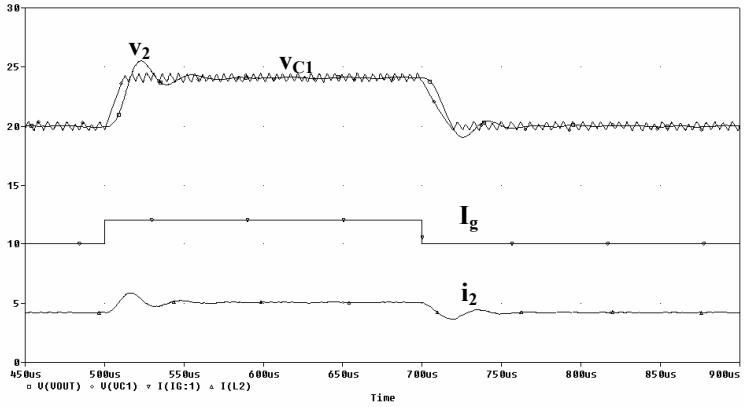

Fig. 2.45 *Simulated response of a BOF converter-based R-gyrator to a pulsating input current.*

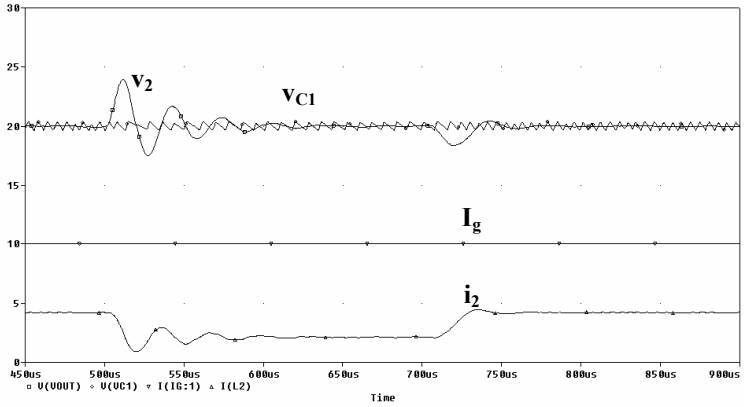

Fig. 2.46 *Simulated response of a BOF converter-based R-gyrator to a pulsating load*

Figure 2.47 illustrates the practical implementation of a BOF converter-based R-gyrator for the set of parameters $I_g = 10$ *A*, $C_1 = 20$ *μF*, $L_2 = 12$ *μH*, $C_2 = 2$ *μF*, $r = 2$ Ω and $R = 4.7$ Ω. The input current source has been implemented by means of the BIF converted-based G-gyrator developed in 2.2.1.1.1. This new switching structure will be described later in Chapter 3. Figure 2.48 shows the gyrator behavior during start-up. The gyrator characteristics given by equations

(2.61)-(2.62) can be easily observed in the steady-state region of Fig. 2.48. The R-gyrator delivers 91 W to the load with an efficiency of 89 %.

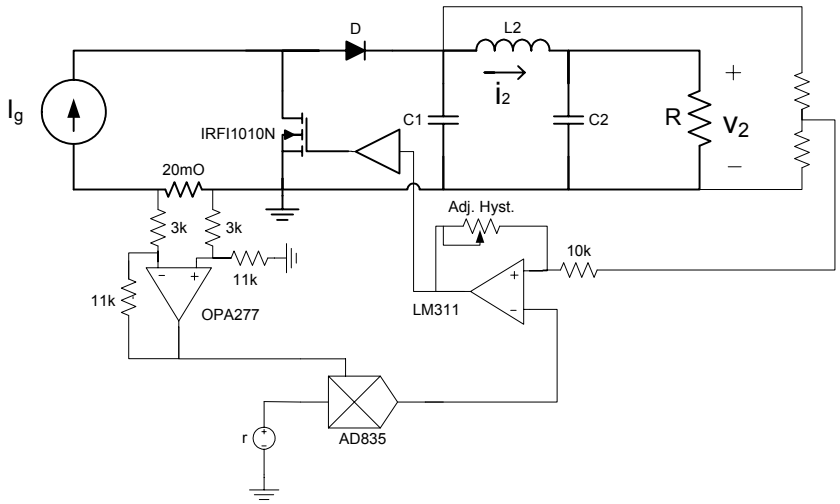

Fig. 2.47 *Practical implementation of a BOF converter-based R-gyrator. I_g=10 A, C_1 = 20 μF, L_2 = 12 μH, C_2 = 2 μF, r = 2 Ω and R= 4.7 Ω .*

Fig. 2.49 illustrates the effect of a pulsating current superposed on the nominal input current. The state variables switch between two steady-states in which the output voltage (voltage at capacitor C_1) is proportional to the input current with a proportionality factor $r = 2\ \Omega$. Finally, the voltage source nature of the output voltage (V_{C1}) is illustrated in Fig. 2.50 by showing that capacitor voltage V_{C1} remains constant is spite of the ± 50 % step changes in the load. It has to be pointed out that experimental results shown in figures 2.48-2.50 are in good agreement with the corresponding simulations depicted in figures 2.44-2.46.

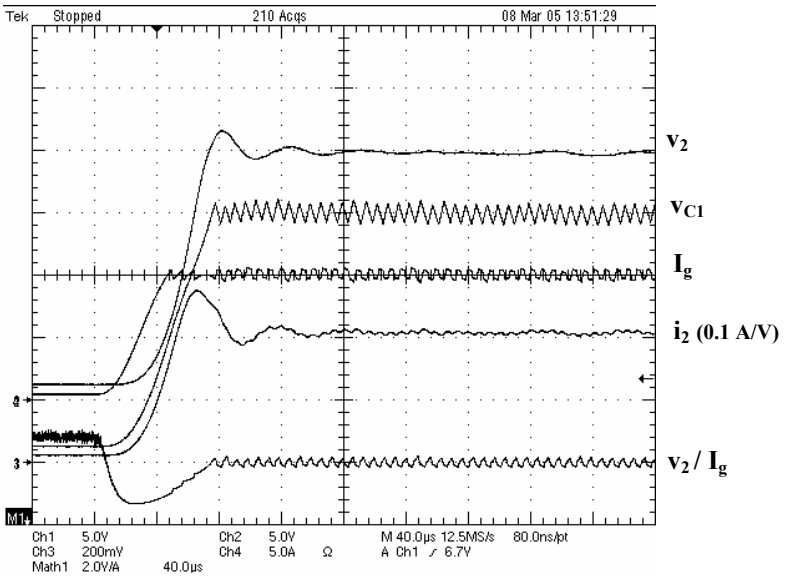

Fig. 2.48 *Experimental behavior of a BOF converter-based R-gyrator during start-up*

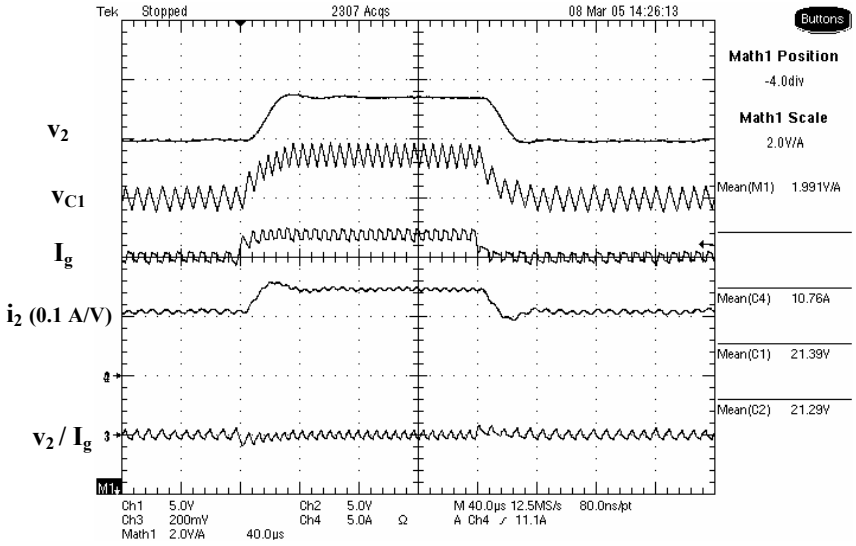

Fig. 2.49 Experimental response of a BOF converter-based R-gyrator to a pulsating input current.

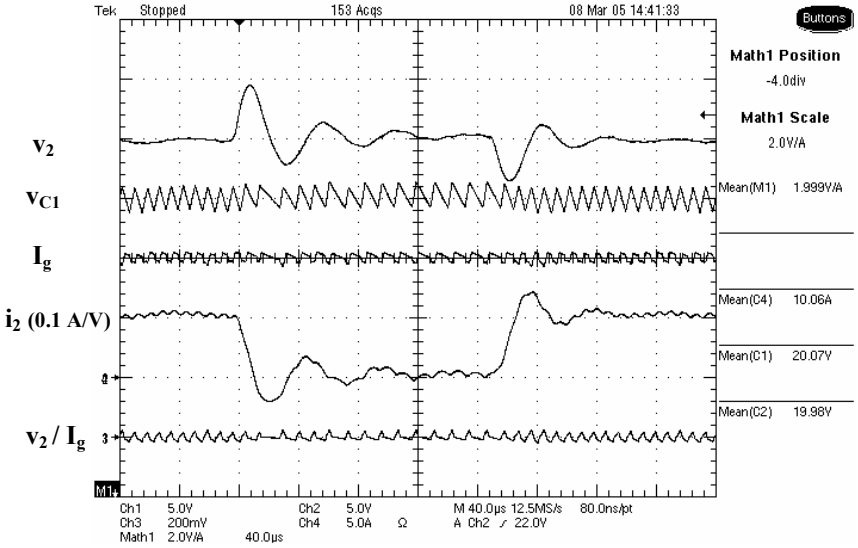

Fig. 2.50 Experimental response of a BOF converter-based R-gyrator to a pulsating load

2.2.2.1.2 Analysis of the Cuk converter as a power R-gyrator with variable switching frequency

In the continuous conduction mode, the Cuk converter depicted in Fig. 2.38 can be described by the following set of differential equations

$$\begin{aligned}\frac{di_2}{dt} &= \frac{v_{C1}}{L_2}u - \frac{v_2}{L_2}\\ \frac{dv_{C1}}{dt} &= \frac{I_g}{C_1}(1-u) - \frac{i_2}{C_1}u\\ \frac{dv_2}{dt} &= \frac{i_2}{C_2} - \frac{v_2}{RC_2}\end{aligned} \tag{2.65}$$

Assuming $S(x) = v_2 - rI_g$ as a sliding surface and imposing the invariance conditions $S(x) = 0$ and $\frac{dS}{dt} = 0$ in (2.65) results in the equivalent control

$$u_{eq}(x) = \frac{v_2}{v_{C1}} \tag{2.66}$$

The introduction of (2.66) in (2.65) leads to the following ideal sliding dynamics

$$g_1(x) = \frac{dv_{C1}}{dt} = \frac{I_g}{C_1}\left(1 - \frac{v_2}{v_{C1}}\right) - \frac{I_2}{C_2}\frac{v_2}{v_{C1}} \tag{2.67}$$

The coordinates of the equilibrium point are

$$x^* = \left[\frac{r}{R}I_g,\ \frac{I_g r(r+R)}{R},\ rI_g\right]^+ \tag{2.68}$$

where it can be observed that $V_2 = rI_g$ and $V_1 = V_{C1} + V_2 = rI_2$.

Linearizing (2.67) around the equilibrium point (2.68) results in the differential equation

$$\frac{dv_{C1}}{dt} = \frac{1}{C_1}\frac{R}{r(R+r)} \tag{2.69}$$

represents an unstable system.

It can be also demonstrated that the insertion of a damping network R_d-C_d of the type depicted in Fig. 2.7 cannot stabilize the system.

2.2.2.2 Power gyrator of type R with constant switching frequency

Using the transformation of a sliding-mode control system into a PWM control system described in 2.2.1.2.1, results in a stable PWM R-gyrator in the case of the BOF converter. The expression of the control law is given by

$$\Gamma(x(t)) = 1 - \left(\frac{rI_g - v}{R_K I_g} + \frac{v}{RI_g}\right) \tag{2.72}$$

and the corresponding characteristic equation is

$$\left(s+\frac{1}{R_K C}\right)\left(s^2+s\frac{1}{RC_2}+\frac{1}{L_2C_2}\right)=0 \qquad (2.73)$$

Figs. 2.51-2.53 show the PSPICE simulations of a BOF converter operating as a PWM R-gyrator with the set of parameters I_g= *10 A*, R= *4 Ω*, r = *2 Ω*, C_1 = *20 μF*, R_K = *0.01 Ω* L_2 = *12 μH*, C_2 = *2 μF* and a switching frequency of *200 kHz*.

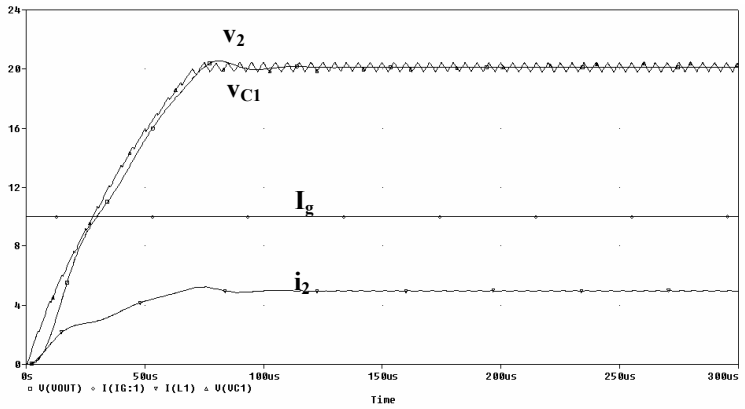

Fig. 2.51 Start-up of a BOF converter as PWM gyrator

The gyrator start-up from zero initial conditions is shown in Fig. 2.51 where it can be observed that the steady-state is reached after a fast transient-state with a very small overshoot. It has to be pointed out that the converter behaves as a power gyrator of type R in perfect agreement with equations (2.61)-(2.62).

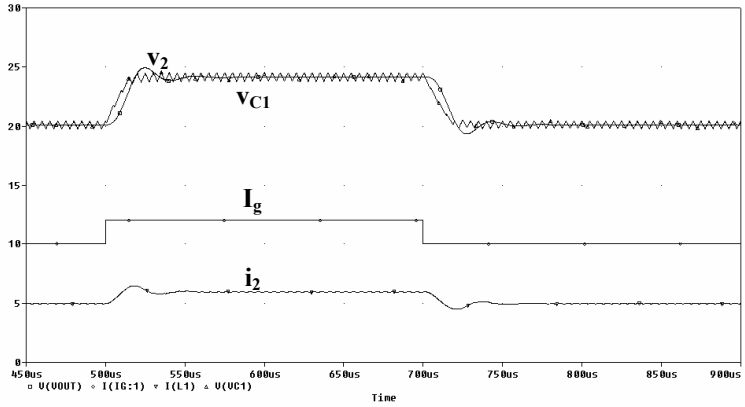

Fig. 2.52 Response of a BOF converter-based PWM R-gyrator to a pulsating input current

Fig. 2.52 illustrates the effect of a pulsating current superposed on the nominal input current. The state variables switch between two steady-states in which the output voltage (voltage at capacitor C_1) is proportional to the input current with a proportionality factor r = *2* Ω. Finally,

the voltage source nature of the output voltage (V_{C1}) is depicted in Fig. 2.53 after introducing ± 50 % perturbations in the load resistance.

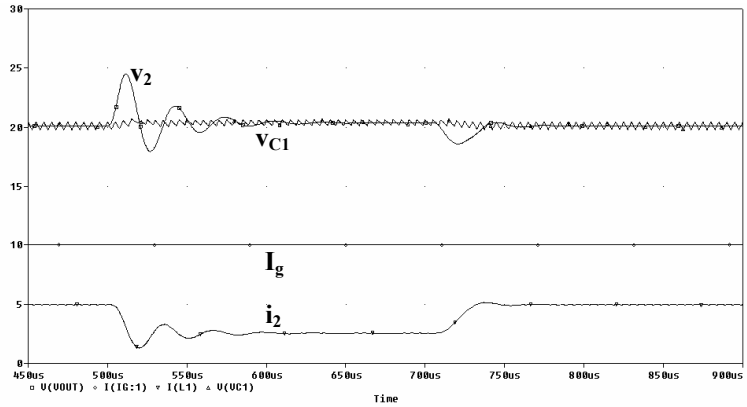

Fig. 2.53 Response of a BOF converter-based PWM R-gyrator to a pulsating load

2.3 Semigyrator definition

A power semigyrator is defined as a switching converter satisfying equations (2.1)-(2.2) or, equivalently, (2.61)-(2.62) in which either the input current or the output current is pulsating. As reported in [22], there are many converters with pulsating behavior in one port and a series inductor in the other port. In this thesis, we have limited our investigation to the canonical structures buck, and boost for simplicity reasons. We have neglected the study of a buck-boost converter due to the non-pulsating nature of both input and output currents. This fact does not make possible a sliding-mode control of any of these currents.

2.3.1 Semigyrator of type G

The synthesis of G-semigyrator is similar to that explained in 2.2.1.1 for the synthesis of G-gyrators, whose aim is to find converter structures satisfying equations (2.1)-(2.2). Fig. 2.54 shows the block diagram of a switching regulator with G-semigyrator characteristics operating at variable switching frequency. In the case of G-semigyrators, the series inductor with the output port is mandatory in order to induce a sliding regime to the output current.

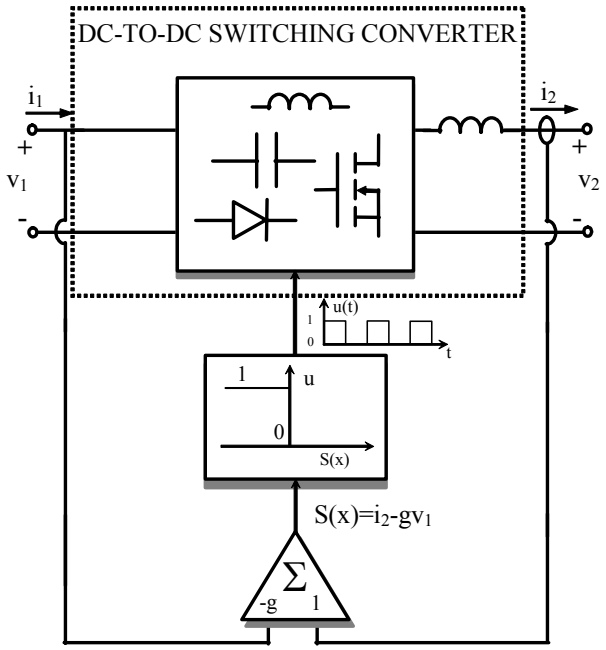

Fig. 2.54 *Block diagram of a dc-to-dc switching regulator operating in sliding-mode with G-semigyrator characteristics.*

2.3.1.1 Semigyrator of type G with variable switching frequency

From the block diagram of Gig. 2.54 it can be derived that the only switching structure that can be used as a candidate for a G-semigyrator is a buck converter (Fig. 2.55).

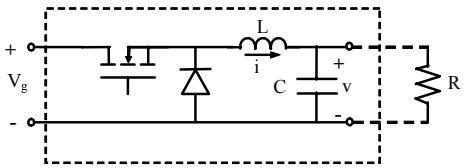

Fig. 2.55 *Buck converter*

The buck converter depicted in Fig. 2.43 can be described by the following set of differential equations

$$\begin{aligned} \frac{di}{dt} &= \frac{V_g}{L}u - \frac{v}{L} \\ \frac{dv}{dt} &= \frac{i}{C} - \frac{v}{RC} \end{aligned} \tag{2.74}$$

Assuming $S(x) = i_2 - gV_g$ as a sliding surface and imposing the invariance conditions $S(x)=0$ and $\frac{dS}{dt} = 0$ in (2.74) result in the equivalent control.

$$u_{eq}(x) = \frac{v}{Vg} \tag{2.75}$$

Substituting u by $u_{eq}(x)$ in (2.74) leads to the following ideal sliding dynamics

$$\frac{dv}{dt} = \frac{gV_g}{C} - \frac{v}{RC} \tag{2.76}$$

The solution of the first-order differential equation is

$$v = Ae^{-\frac{t}{RC}} + gRV_g \tag{2.77}$$

where A is a constant given by the initial conditions.
From (2.77) we deduce that the steady-state response will be given by

$$V = gRV_g \tag{2.78}$$

which implies

$$I = gV_g \tag{2.79}$$

Note that (2.79) corresponds to the desired gyrator behavior at the output port. The complementary gyrator characteristics at the input port are fixed by the POPI nature of the buck converter. However, it has to be pointed out that the input current is pulsating and therefore the expected EMI levels will be bigger than in the case of BIF converter-based gyrator

Figs. 2.56 and 2.57 show the PSIM simulations of a buck converter-based g-semigyrator with the set of parameters *Vg = 20 V, R = 1 Ω, g = 0.5 Ω^{-1}, L = 35 μH and C = 6.6 μF*.

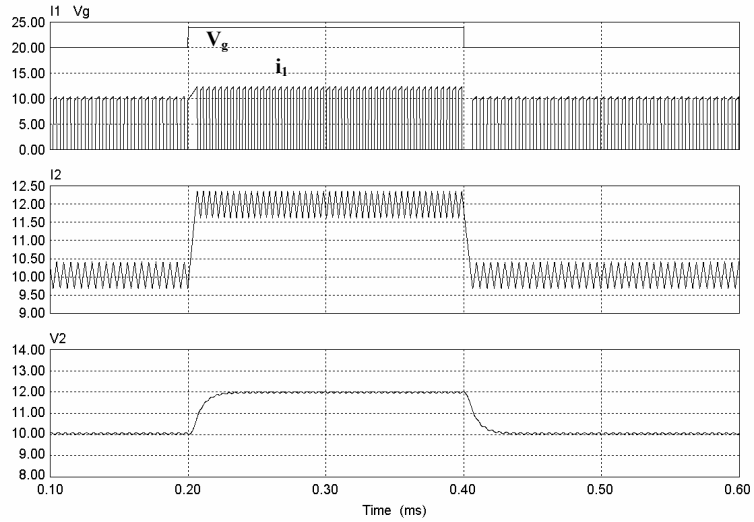

Fig. 2.56 Simulated response of a buck converter-based G-semigyrator in sliding-mode to a pulsating input voltage.

Fig. 2.56 illustrates the semigyrator response to input voltage variations of ± 4 V of step type superposed on the nominal input voltage. These variations are reproduced proportionally by the output current this verifying the expected gyrator characteristics at the output port.

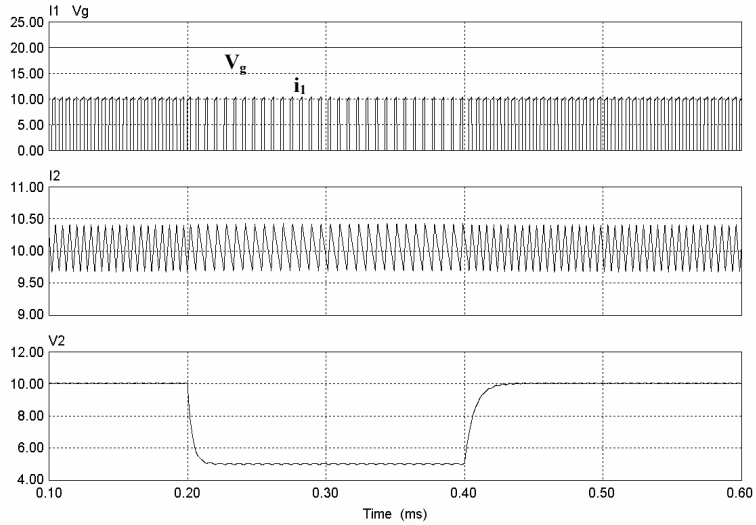

Fig. 2.57 *Simulated response of a buck converter-based G-semigyrator in sliding-mode to a pulsating load*

Fig. 2.57 shows the semigyrator response to step changes of ± 50 % in the load resistance. Note that the output current remains constant, this verifying the current source nature of this current, and therefore the expected gyrator behavior.

The BIF converter-based G-gyrator depicted in Fig. 2.8 has been adapted to implement a G-semigyrator. As shown in Fig. 2.58. The input filter L_1-C_1 and the camping networks R_aL_a and R_dC_d have been suppressed. The set of parameters are those used in the simulations of figs. 2.56 and 2.57.

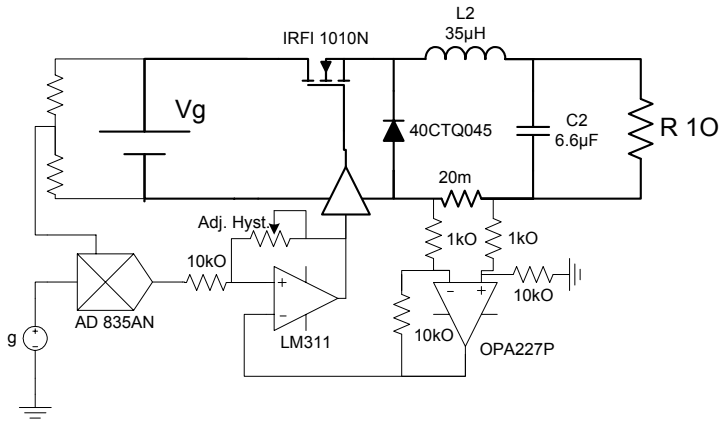

Fig. 2.58 *Practical implementation of a buck converter-based G-semigyrator. Vg = 20 V, R = 1 Ω, g = 0.5 Ω^{-1}, L = 35 µH, C = 6.6 µF.*

Figures 2.59 and 2.60 illustrate the experimental behavior of the G-semigyrator. The nominal power delivered to the load is 103 W with an efficiency of 91.1 %. Figure 2.59 shows the semigyrator response to ± 4 V step perturbations superposed on the input voltage. Figure 2.48, in turn, depicts the semigyrator response to load variations.

It can be observed that the experimental results of figures 2.59 and 2.60 are in good agreement with the simulations shown in figs. 2.56 and 2.57 respectively.

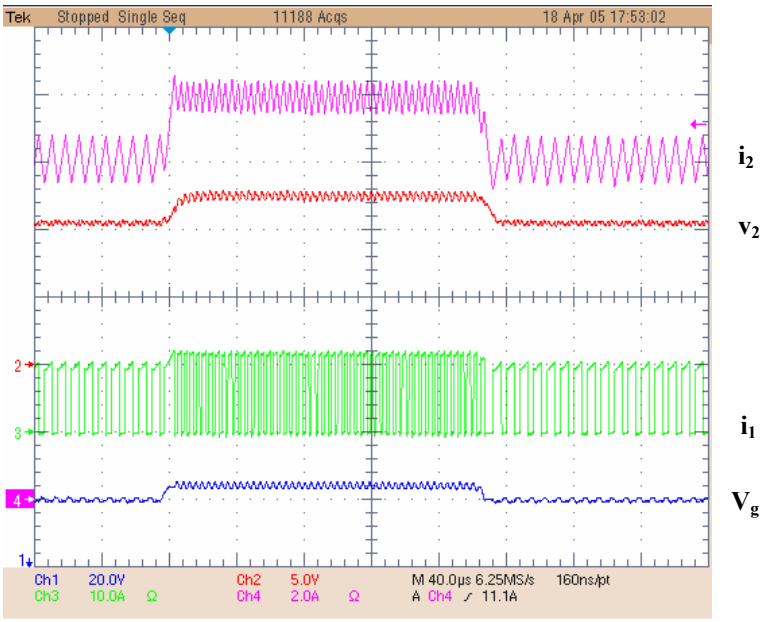

Fig. 2.59 *Experimental response of a buck converter-based G-semigyrator in sliding-mode to a pulsating input voltage.*

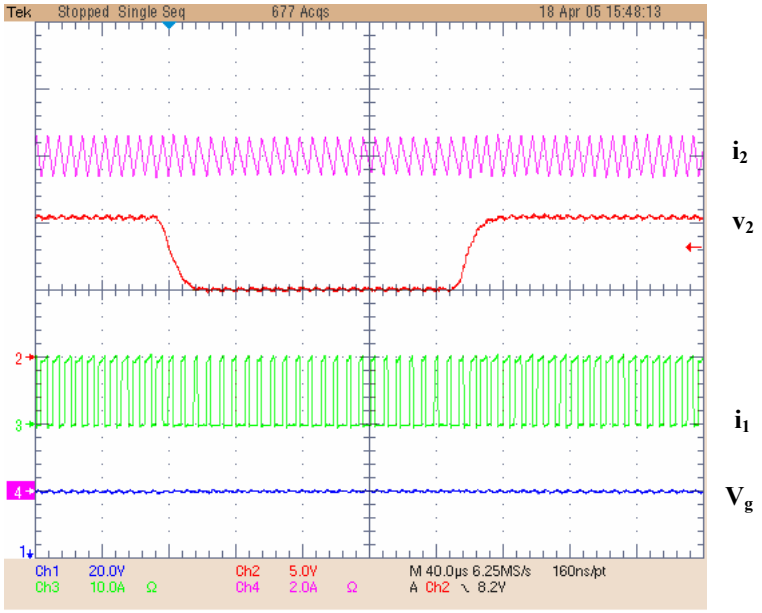

Fig. 2.60 *Experimental response of a buck converter-based G-semigyrator in sliding-mode to a pulsating load.*

2.3.1.2 Semigyrator of type G with constant switching frequency

We'll make use of the method employed in 2.2.1.2 to derive the PWM nonlinear control law in the case of G-semigyrators.

Considering again the set of equations (2.74) describing the buck converter dynamics, we will substitute the discrete variable u by Γ which corresponds to the averaged value of u in each switching cycle. Thus, the inductor dynamics will be given by

$$\frac{di}{dt} = \frac{-v}{L} + \Gamma \frac{V_g}{L} \tag{2.80}$$

If equation (2.80) could be expressed as

$$\frac{di}{dt} = \frac{R_K}{L}\left(gV_g - i\right) \tag{2.81}$$

would result in the steady-state identity

$$I = gV_g \tag{2.82}$$

which characterizes a gyrator behavior.

The control law yielding (2.81) is given by

$$\Gamma(x) = \frac{v + R_K\left(gV_g - i\right)}{V_g} \tag{2.83}$$

The resulting dynamics can be described by the following characteristic equation

$$\left(s + \frac{R_K}{L}\right)\left(s + \frac{1}{RC}\right) = 0 \tag{2.84}$$

which corresponds to a stable system.

Figures 2.61 and 2.62 show the PSIM simulations of a PWM G-semigyrator for the set of parameters *Vg = 20 V, R = 1 Ω, g = 0.5 Ω*$^{-1}$*, L = 35 μH, C = 6.6 μF, F= 200 kHz* and R_K*= 200* Ω.

Fig. 2.49 illustrates the semigyrator response to step type input voltage variations of ± 4 V. It can be observed that current i_2 follows with a proportional factor the V_g variations.

On the other hand, the nature of current source at the output port has been verified as shown in Fig. 2.50. There, the step changes in the load resistance are proportionally reproduced by output voltage, the output current being the proportionality factor.

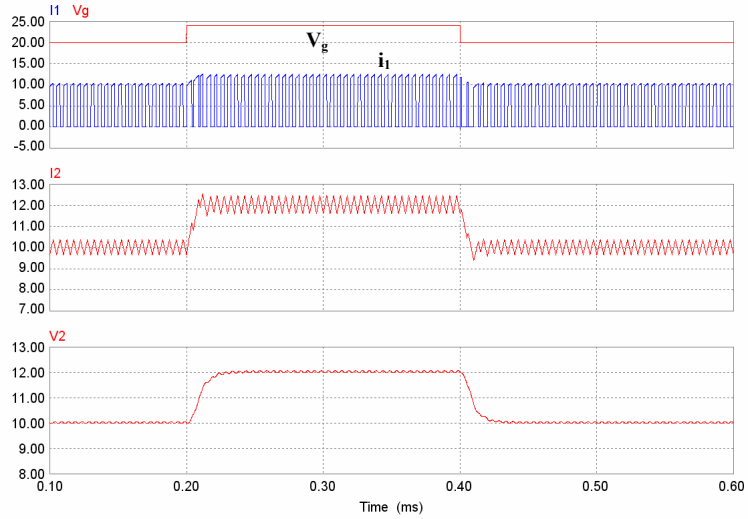

Fig. 2.61 *Simulated behavior of the buck converter-based PWM G-semigyrator to a pulsating input voltage*

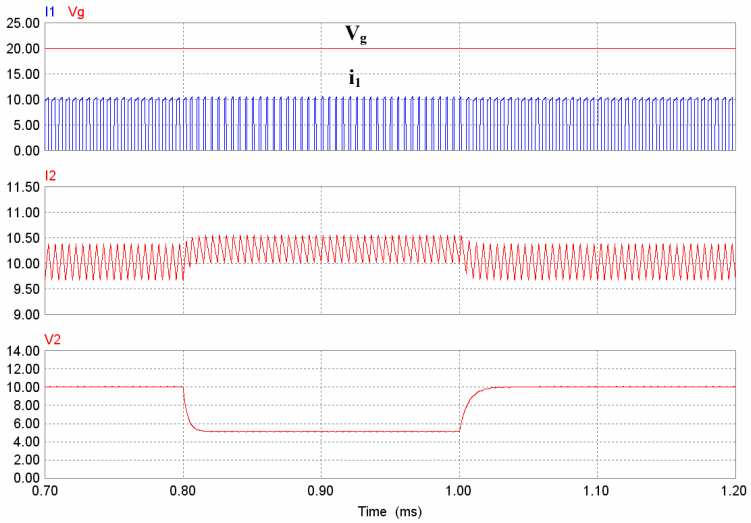

Fig. 2.62 *Simulated behavior of the buck converter-based PWM G-semigyrator to a pulsating load*

2.3.2 Semigyrator of type R

The synthesis of R-semigyrators will follow the same steps described in 2.2.2 for the realization of R-gyrators. Considering again the block diagram of Fig. 2.37, note that a potential structure for a semigyrator of type R will require a pulsating current at the output port. As reported in [22], there are several converters satisfying this constraint. We have limited our investigation to the most simple candidate, i.e., the boost-shunt [31] structure depicted in Fig. 2.63.

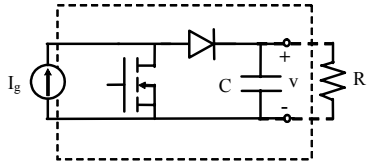

Fig. 2.63 Boost-shunt converter

2.3.2.1 Semigyrator of type R with variable switching frequency

The boost-shunt converter is a first-order circuit that can be represented by the following differential equation

$$\frac{dv}{dt} = \frac{I_g}{C}(1-u) - \frac{v}{RC} \tag{2.85}$$

Assuming $S(x) = v - rI_g$ as a sliding surface leads to the equivalent control

$$u_{eq}(x) = 1 - \frac{v}{RI_g} \tag{2.86}$$

which results in the following ideal zero-order sliding dynamics

$$\frac{dv}{dt} = 0 \tag{2.87}$$

and

$$v = V = rI_g \tag{2.88}$$

Therefore, the converter behaves a R-gyrator.

Figures 2.64 and 2.65 show the PSIM simulations of a boost-shunt converter-based R-semigyrator for the set of parameters $I_g = 10$ *A,* $r = 2$ Ω, $C = 20$ *μF and* $R = 4$ Ω. Figure 2.64 illustrates the semigyrator response to step type input current variations of ± 2 A superposed to the nominal input current I_g. Note that the output voltage follows proportionally the input current.

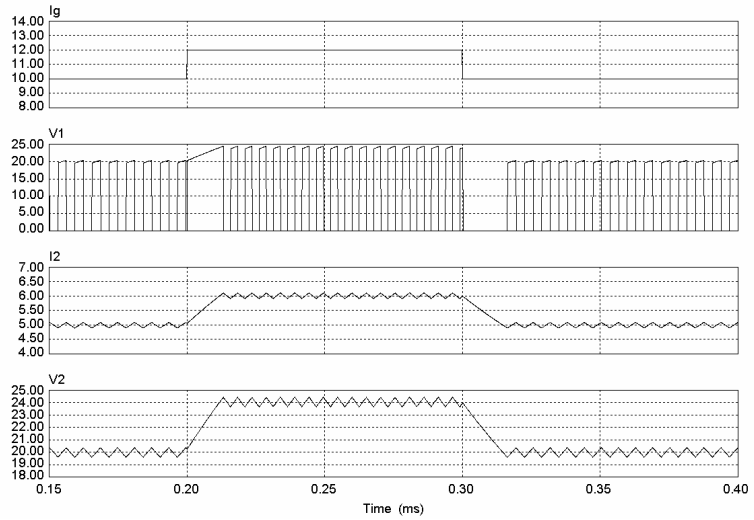

Fig. 2.64 *Simulated response of a boost-shunt converter-based R-semigyrator in sliding-mode to a pulsating input current.*

Also, the semigyrator response to step type load variations of ± 50 % is shown in Fig. 2.65. In this case, it has to be pointed out that the output voltage remains constant since it only depends on the input current value. It can be observed that the gyrator equation $V_1 = r\, I_2$ is preserved since there is a proportional relation between the output current and the averaged value of the input voltage.

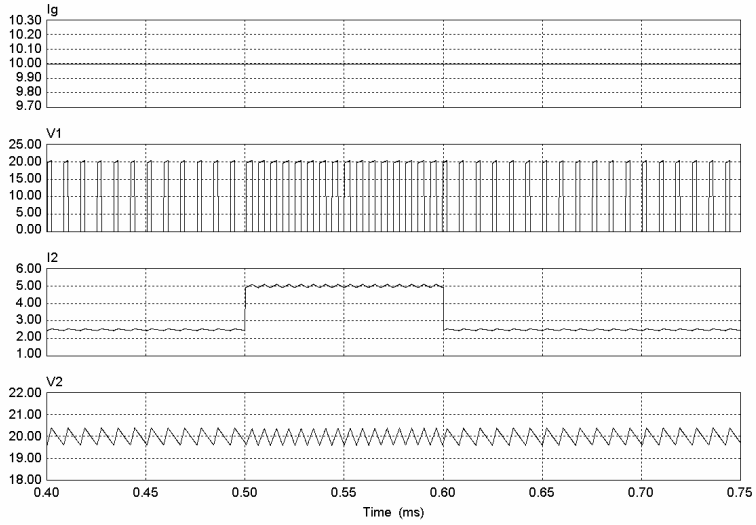

Fig. 2.65 *Simulated response of a boost-shunt converter-based R-semigyrator in sliding-mode to a pulsating load.*

2.3.2.1.1 *Semigyrator of type R with variable switching frequency based on the boost converter*

Considering again the equations defining a power gyrator of type R, we observe that the equation $V_2 = rI_1$ can be imposed by means of a sliding regime provided that i_1 is a continuous variable, i.e., an inductor current. Therefore, a boost converter, as shown in Fig. 2.66, could be also a candidate for a R-semigyrator realization.

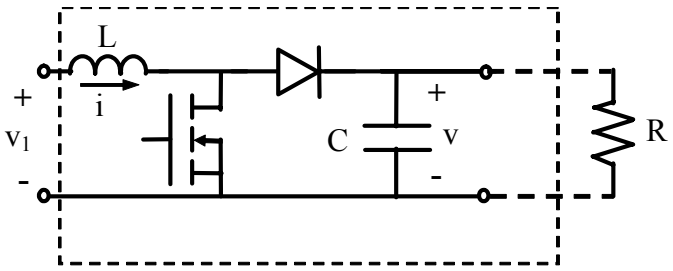

Fig. 2.66 Boost converter

The analysis of the sliding-mode induced by considering $S(x) = V_2 - rI_1$ results in a stable equilibrium point, the characteristic equation being

$$\left(s + \frac{r^2}{R(r^2C + L)} \right) = 0 \tag{2.89}$$

The practical implementation of a boost-converter-based R-semigyrator is shown in Fig. 2.67 for the set of parameters $V_g = 10\ V$, $L = 75\ \mu H$, $r = 2\ \Omega$, $C = 20\ \mu F$ and $R = 5\ \Omega$.

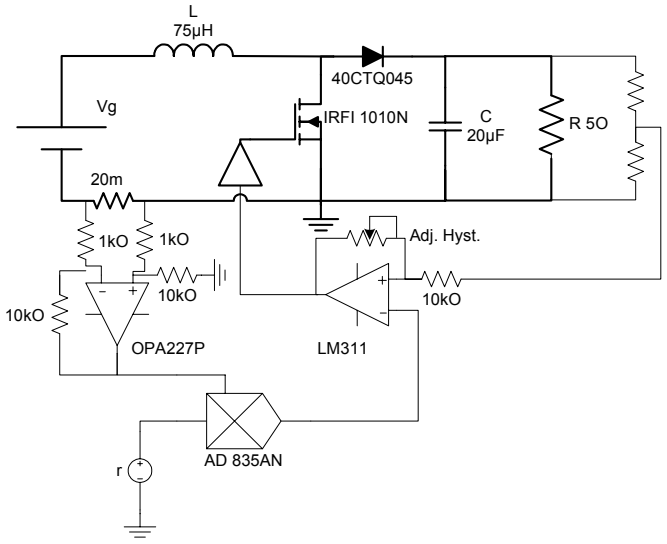

Fig. 2.67 Practical implementation of a boost converter-based R-semigyrator. Vg = 10 V, R = 5 Ω, r = 2 Ω, L = 75 µH, C = 20 µF.

Figures 2.68 and 2.69 show respectively the simulated and experimental responses of the semigyrator to step changes in the input voltage of ± 4 V superposed to the nominal voltage. Note that in both figures, the division v / i_1 has been also represented. The averaged value of this division is 2 Ω which corresponds to the averaged value imposed by the sliding surface. The semigyrator delivers 106 W with an efficiency of 92 % operating at a nominal switching frequency of 100 kHz.

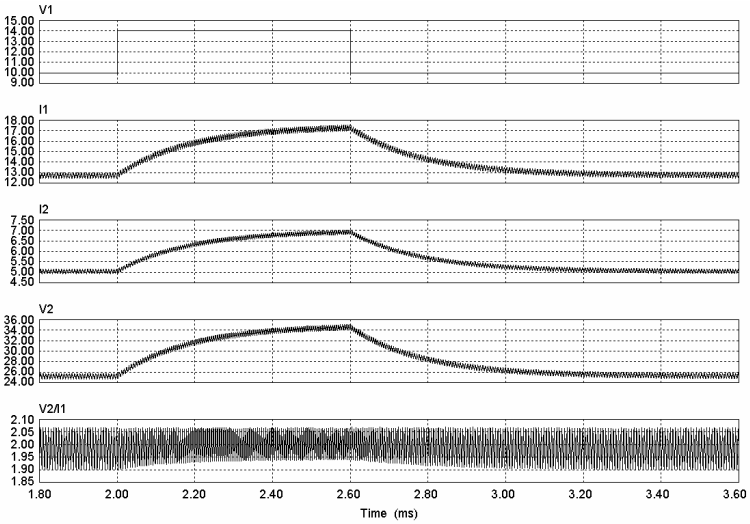

Fig. 2.68 *Simulated response of a boost converter-based R-semigyrator in sliding-mode to a pulsating input voltage.*

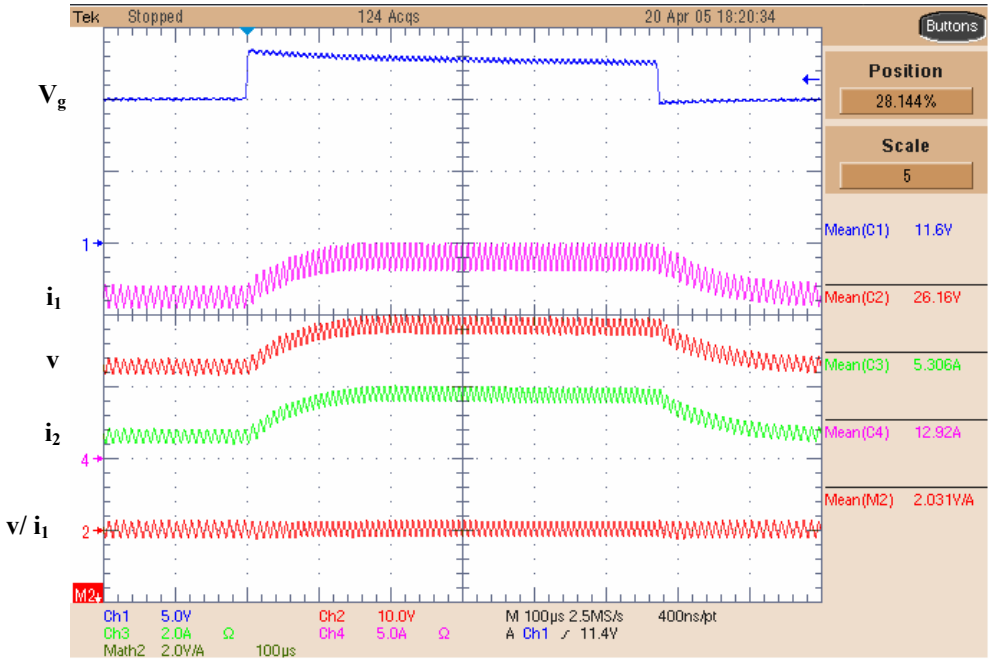

Fig. 2.69 *Experimental response of a boost converter-based R-semigyrator in sliding-mode to a pulsating input voltage*

Finally, figures 2.70 and 2.71 show respectively the simulated and experimental responses of the semigyrator to step changes in the output load passing from 5 Ω to 6 Ω and then to 5 Ω.

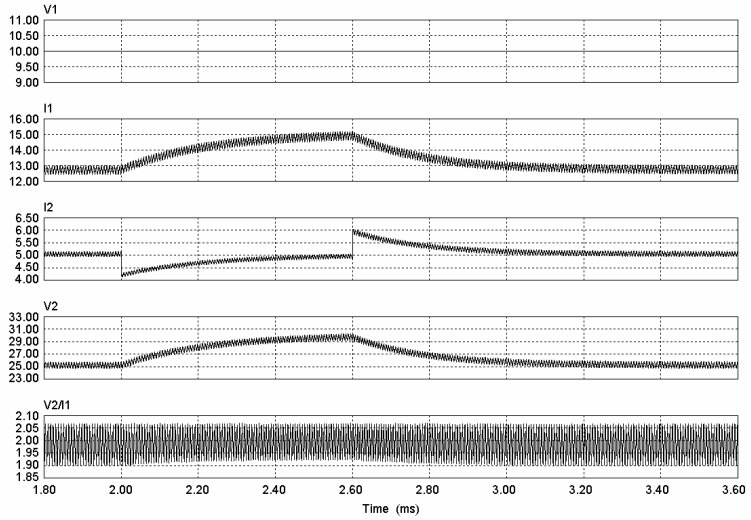

Fig. 2.70 *Simulated response of a boost converter-based R-semigyrator in sliding-mode to a pulsating load*

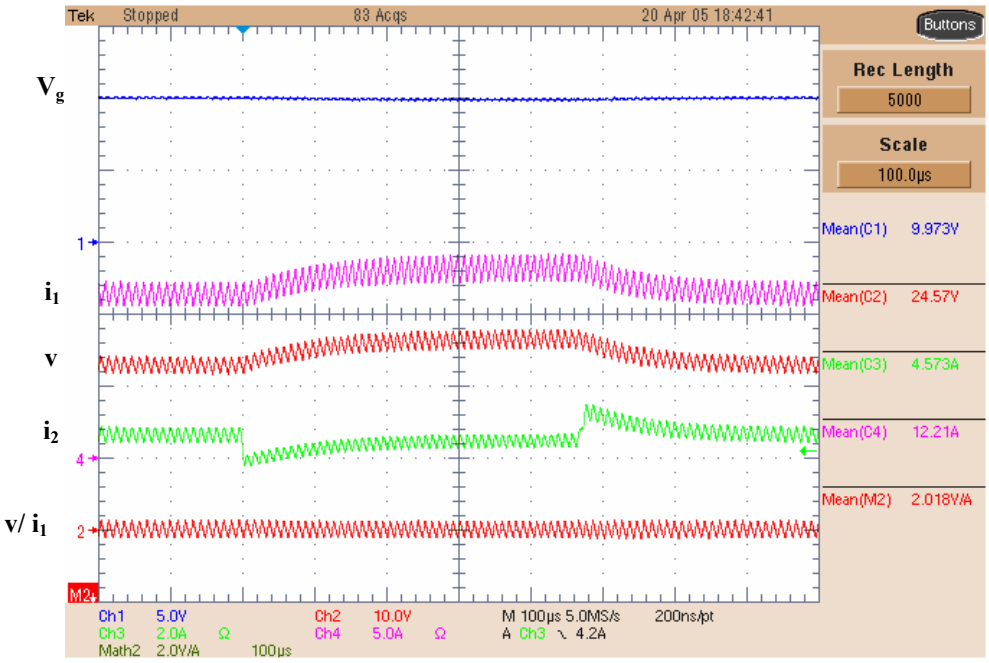

Fig. 2.71 *Experimental response of a boost converter-based R-semigyrator in sliding-mode to a pulsating load*

In all cases, the experimental results are in good agreement with the simulations.

2.3.2.2 Semigyrator of type R with constant switching frequency

By using the method employed in 2.2.1.2 and 2.3.1.2 to derive a PWM nonlinear control law, we can synthesize a R-semigyrator operating at constant switching frequency.

Considering again the first-order differential equation of the boost-shunt converter

$$\frac{dv(t)}{dt} = \frac{I_g}{L}(1-\Gamma) - \frac{v}{RC} \tag{2.90}$$

If equation (2.90) could be expressed as

$$\frac{dv(t)}{dt} = \frac{rI_g - v}{R_K C} \tag{2.91}$$

would result in the steady-state identity

$$v = rI_g \tag{2.92}$$

which characterizes a gyrator behavior.

The control law leading to (2.92) is given by

$$\Gamma(x) = 1 - \left(\frac{v - rI_g}{R_K I_g} + \frac{v}{RI_g} \right) \tag{2.93}$$

Note that the resulting dynamics is given by equation (2.90) which represents a stable system.

Figures 2.72 and 2.73 show the PSIM simulations of a PWM boost-shunt converter-based R-semigyrator for the set of parameters V_g = *10 V, L = 75 μH, r = 2* Ω *, F= 200 kHz,* $R_K = 10^{-2}$ Ω, *C= 20 μF* and *R= 5* Ω.

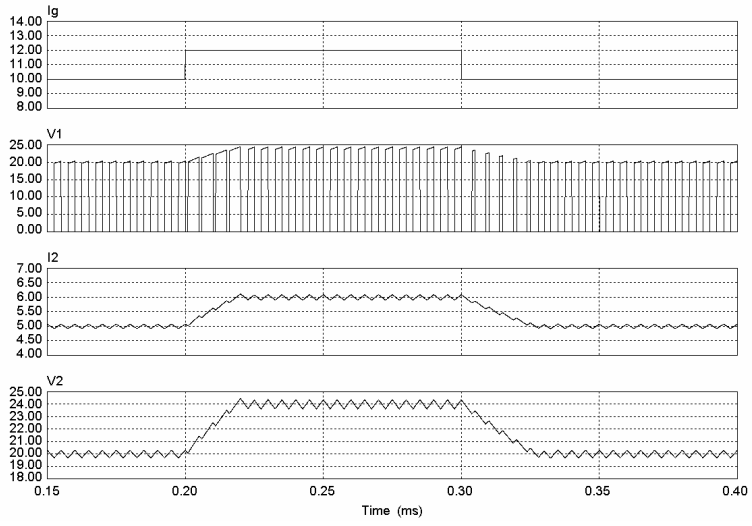

Fig. 2.72 Simulated response of a PWM boost-shunt converter-based R-semigyrator to a pulsating input current.

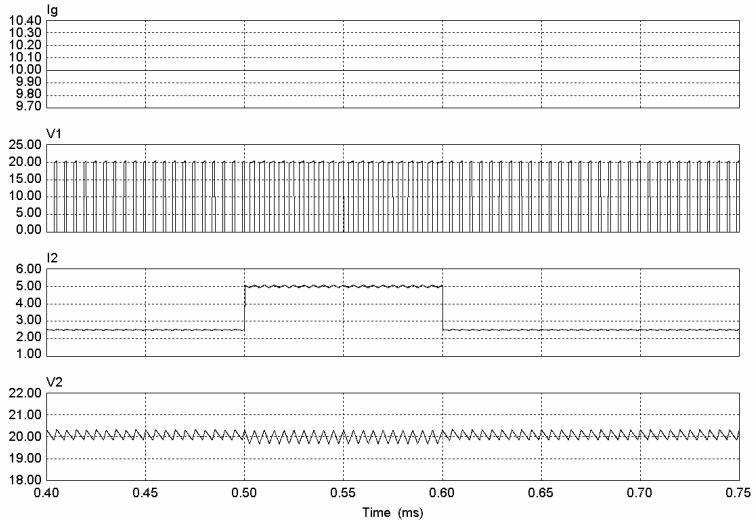

Fig. 2.73 Simulated response of a PWM boost-shunt converter-based R-semigyrator to a pulsating load.

The semigyrator behavior for a step change of ± 2 A of the input current is illustrated in Fig. 2.72. It can be observed that the output voltage follows proportionally the input current with a constant switching period. On the other hand, the response of the PWM R-semigyrator to step changes of the load resistance is depicted in Fig. 2.61. In this case, the load resistance changes from 5 Ω to 6 Ω and returns to 5 Ω. The output voltage remains constant and proportional to the input current and the resistance change is reproduced by the output current.

2.4 Conclusion

In this chapter, the foundations for a systematic design of power gyrators have been established. Power gyrators have been classified into two categories: G-gyrators and R-gyrators. The G-gyrators transform a voltage source into a current source while the R-gyrator perform the conversion of a current source into a voltage source

It has been found that both BIF and Cuk converters can exhibit stable G-gyrator characteristics if damping networks are inserted and certain stability conditions are accomplished. It has been also defined the notion of semigyrator and it has been demonstrated that a buck converter-based G-semigyrator is always stable.

With regard to R-gyrators, it has been shown that BOF a converter is always stable for a sliding surface $S(x) = V_{C1} - Ig$. It has been also found empirically, by means of simulation, that this converter has a stable limit cycle for the control law $S(x) = V_2 - I_g$. Moreover, both boost and boost-shunt converters exhibit stable sliding modes over the surface $S(x) = V_2 - I_g$ and therefore can be considered as R-semigyrators.

In addition, G-gyrators with controlled input current have been investigated. It can be concluded that both BOF and Cuk converter exhibit unconditionally stable gyrator characteristics. Also, it has been empirically shown by means of simulation that the BIF converter has a stable limit cycle in steady-state with gyrator characteristics.

The realization of power gyrators operating at constant switching frequency has been also studied in this chapter. The key element in the design is the equivalence between the equivalent control in sliding-mode and the nonlinear PWM zero-dynamics control reported in [20]. It has been concluded that all gyrator structures operating in sliding-mode can be automatically implemented in PWM operation by using this technique. According to this method the characteristic equation $\Delta_{PWM}(s)$ can be separated in two terms, i.e., $\Delta_{PWM}(s) = \Delta_{SLIDING}(s)(s + p)$ where $\Delta_{SLIDING}(s)$ is the system dynamics around the equilibrium point on the surface $S(x)$, and p defines the start-up dynamics of the gyrator.

Table I summarizes the expressions of the sliding surfaces, equivalent control in sliding-mode and the expression of the PWM nonlinear control law of all gyrators disclosed in this Chapter. It has also to be pointed out that the realization of gyrators operating in sliding-mode can be easily carried out by means of hysteretic comparator. However, the implementation of power gyrators operating at constant switching frequency requires a higher number of components what results in an increased wasted of the energy in the control loop. This design solution requires an analog divider, this eventually resulting in a more expensive realization.

An important fact that has to be pointed out is that all PWM G-gyrators require the same expression of the control law $\Gamma(x(t))$. In the case of PWM semigyrators, the expression continues to be the same by changing v_{C1} by V_g. Note also that the expression $\Gamma(x(t))$ for R-gyrators are dual of those corresponding to G-gyrator. Therefore, it can be concluded that the mathematical function $\Gamma(x(t))$ is the same for all gyrators irrespective of the type of power gyrator. This fact constitutes an important feature in terms of prototyping since the same electronic card can be used in all gyrator structures.

Table II shows the efficiency of all power gyrators that have been prototyped. It has to be pointed out that both G and R semigyrators have bigger efficiency than their corresponding G and R-gyrators. However, semigyrators have pulsating current and therefore they generate bigger EMI levels. This fact has been experimentally confirmed in the case of a buck converter-based G-semigyrator in which the generated noise at the input port reached the hysteretic comparator and made difficult the adjustment of this circuit.

On the other hand, the Cuk converter-based G-gyrator has a smaller efficiency than the rest of gyrators. This is partially, due to the high current stress of the switching devices that handle current peaks bigger that that of BIF and BOF gyrators. Also, the energy transfer is capacitive, this mechanism generally being less efficient than the inductive transference.

TABLE I. COMPARISON OF CONTROL LAWS FOR POWER GYRATORS

Converter	Sliding surface	Equivalent control $u_{eq}(x)$	PWM nonlinear control $\Gamma(x(t))$
BIF G	$S(x)= i_2 - gV_g$	$\frac{v_2}{v_{C1}}$	$\frac{v_2 + R_K\left(gV_g - i_2\right)}{v_{C1}}$
CUK G	$S(x)= i_2 - gV_g$	$\frac{v_2}{v_{C1}}$	$\frac{v_2 + R_K\left(gV_g - i_2\right)}{v_{C1}}$
BOF R	$S(x)= v_{C1} - rI_g$	$\frac{I_g - i_2}{I_g}$	$1 - \frac{i_2 + \frac{1}{R_K}\left(v_{C1} - rI_g\right)}{I_g}$
Semi-buck G	$S(x)= i - gV_g$	$\frac{v}{Vg}$	$\frac{v + R_K\left(gV_g - i\right)}{V_g}$
Semi-boost shunt R	$S(x)= v - rI_g$	$\frac{I_g - i_o}{I_g}$	$1 - \frac{i_O + \frac{1}{R_K}\left(v - rI_g\right)}{I_g}$
CUK G_{I1}	$S(x)= i_1 - gV_2$	$\frac{v_{C1} - V_g}{v_{C1}}$	$\frac{v_{C1} - V_g + R_K\left(gV_2 - i_1\right)}{v_{C1}}$
BOF G_{I1}	$S(x)= i_1 - gV_2$	$\frac{v_{C1} - V_g}{v_{C1}}$	$\frac{v_{C1} - V_g + R_K\left(gV_2 - i_1\right)}{v_{C1}}$

TABLE II. MEASURED EFFICIENCY OF POWER GYRATORS

Gyrator	Nominal Frequency	Measured Output Power	Measured Efficiency
BIF G	175 kHz	101 W	90 %
BIF G PWM	200 kHz	102 W	88 %
CUK G	175 kHz	65 W	80 %
BOF R	150 kHz	91 W	89 %
Semi G	150 kHz	103 W	91.1 %
R-semi.shunt	150 kHz	91 W	89.3 %
R-semi .boost	100 kHz	106 W	92 %
CUK G I_1 control	175 kHz	75 W	83 %

With regard to PWM power gyrators, it can be observed that a BIF converter-based G-gyrator is 2 % less efficient operating at constant switching frequency than working at variable switching frequency. This efficiency reduction is due to the fact that the PWM control loop consumes more energy than the hysteretic loop. Last but not least, it has been confirmed during the prototyping phase that one of the main advantages of the hysteretic-based control is its great implementation simplicity.

CHAPTER 3

3 REALIZATION OF ELECTRONIC FUNCTIONS IN ENERGY PROCESSING BY MEANS OF GYRATORS

3.1 Introduction

The aim of this chapter is to demonstrate that certain electronic functions in energy processing can be efficiently performed by means of power gyrators. Thus, it is intended to show that power gyrators are canonical elements in the construction of energy processing systems. The investigation is devoted to some properties directly derived from the G or R nature of power gyrators as, for example, current addition or current to voltage conversion. Another property studied in this chapter is the use of power gyrators for impedance matching, particularly for maximum power point tracking in photovoltaic systems. Voltage regulation in dc-to-dc conversion systems is a key function in power electronics. The realization of gyrator-based dc-to-dc switching regulators is not covered in this subject, but it will be extensively analyzed in Chapter 4.

3.2 Addition of currents

The addition of the output currents of several converters can be easily performed if the converters behave as current sources at their respective output ports. As demonstrated in Chapter 2, a G-gyrator has a current source nature at the output port. Hence, connecting in parallel the output ports of G-gyrators will result in a direct addition of currents. This fact will be a central element in the development of voltage regulators for high power applications as it will be shown in Chapter 4.

Fig. 3.1 illustrates the parallel connection of *n* power gyrators of type G. The scheme of Figure 3.1 can be implemented by means of either BIF converter-based G-gyrators or Cuk converter-based G-gyrators. Also, buck converter-based semigyrator can be used.

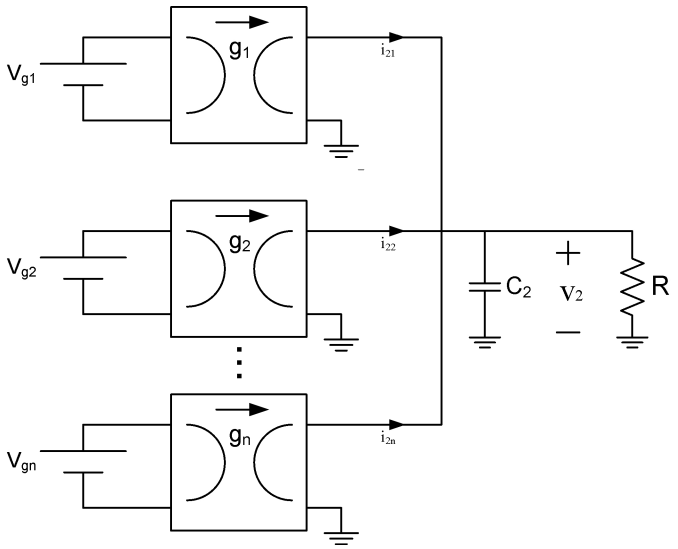

Fig. 3.1 Parallel connection of several gyrators of type G

The BIF converter-based G-gyrator has been chosen as a main building block of the electric architecture depicted in Fig. 3.1. It has been considered the best candidate for converter paralleling because it has bigger efficiency than the Cuk converter-based G gyrator and no voltage sign inversion at the output. The trade-off between lower EMI and higher efficiency has been solved for the first one. Thus, BIF structures has been chosen instead of buck structures because low levels of EMI have been considered a priority property in the electric architecture design.

On the other hand, the parallel connection of these gyrators will require the fulfillment of certain conditions ensuring the operation of each gyrator within its corresponding sliding region. As shown in 2.2.1.1.1 a BIF converter-based G-gyrator is characterized in steady-state by an equivalent control $u_{eq}(x^*) = \frac{V_2}{V_g}$ bounded by

$$0 < u_{eq}(x^*) < 1 \tag{3.1}$$

If *n* of gyrators connected in parallel are assumed to be equal, inequality (3.1) will become

$$0 < \frac{g_1 V_{g1} + \dots g_n V_{gn}}{V_{gi}} R < 1 \qquad \text{for gyrator i} \qquad \text{i= 1,… n} \tag{3.2}$$

Assuming $V_{g1} = V_{g2} = ,..., = V_{gn}$ and $g_1 = g_2 =,..., = g_n$, (3.2) becomes

$$g < \frac{1}{nR} \tag{3.3}$$

The practical implementation of three G-gyrators connected in parallel is shown in Fig. 3.2. The parameters of each gyrator are the following: $g = 0.5\ \Omega^{-1}$, $L_1 = 12\ \mu H$, $C_1 = 12\ \mu F$, $C_d = 100\ \mu F$, $R_d = 2.2\ \Omega$, $L_2 = 35\ \mu H$, $L_a = 22\ \mu H$, $R_a = 1.2\ \Omega$, and $C_2 = 6.6\ \mu F$. The nominal input voltage of each gyrator is $V_{g1} = 20\ V$, $V_{g2} = 18\ V$ and $V_{g3} = 16\ V$ and the output load is $R = 0.26\ \Omega$. Figure 3.3 illustrates the PSIM simulated response to a ± 4 V input voltage perturbation of step type superposed on the nominal input voltage of gyrator 1. It can be observed that output currents of gyrators 2 and 3 remain constant at 9 A and 8 A respectively. On the other hand, the output current of gyrator 1 reproduces proportionally the input voltage variations by changing from 10 A to 12 A and finally returning to 10 A.

Fig. 3.4 illustrates the corresponding experimental behavior of the 3 paralleled gyrators under the same test conditions simulated in Fig. 3.3. It can be observed that the measured waveforms verify the predictions obtained by simulation. The parallel connection delivers 189 W to the load and this power is distributed as follows: 70 W is supplied by gyrator 1, 63 W by gyrator 2 and 56 W by gyrator 3.

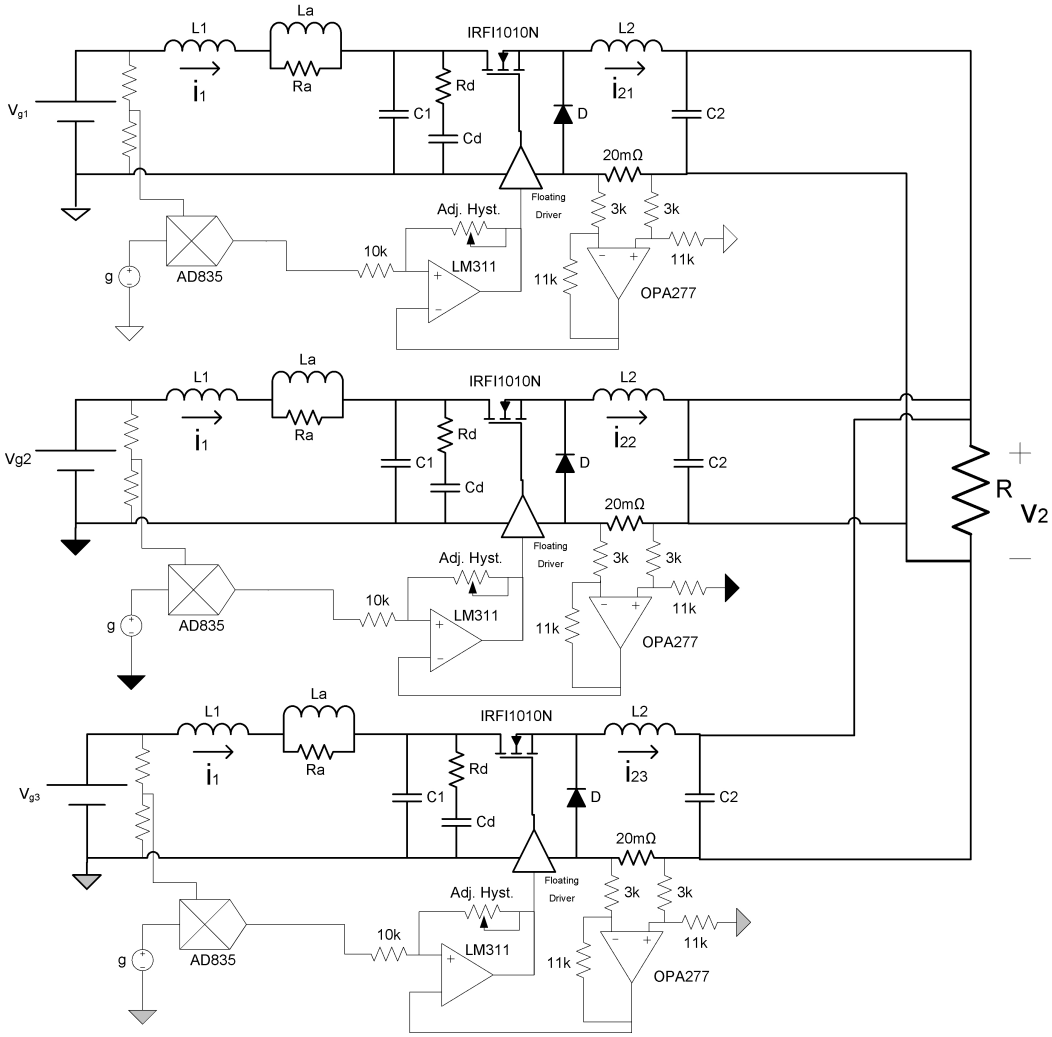

Fig. 3.2 Practical implementation of the parallel connection of three BIF converter-based G-gyrators.

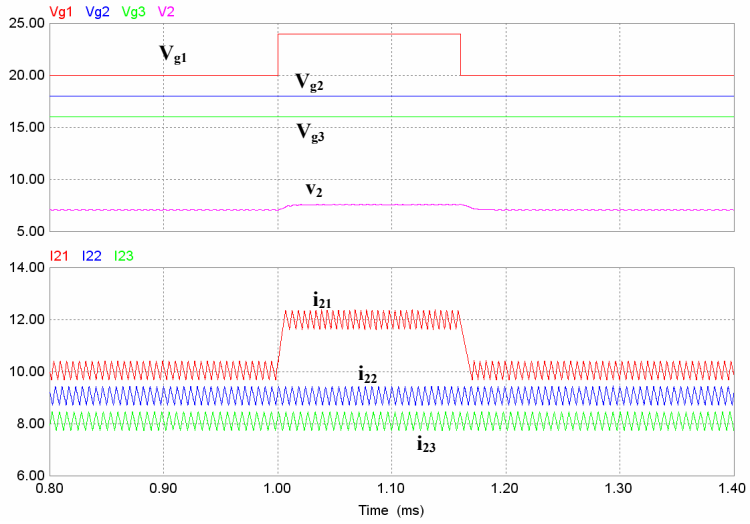

Fig. 3.3 Simulated response of the parallel connection of 3 G-gyrators. V_{g2} = 18 V, V_{g3} = 16 V and V_{g1} changes from 20 V to 24 V and returns to 20 V.

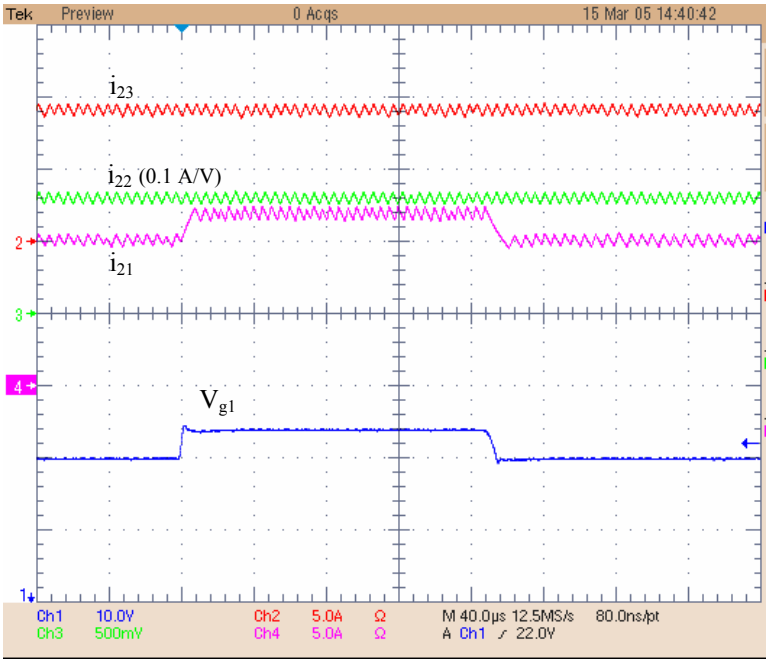

Fig. 3.4 Experimental behavior of 3 paralleled BIF converter-based G-gyrators to a pulsating input voltage in gyrator # 1.

3.2.1 G-gyrators paralleling with current distribution policy

The stress distribution among the different gyrators connected in parallel can be performed by means of different strategies for current distribution. Figure 3.5 shows a block diagram describing a current distribution scheme for *n* G-gyrators connected in parallel. Current I_{COM} establishes the reference current for each gyrator and it is obtained by weighting the output current values of each gyrator as follows

$$I_{COM} = \mu_1 I_{21} + \mu_2 I_{22} + \cdots + \mu_n I_{2N} \tag{3.4}$$

where I_{21}, I_{22}, ... , I_{2N} are the output currents of gyrator 1, gyrator 2, … , gyrator N respectively.

The current distribution can be carried out in two ways ,i.e., by means of a democratic current sharing or by means of a master-slave distribution.

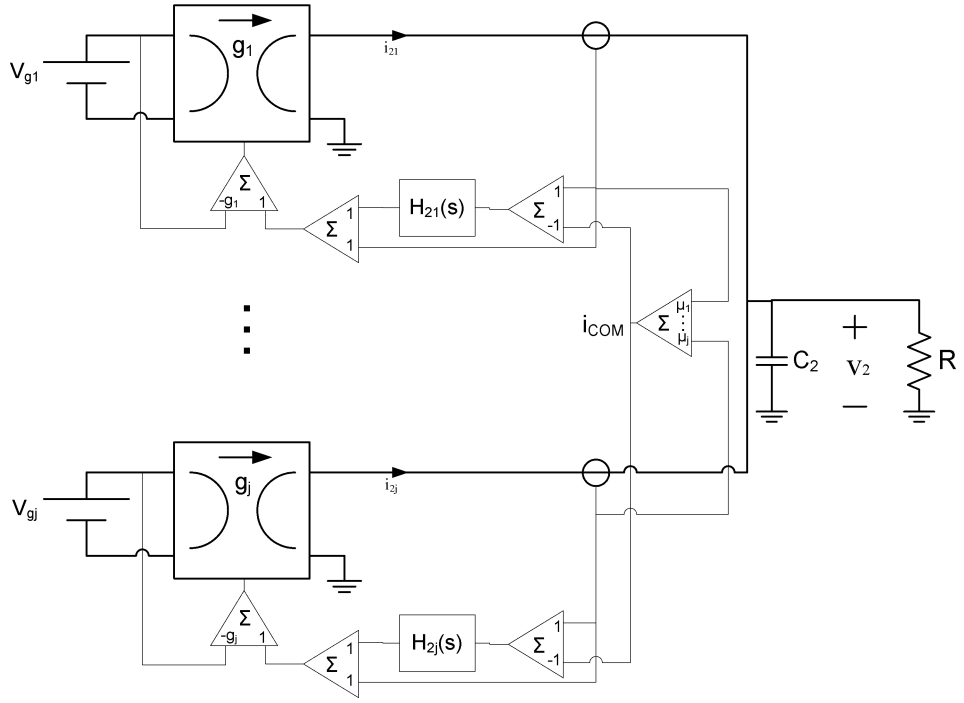

Fig. 3.5 Paralleled gyrators with current distribution policy

3.2.1.1 Democratic current sharing

The democratic current sharing implies $\mu_1 = \mu_2 = \ldots = \mu_N = \frac{1}{N}$, i.e., I_{COM} is the mean value of all output currents. Figure 3.6 illustrates a 3-gyrators parallel connection with democratic current sharing. The parameters of each gyrator are the following: $g = 0.5\ \Omega^{-1}$, $L_1 = 12\ \mu H$, $C_1 = 12\ \mu F$, $C_d = 100\ \mu F$, $R_d = 2.2\ \Omega$, $L_2 = 35\ \mu H$, $L_a = 22\ \mu H$, $R_a = 1.2\ \Omega$, and $C_2 = 6.6\ \mu F$. The nominal input voltage of each gyrator is $V_{g1} = 20\ V$, $V_{g2} = 18\ V$ and $V_{g3} = 16\ V$. The output load is $R = 0.26\ \Omega$. Note that each gyrator has an internal current loop to balance the current distribution. Details can be found later in Chapter 4.

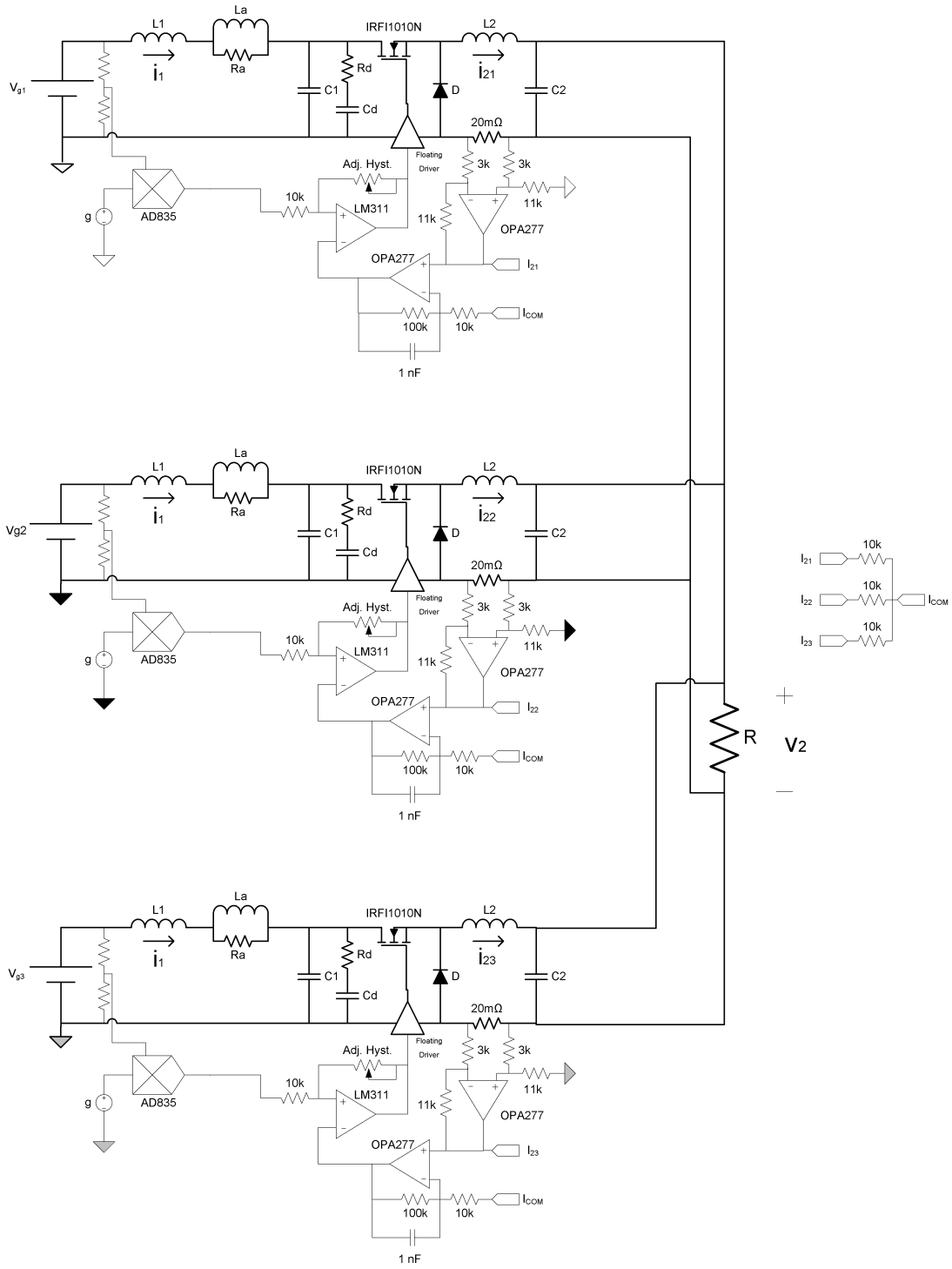

Fig. 3.6 Practical implementation of a 3-gyrators parallel connection with democratic current sharing

The experiments reported in 3.2.1 are now reproduced as shown in Figures 3.7 (simulation) and 3.8 (experimental results). Note that the ± 4 V step voltage perturbations at the input voltage of gyrator 1 are equally absorbed by the three output currents. The power delivered to the load is 189 W which is equally distributed among the 3 gyrators. In fact, gyrator 1 supplies 63.3 W, gyrator 2 delivers 62.6 W, and gyrator 3 provides 63.1 W.

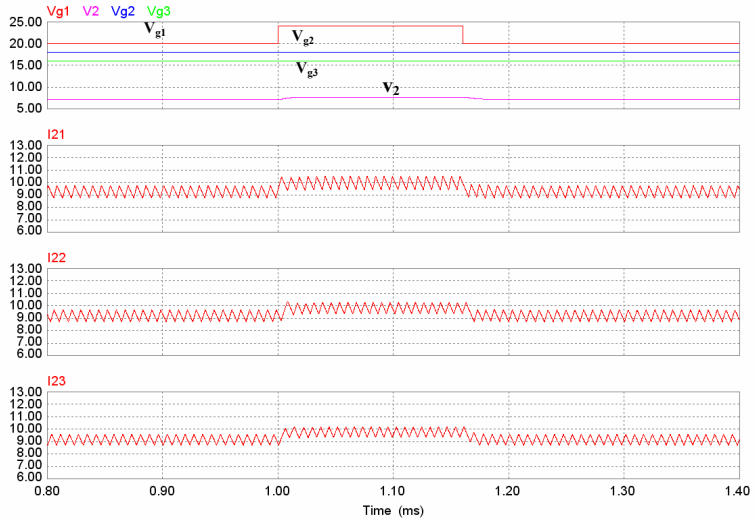

Fig. 3.7 Simulated response of a 3-gyrators parallel connection with democratic current sharing to a pulsating input voltage in gyrator 1.

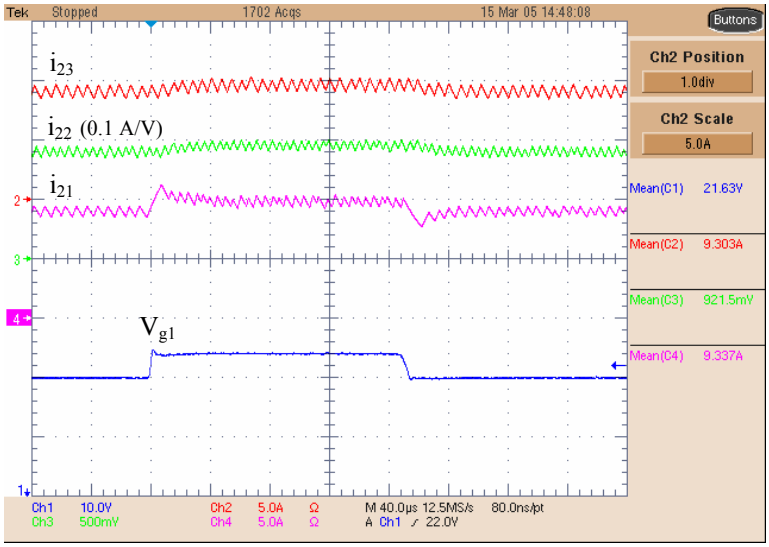

Fig. 3.8 Experimental response of a 3-gyrators parallel connection with democratic current sharing to a pulsating input voltage in gyrator 1

3.2.1.2 Master-slave current distribution

The master-slave current distribution is characterized by $\mu_1 = 1$ and $\mu_2 = \mu_3 = \ldots = \mu_N = 0$, this implying $I_{COM} = I_{21}$.

Figure 3.9 illustrates by means of simulation the effect of the master-slave current distribution in the parallel connection of Fig. 3.6 when the input voltage of gyrator 1 has the pulsating behavior previously described.

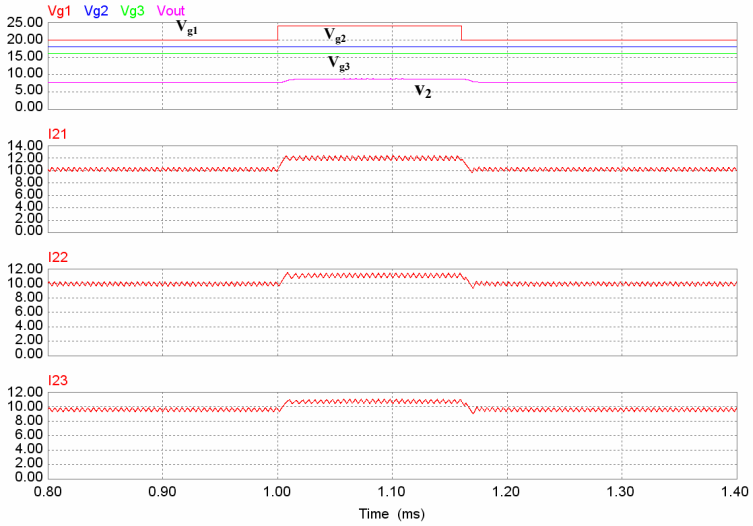

Fig. 3.9 Simulated response of a 3-gyrators parallel connection with master-slave current distribution to a pulsating input voltage in gyrator 1

3.3 Combining v-i and i-v conversion

In the context of transforming an energy source into its dual representation, we can think of a combined transformation performing the *v-i-v* conversion. Thus, a cascade connection of a G-gyrator and a R-gyrator would performed this conversion.

Figures 3.10 and 3.11 illustrate the symbolic representation for G-gyrators and R-gyrators respectively. Fig. 3.12 depicts the cascade connection of a power G-gyrator and a power R-gyrator.

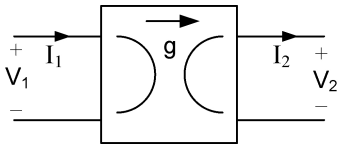

$$I_2 = gV_1$$
$$I_1 = gV_2$$

Fig. 3.10 Symbolic representation of a power G-gyrator

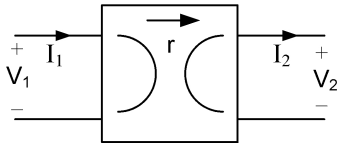

$$V_2 = rI_1$$
$$V_1 = rI_2$$

Fig. 3.11 Symbolic representation of a power R-gyrator

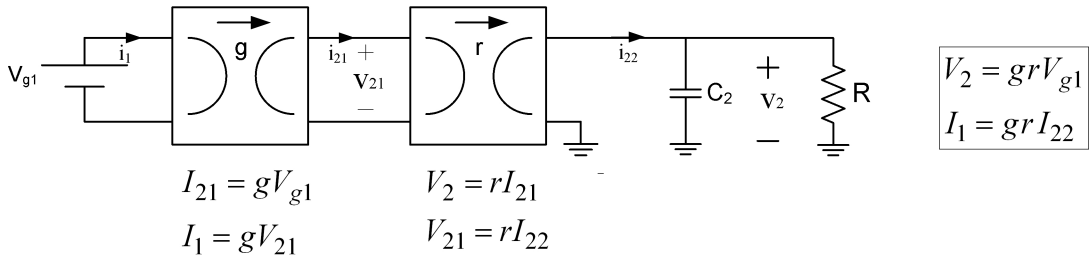

Fig. 3.12 Cascade connection of a power G-gyrator and a power R-gyrator

The practical implementation of the cascade connection is shown in Fig. 3.13. Note that inductance L_2 of the G-gyrator is used as the L_1 inductance of the BOF converter-based R-gyrator. It has to be pointed out that the circuit depicted in Fig. 3.13 has been used in the experimental test of the BOF converter-based R-gyrator described in Chapter 2.

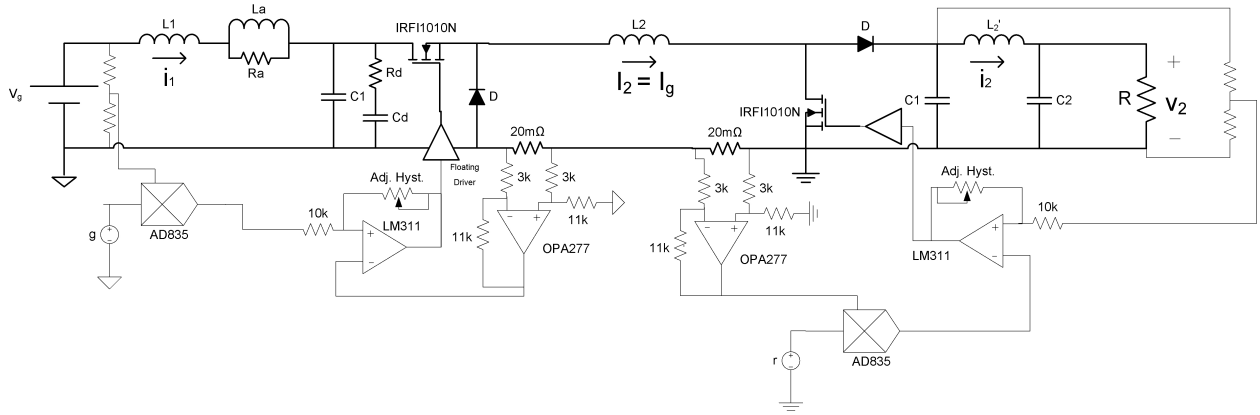

Fig. 3.13 Practical implementation of the cascade connection of a BIF G-gyrator and a BOF R-gyrator.

On the other hand, the v-i-v conversion could be performed by means of the circuit scheme shown in Fig. 3.14. Note that the v-i conversion is carried out by means of the parallel connection of *n* G-gyrators whose output is the input of a power R-gyrator.

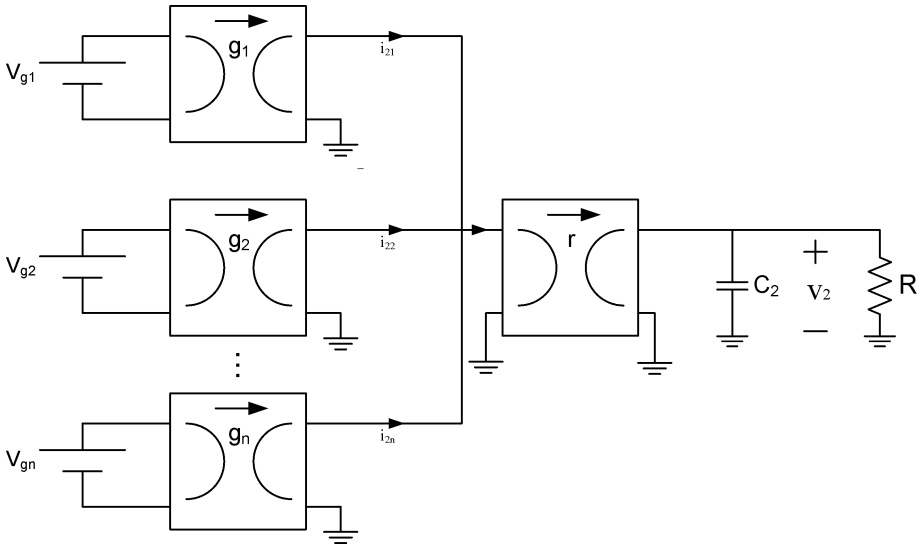

Fig. 3.14 Cascade connection of n-paralleled power G-gyrators and a power R-gyrator

Figure 3.15 shows the practical realization of the circuit scheme depicted in Fig. 3.14 for the case of 3 paralleled G-gyrators. The G-gyrators are based on the BIF converter while the R-gyrator is based on the BOF converter. The parameters of each G-gyrator are $g = 0.5\ \Omega^{-1}$, $L_1 = 12\ \mu H$, $C_1 = 12\ \mu F$, $C_d = 100\ \mu F$, $R_d = 2.2\ \Omega$, $L_2 = 35\ \mu H$, $L_a = 22\ \mu H$, $R_a = 1.2\ \Omega$, and $C_2 = 6.6\ \mu F$. The parameters of the R-gyrator are $R = 5\ \Omega$, r= 1.1 Ω , C_1 = 20 μF, L_2 = 12 μH, C_2 = 2 μF. The input voltage of each G-gyrator is $V_{g1} = 14\ V$, $V_{g2} = 12\ V$ and $V_{g3} = 12\ V$.

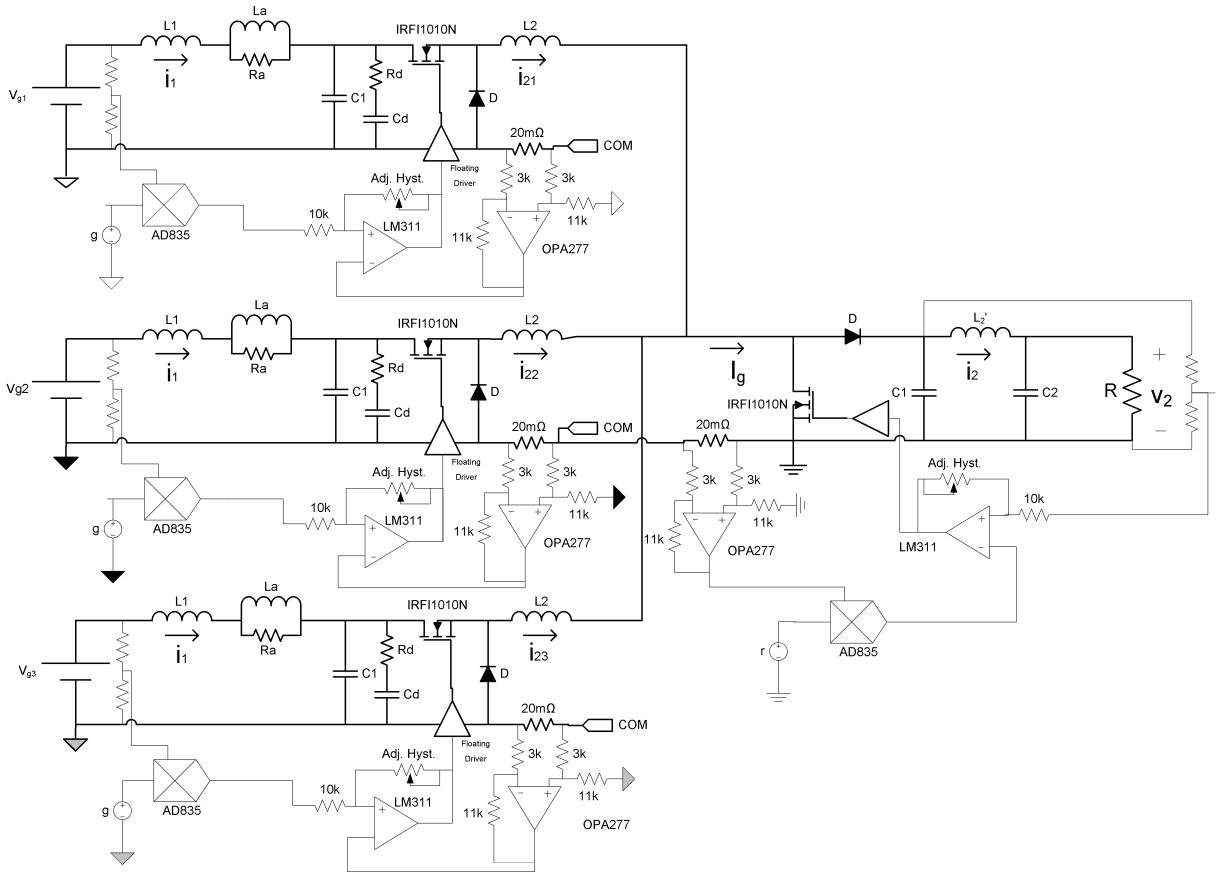

Fig. 3.15 Practical implementation of a cascade connection of 3 paralleled power G-gyrators and a power R-gyrator

Figure 3.16 shows the system response to a 50 % step change in the load resistance. Note that the output voltage remains constant and the load perturbation is absorbed by output current of the R-gyrator.

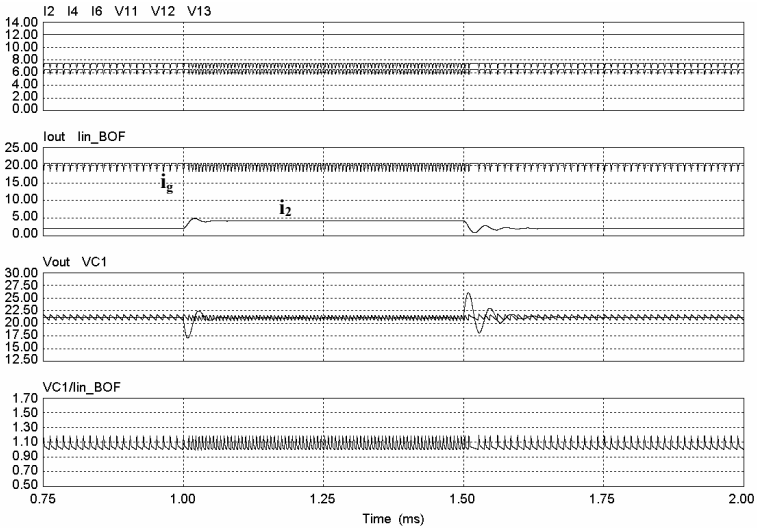

Fig. 3.16 *Simulated response of the circuit of Fig. 3.15 to load variations of step type*

The corresponding experimental results are depicted in Fig. 3.17 and they are in good agreement with the simulation shown in Fig. 3.16. Note that the output voltage is 1.035 times the value of the sum of G-gyrator output currents. This value is practically the theoretical one, which is 1.1 times the value of this sum.

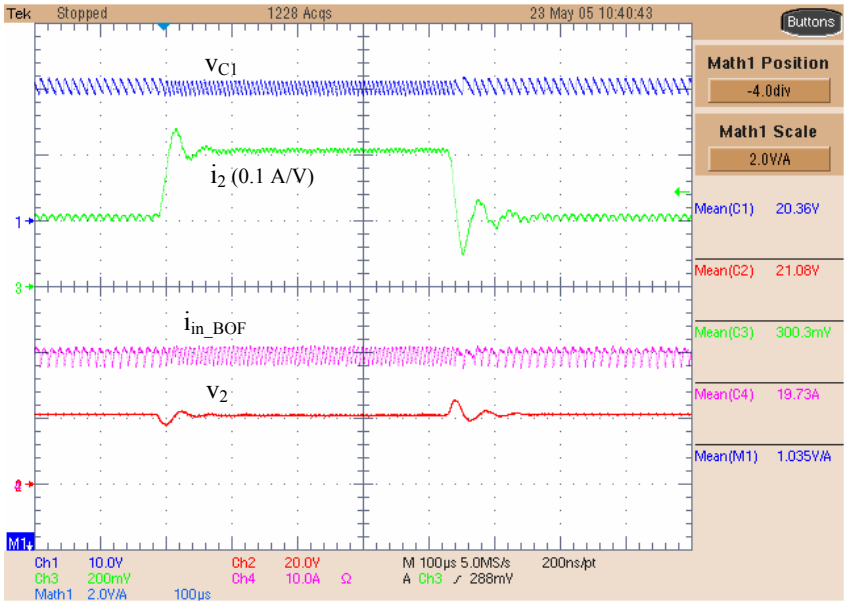

Fig. 3.17 *Experimental response of the circuit of Fig. 3.15 to load variations of step type*

3.4 Impedance matching

Impedance matching in power electronics basically means solving the problem of maximum power transfer between a dc generator and a dc load. In particular, the maximum power transfer from a photovoltaic panel to a dc load is an important technological problem in many practical cases dealing with the optimization of a PV conversion chain [33].

Although there are many works devoted to the problem of the maximum power point tracking (MPPT) in a PV array, only few of them deal with the nature of the power interface while most of them focus on different types of tracking algorithms. The problem of finding the most appropriate power interface is discussed next. The main antecedents in the study of matching power interfaces can be found in the works of Singer and Braunstein on the coupling of a PV array and a dc load by means of a dc transformer with variable transformer ratio [24]-[25].

We will analyze first the matching problem using the notion of a dc transformer and subsequently we will demonstrate that such problem can be solved by using a power gyrator.

3.4.1 Impedance matching by means of a dc transformer

A dc-to-dc switching converter can be modeled according to Middlebrook's paradigm as an ideal dc function of the duty cycle. The PV generator-converter-dc load connection shown in Fig.1 where both generator and load have been modeled by a first quadrant *v-i* characteristics.

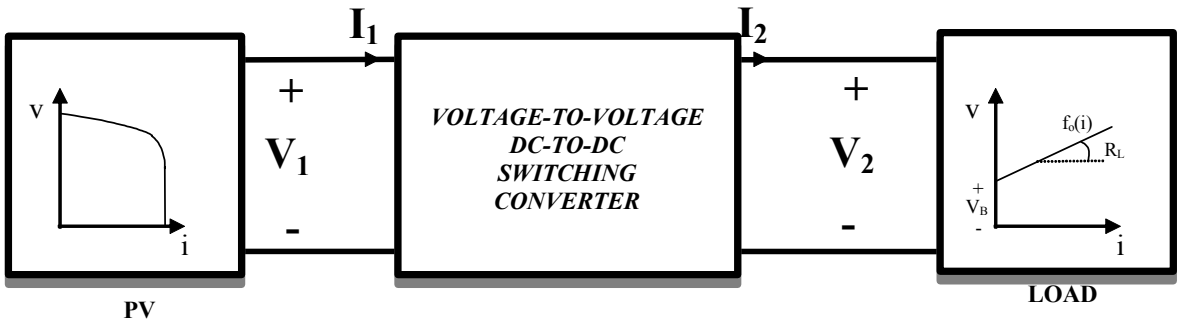

Fig. 3.18 Matching a PV generator to a dc load using a voltage-to-voltage dc-to-dc switching converter

The behavior of the converter in steady-state can be described by means of the following equations

$$V_2 = n(D)V_1$$
$$I_2 = \frac{1}{n(D)} I_1 \qquad (3.5)$$

which define a dc ideal transformer.

The dc load can be modeled by means of the following function $v = f(i)$

$$v = f_o(i) = V_B + R_L i \tag{3.6}$$

with $V_B > 0$ and $R_L > 0$

which corresponds to the Thevenin equivalent of the usual dc loads supplied by a PV generator. Namely, storage batteries, permanent magnet dc motor, shunt dc motor, electrolysis pool etc

From (3.5) and (3.6) the following function $v_1 = f_{in}(i_1)$ is derived

$$v_1 = f_{in}(i_1) = \frac{V_2}{n(D)} = \frac{V_B}{n(D)} + \frac{R_L I_2}{n(D)} = \frac{V_B}{n(D)} + \frac{R_L}{n^2(D)} I_1 \tag{3.7}$$

Fig. 3.19 shows the intersection of characteristics f_o and f_{in} with the PV curve under different hypotheses. In this case, the direct connection of the load to the panel would correspond to the operating point A, which is located at the left side of the maximum point M. It can be deduced from (3.7) that the intersection point will be placed at the right of M if $n(D) > 1$. On the other hand, if we assume that the intersection at point B corresponds to a certain value D_1 of the duty cycle, then intersection at C will correspond to a value $D_2 > D_1$ since $n(D)$ is an increasing monotonous function of the duty cycle D [22].

The objective of the converter is to achieve a f_{inop} characteristic so that it intersects with PV curve at the optimal operating point M.

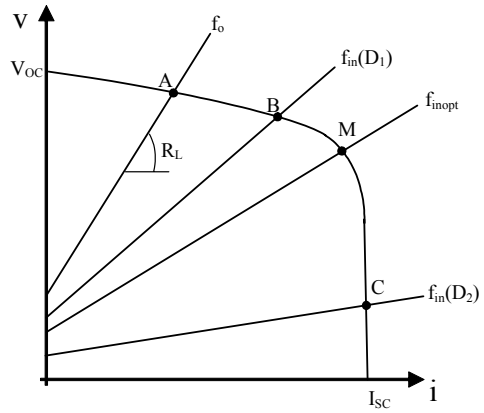

Fig. 3.19 PV Array operating points (n(D) >1, $D_2 > D_1$)

Similarly, figure 3.20 illustrates the case of an operating point corresponding to a direct connection (point A) which is located at the right of M, and it also shows the possibility of matching with $n(D) < 1$. In this case, $D_2 < D_1$.

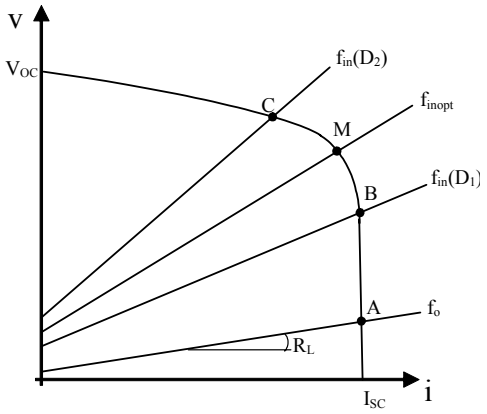

Fig. 3.20 PV array operating points (n(D) < 1, $D_2 < D_1$)

Now, we will analyze the influence of the duty cycle variations in equation (3.7) in order to study the trajectories that allow the displacement of the operating point along the v-i characteristic curve of the PV array.

Therefore

$$\frac{dV_1}{dD} = -\frac{V_B}{n^2(D)}\frac{dn(D)}{dD} - \frac{2R_L}{n^3(D)}\frac{d(n(D))}{dD}I_1 = -\left(\frac{V_B}{n^2(D)} + \frac{2R_L I_1}{n^3(D)}\right)\frac{d(n(D))}{dD} < 0 \qquad (3.8)$$

since $\frac{d(n(D))}{dD} > 0$ in any converter [22] and we assume n(D) > 0.

On the other hand, we can write

$$\Delta V_1 = \frac{dV_1}{dD}\Delta D \qquad (3.9)$$

Therefore, we can conclude that increasing the duty cycle will produce a trajectory to the right along the *v-i* curve (ΔV_1 negative), while decreasing *D* will result in a trajectory to the left along the *v-i* curve irrespective of the step-up or step-down nature of the converter.

3.4.2 Impedance matching by means of a dc gyrator

If the voltage to voltage dc-to-dc switching converter of Fig. 3.18 is substituted by a voltage to current dc-to-dc switching converter, i.e., a G-power gyrator, the steady-state equations at both input and output ports of the converter will be given by

$$\begin{aligned} I_1 &= gV_2 \\ I_2 &= gV_1 \end{aligned} \qquad (3.10)$$

From (3.6) and (3.10), we conclude that the input characteristics $v_{in} = f_{in}(i_1)$ will be expressed as

$$V_1 = \frac{I_2}{g} = \frac{V_2}{gR_L} - \frac{V_B}{gR_L} = \frac{I_1}{g^2 R_L} - \frac{V_B}{gR_L} \tag{3.11}$$

Figs. 3.21 and 3.22 show the intersection of characteristics f_o and f_{in} with PV curve in similar situations as those illustrated in figs. 3.19 and 3.20 respectively. Fig. 3.21 describes the direct connection of the load to the PV array resulting in an operating point A located at the left of the maximum power point. It can be derived from (3.11) that the intersection point B can be placed at the right side of M by an appropriate choice of g. On the other hand, if the slope of $f_o(i_2)$ is R_L, the slope of $f_{in}(i_1)$ will be $\frac{1}{g^2 R_L}$.

In chapter 2, expression (2.23), it has been shown that the existence of sliding motions requires the fulfillment of the following inequality

$$0 < gR_L < 1 \tag{3.12}$$

Therefore

$$R_L < \frac{1}{g} < \frac{1}{g^2 R_L} \tag{3.13}$$

which shows that the slope of $f_{in}(i_1)$ is smaller than that of $f_o(i_2)$

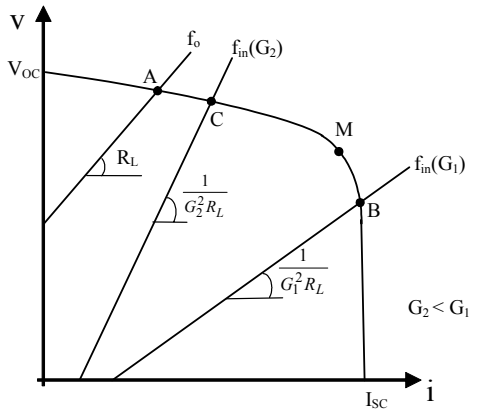

Fig. 3.21 PV array operating points. Impedance matching by means of a G-gyrator ($f_o(i_2)$ intersects at the left side of M)

If we assume that the intersection at point B corresponds to a certain value G_1 of the gyrator conductance, then intersection at C will correspond to a value $G_2 < G_1$ as derived from (3.11).

Fig. 3.22, in turn, illustrates the case of a direct connection at point A', which is located at the right side of point M. By an appropriate selection of the gyrator conductance ($G = G_2$) the operating point can be placed at the left side of M (point B'). Increasing the conductance value to G_1 ($G_1 > G_2$) will establish the operating point at point C', which is located at the left side of M.

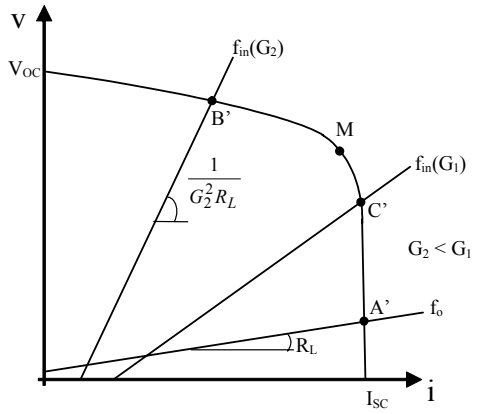

Fig. 3.22 PV array operating points. Impedance matching by means of a G-gyrator. ($f_o(i_2)$ intersects at the right side of M)

Now, we will study the influence of conductance g variations in equation (3.11) in order to study the trajectories or the operating point along the *i-v* curve. Hence,

$$\frac{dV_1}{dg} = -\frac{2I_1}{g^3 R_L} + \frac{V_B}{g^2 R_L} = \frac{1}{g}\left(\frac{-2I_1}{g^2 R_L} + \frac{V_B}{gR_L}\right) = \frac{1}{g}\left(\frac{-2I_1}{g^2 R_L} + \frac{I_1}{g^2 R_L} - V_1\right) = \frac{-1}{g}\left(V_1 + \frac{I_1}{g^2 R_L}\right) < 0 \tag{3.14}$$

Also,

$$\Delta V_1 = \frac{dV_1}{dg}\Delta g \tag{3.15}$$

Therefore, we can conclude that increasing the gyrator conductance will result in a trajectory towards the right (ΔV_1 negative), while decreasing g will result in a trajectory to the left along the *v-i* curve.

3.4.2.1 G-gyrator-based maximum power point tracking of a PV array

It has been recently demonstrated that an extremum seeking algorithm was stable in the sense of Lyapunov and that it could applied to the maximum power point tracking of a PV generator by using a voltage to voltage dc-to-dc switching converter in PWM operation.

The main characteristics of the extremum seeking algorithm are reviewed in Appendix C. The application of such algorithm to a G-gyrator-based maximum power point tracking is analyzed next.

We will demonstrate that the extremum seeking algorithm will force the PV system to approach to the maximum power point by increasing or decreasing the voltage at the panel terminals with a constant value of the time-derivative.

Figure 3.23 shows the block diagram of a G-gyrator-based maximum power point tracking. Note that variable x in Appendix C becomes the panel voltage v_s while variable y represents now

the panel power p_s. A battery constitutes the gyrator load. The variation of v_s with constant time-derivative es achieved by imposing such behavior to the gyrator conductance G.

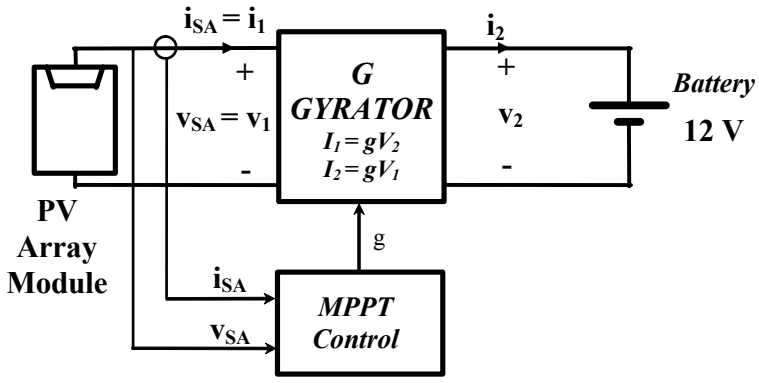

Fig. 3.23 Block diagram of a MPPT of a PV array based on a power gyrator of type G.

The variation of the gyrator conductance changes the PV panel operating point as depicted in Fig. 3.24. In such figure the operating points P_1 and P_2 correspond respectively to conductance G_1 and G_2 with $G_2 > G_1$, and we have assumed that the battery voltage v_B is less than v_{OC} of the PV generator.

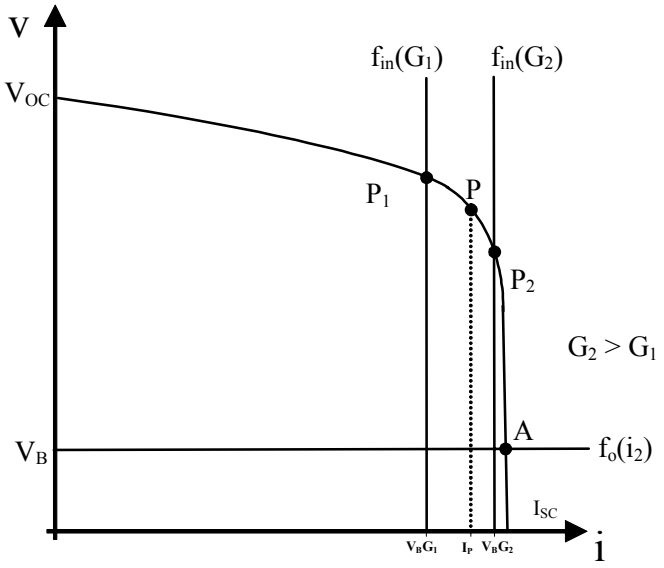

Fig. 3.24 PV array operating points corresponding to the system depicted in Fig. 3.23

Assume now that the transition from P_1 to a generic point P is carried out by increasing the gyrator conductance as follows

$$G_P(t) = G_1 + kt \tag{3.16}$$

Therefore, the expression of $I_P(t)$ will be given by

$$I_P(t) = V_B G_P(t) = V_B G_1 + V_B kt = I_{P1} + V_B kt \tag{3.17}$$

which predicts a linear increasing with time of the current at the solar array terminals.

Similarly, a decrease in the gyrator conductance would result in a decrease of $I_P(t)$ given by

$$I_P(t) = I_{P1} - V_B kt \tag{3.18}$$

On the other hand, the power P supplied by the PV generator can be expressed as a function of the panel current I_1 as follows

$$P = V_1(I_1)I_1(t) = g(I_1) \tag{3.19}$$

At the maximum power point M, we can write

$$\left.\frac{dP}{dI_1}\right|_{I_1 = I_M} = 0 \tag{3.20}$$

and

$$\left.\frac{d^2P}{dI_1^2}\right|_{I_1 = I_M} < 0 \tag{3.21}$$

In terms of gyrator conductance, we can express

$$\frac{dP}{dG} = \frac{dP}{dI_1}\frac{dI_1}{dG} = \frac{dP}{dI_1}v_B \tag{3.22}$$

and

$$\frac{d^2P}{dG^2} = \frac{d^2P}{d^2{I_1}^2}\frac{dI_1}{dG}v_B = \frac{d^2P}{d^2{I_1}^2}{v_B}^2 \tag{3.23}$$

Taking into account (3.20) and (3.21), expressions (3.22) and (3.23) become

$$\frac{dP}{dG} = 0 \quad \text{at the maximum power point} \tag{3.24}$$

$$\frac{d^2P}{dG^2} < 0 \quad \text{at the maximum power point} \tag{3.25}$$

We can conclude that there is an optimum value of G that results in the maximum power transference.

The block diagram depicted in Figure 3.23 has been implemented as shown in figure 3.25 where the power gyrator and its control circuit are depicted in detail.

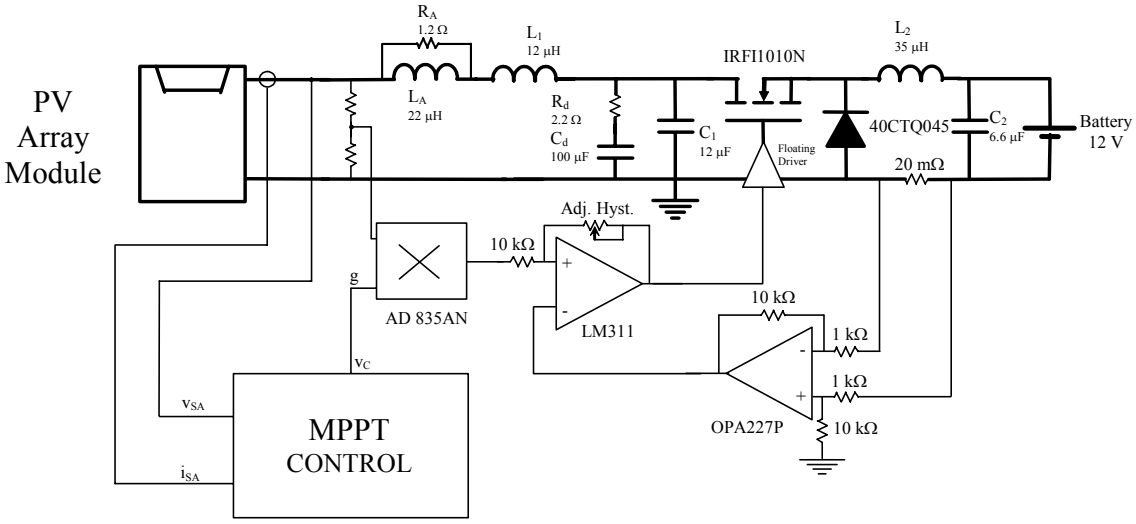

Fig. 3.25 Practical implementation of a BIF converter-based G-gyrator performing the MPPT of a PV array

The PV panel is a solar array of monocrystalline cells with an open circuit voltage of 22.1 V and a nominal voltage value at the maximum power point of 18 V. Since the load is a 12 V acid-lead battery, the dc-to-dc conversion must be performed by a BIF structure. The BIF parameters satisfy the stability conditions (2.28)-(2.30) and are given by $V_g = 20\ V$, $V_{BAT} = 12\ V$, $g = 0.5\ \Omega^{-1}$, $L_1 = 12\ \mu H$, $C_1 = 12\ \mu F$, $C_d = 100\ \mu F$, $R_d = 2.2\ \Omega$, $L_2 = 35\ \mu H$, $C_2 = 6.6\ \mu F$, $L_a = 22\ \mu H$ and $R_a = 1.2\ \Omega$. The circuit performing the MPPT control is illustrated in Fig. 3.26.

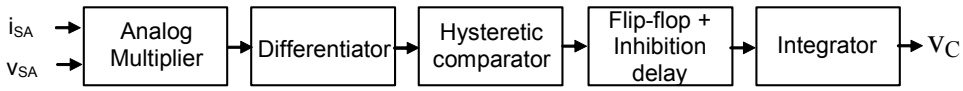

Fig. 3.26 Realization of the MPPT controller

The MPPT controller consists of six blocks, namely, analog multiplier, differentiator, hysteretic comparator, bistable with inhibition delay, integrator and pulse width modulator. The analog multiplication is performed by the *IC AD835* whose two inputs are proportional to current and voltage of the PV array respectively. The output of the analog multiplier provides a signal proportional to the PV panel power which is then differentiated by a linear circuit of two operational amplifiers implementing the transfer function

$$D_L(s) = k' \frac{s}{\left(\frac{T_d}{2\pi} s + 1\right)^2} \tag{3.26}$$

where T_d has tuned to $\frac{T_{MPPT}}{8}$, T_{MPPT} being the oscillation period around the maximum power point that characterizes the MPPT behavior.

It can be observed that $D_L(s)$ is a pure differentiator for signals with frequency contents below $2\pi / T_d$. Constant T_d must be smaller than the smallest time-constant of the converter, which, in turn, must be much bigger than the switching period.

The output signal of the linear differentiator is then processed by a hysteretic comparator which eliminates the high frequency harmonics. The comparator output provides a digital signal which indicates whether the power time-derivative is positive or negative. The digital signal is introduced into a flip-flop with inhibition delay which establishes, after a fixed time interval of 4.5 ms, if the direction of maximum searching has to be maintained or should be changed. The waiting interval ensures that the converter is operating in steady-state when the decision on the change or maintenance of the sign of the control law is made. The output signal of the flip-flop is multiplied by a constant K' and the result is integrated in order to obtain the ramp signal required by the reference input of the power gyrator. The voltage excursion Δv_s around the maximum power point is given by $\Delta v_s \approx K' \frac{T_{MPPT}}{2}$ and it will eventually establish the MPPT efficiency. [27].

3.4.2.1.1 Experimental results

It will be shown in this section the experimental behavior of I_s, V_s, P_s of the PV generator and also of conductance g with the extremum-seeking control algorithm under different operating conditions. The experimental prototype corresponds to the circuit configuration of figure 8 using a PV panel of 85 W of nominal power and a 12 V battery as a load.

A) Steady-state measurements.

Figure 3.27 shows in detail the steady-state behavior of the BIF converter-based G-gyrator performing a MPPT function. It can be observed that the extremum seeking control algorithm imposes a triangular shape waveform to the gyrator conductance g. The positive slope interval of the triangular signal corresponds to the PV operating point trajectory going from left to right towards the maximum power point. The negative slope interval, in turn, corresponds to the right to left movement. Thus, the maximum power point is found twice in each period of the g triangular waveform. Note that the signal corresponding to V_{PV} is 180° out of phase with respect to signal g and current I_{PV} as predicted in the analysis of 3.3.2. The MPPT efficiency, i.e., the quotient between the power absorbed from the solar array and the maximum available power is 99.17 % for a delivered power of 38.53 W.

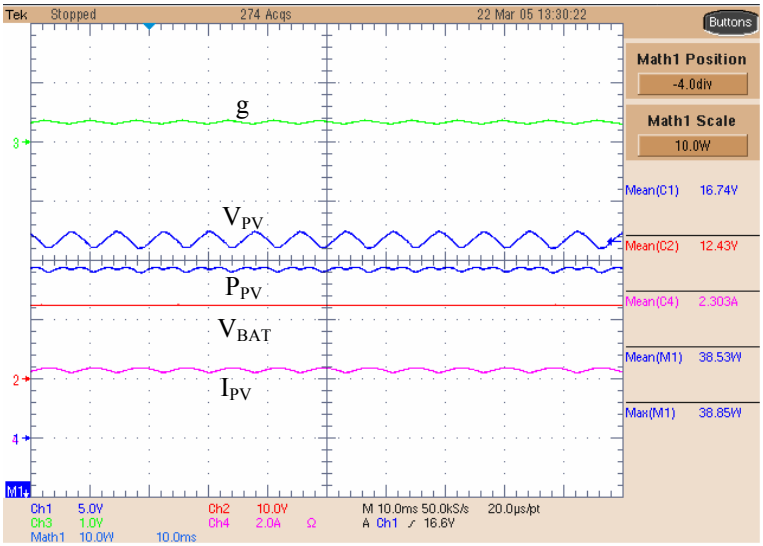

Fig. 3.27 *Steady-state waveforms of a BIF converter-based G-gyrator with MPPT function charging a 12 V battery*

B) Array paralleling

Figure 3.28a shows the PV system response after the connection of an additional panel in parallel with the PV generator. As it can be expected, the current increases while the voltage remains practically unchanged except in the transient-state connection. Since the voltage operating point has not changed, the maximum power point is almost instantaneously reached. A similar situation is observed in Fig. 3.28b in which the panel previously added is removed.

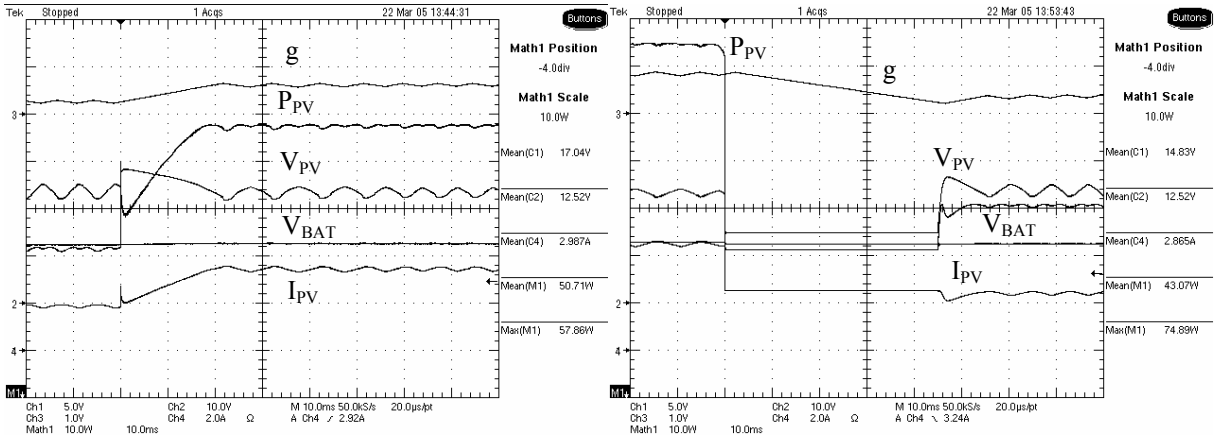

a) connection *b) disconnection*

Fig. 3.28 *Response to a parallel connection of an additional panel.*

C) DC voltage source in series with the PV generator

Fig. 3.29a shows the behavior of the panel variables after the insertion of a 5 V DC source in series with the PV generator. In this case, the current operating point has not changed and,

therefore, the MPPT algorithm adapts very fast the system operation to the new situation. Similarly, as illustrated in Fig. 3.29b, after disconnecting the DC voltage source, a linear decrease of the array voltage occurs and the new operating point is also reached very quickly.

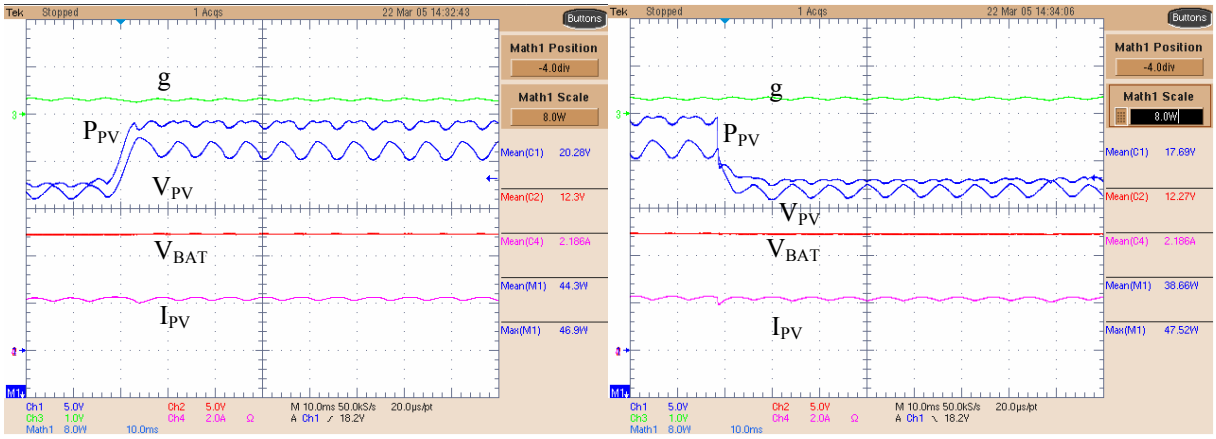

a) connection *b) disconnection*

Fig. 3.29 Response to a series connection of an additional 5 V DC source.

3.4.2.2 MPPT by means of gyrators of type G with controlled input current

A Cuk converter-based G-gyrator with controlled input current is a versatile structure that can be indistinctly used for output voltages higher or smaller than the input voltage. This is due to the fact that the equivalent control $u_{eq}(x)$ found in (2.50) is bounded as follows.

$$0 < \frac{V_2}{V_2 + v_1} < 1 \tag{3.27}$$

This condition is satisfied indistinctly for $V_2 > V_1$ and for $V_1 < V_2$.

Figure 3.30 shows the circuit scheme of a Cuk converter-based G-gyrator with controlled input current performing the MPPT of a PV array. Note that the output of the analog multiplier AD835 is the product of g times a negative signal proportional to $-V_2$. The gyrator parameters are $L_1 = 75\ \mu H$, $C_1 = 10\ \mu F$, $L_2 = 75\ \mu H$, and $V_2 = 12\ V$ (24 V).

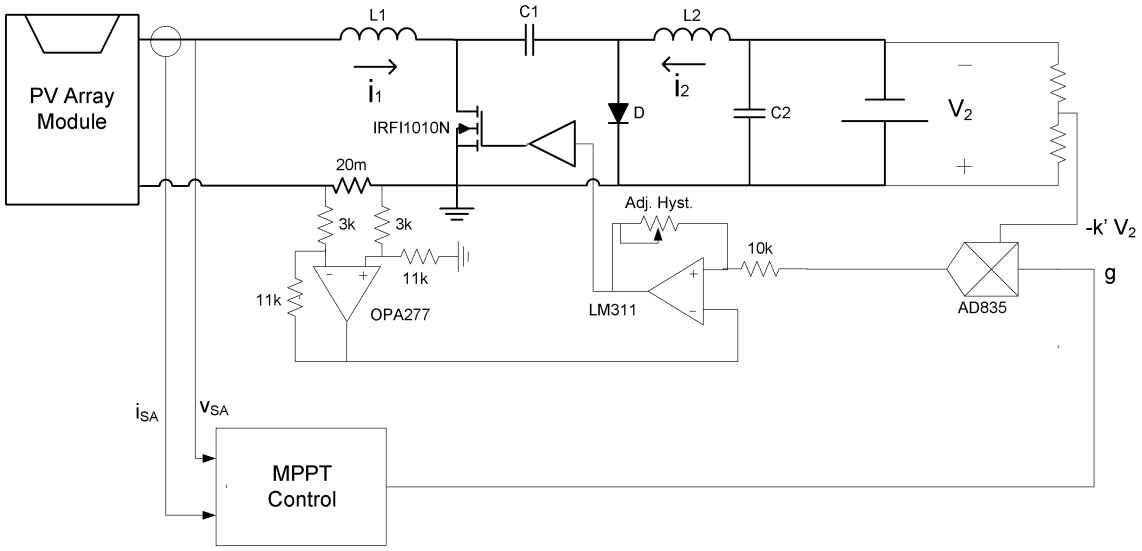

Fig. 3.30 *Cuk converter-based G-gyrator with controlled input current with MPPT function*

Figures 3.31 and 3.32 show the charge of a 12 V battery and a 24 V battery respectively by means of the power gyrator with MPPT function. Note that the search of the maximum point is performed by controlling *g* (depicted in channel 3) which takes negative values in this case. The MPPT efficiency is of 99 % when the gyrator delivers 57.47 W to a 12 V battery and 98.6 % efficiency when it supplies 57.4 W to a 24 V battery.

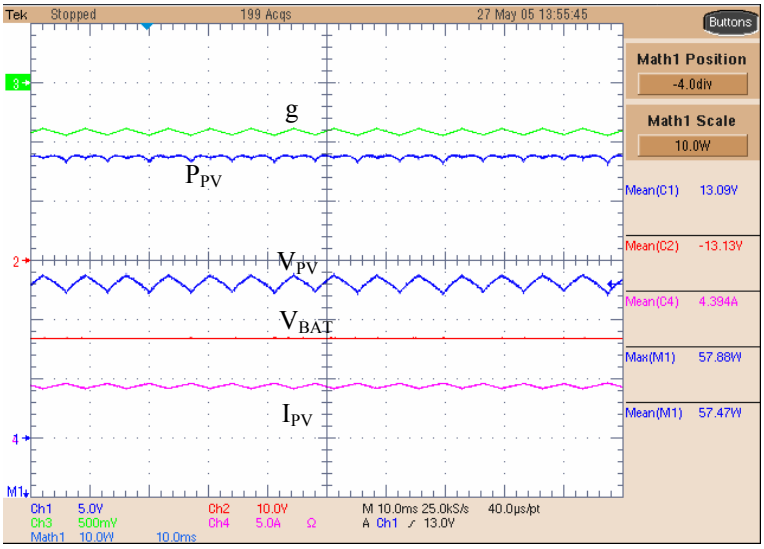

Fig. 3.31 *Steady-state waveforms of a Cuk converter-based G-gyrator with controlled input current supplying 12 V battery.*

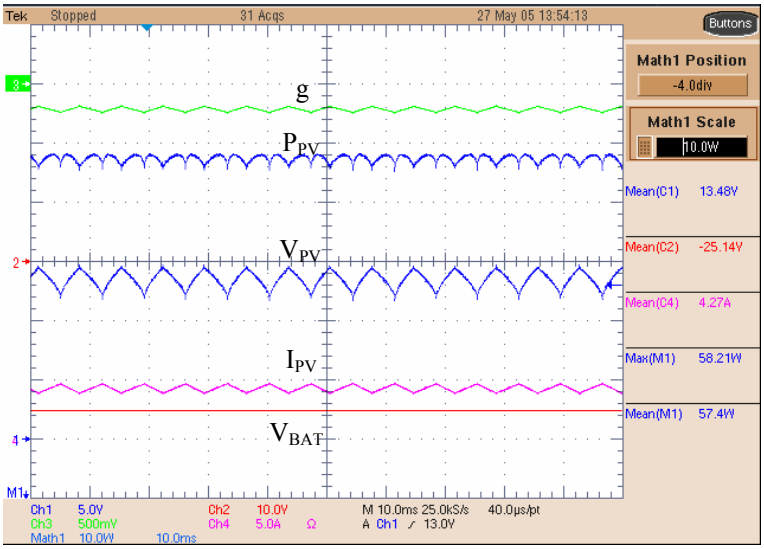

Fig. 3.32 *Steady-state waveforms of a Cuk converter-based G-gyrator with controlled input current supplying 24 V battery.*

3.4.2.3 MPPT by means of gyrators of type R

R-gyrators can be also used to perform the MPPT function in a PV array. Figure 3.33 shows the block diagram of a MPPT system based on a R-gyrator.

The equations (2.3)-(2.4) defining a power R-gyrator can be written also as follows.

$$I_1 = \frac{V_2}{r} \tag{3.28}$$

$$I_2 = \frac{V_1}{r} \tag{3.29}$$

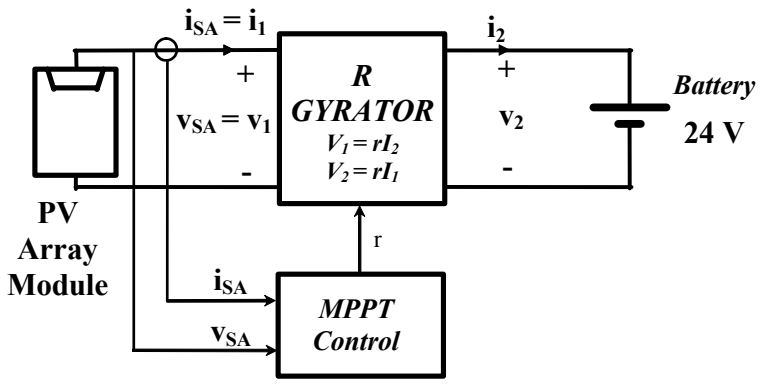

Fig. 3.33 *Block diagram of a PV array MPPT system based on R-gyrator*

Note that substituting r^{-1} by g in (3.28)-(3.29) allows the same assumptions of 3.3.2.1 for MPPT realization. Therefore, we can find a value of r in a power R-gyrator that results in the maximum power point operation as depicted in Fig. 3.34

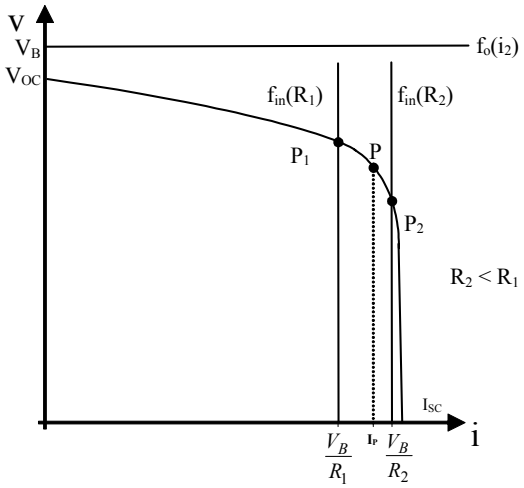

Fig. 3.34 PV array operating points corresponding to the system depicted in Fig. 16

The BOF converter-based R-gyrator shown in Fig. 2.4.3 has been modified for the connection to a PV array. With this purpose, the current source I_g has been substituted by an inductance in series with the PV generator. The practical implementation is illustrated in Fig. 3.35 for the following set of parameters: $L_1 = 55\ \mu H$, $C_1 = 20\ \mu F$, $L_2 = 12\ \mu H$, $C_2 = 2\ \mu F$ and $V_2 = 24\ V$.

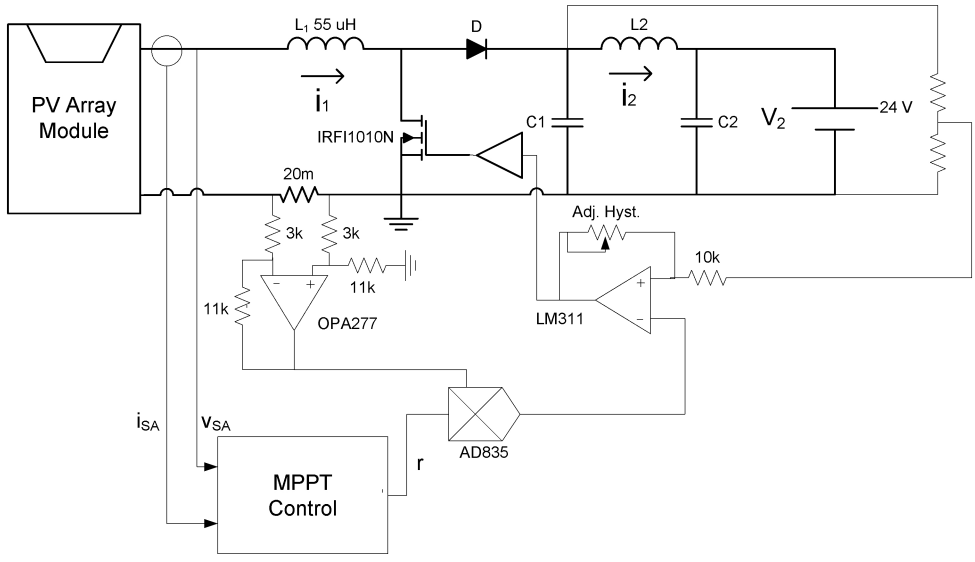

Fig. 3.35 Practical implementation of a BOF converter-based R-gyrator with MPPT function

A) Steady-state measurements

Fig. 3.36 shows the steady-state behavior of the BOF converter-based R-gyrator of Fig. 3.35 performing a MPPT function when charging a 24 V battery. It can be observed that the search of the maximum power point is performed by controlling variable *r* depicted in channel 3. Note that the MPPT efficiency is of 99 % for 45,43 W of supplied power to the battery.

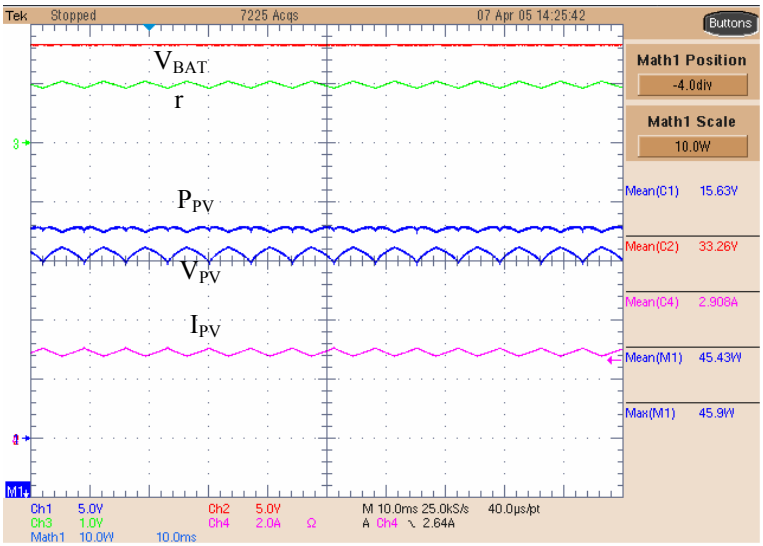

Fig. 3.36 *Steady-state waveforms of the power gyrator of Fig. 18 charging a 24 V battery with MPPT function.*

B) Array paralleling

Figure 3.37a shows the system response when an additional PV module is connected in parallel with the solar array. The maximum power point is reached after a transient-state required by *r* to find a position around the new maximum power point. It can be observed in Fig. 3.37b that the abrupt power decrease due to panel disconnection cuts the power delivery during almost 10 ms. This effect is caused by a small value of *r* which places the PV array operating point near the short-circuit point. Once that *r* has recovered the steady-state operating point, it exhibits a stable oscillation around the maximum power point.

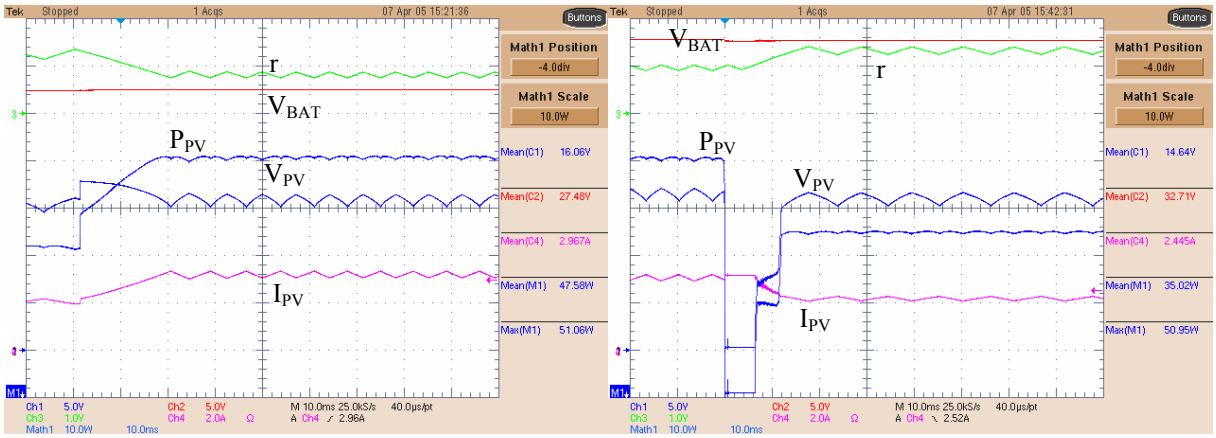

a) connection *b) disconnection*

Fig. 3.37 Response to a parallel connection of an additional panel.

C) DC voltage source in series with the PV generator

Figure 3.38 shows the system response to the insertion of a 5 V voltage source in series with the PV generator. It can be seen that the system reacts very fast by adapting variable *r* to the new situation.

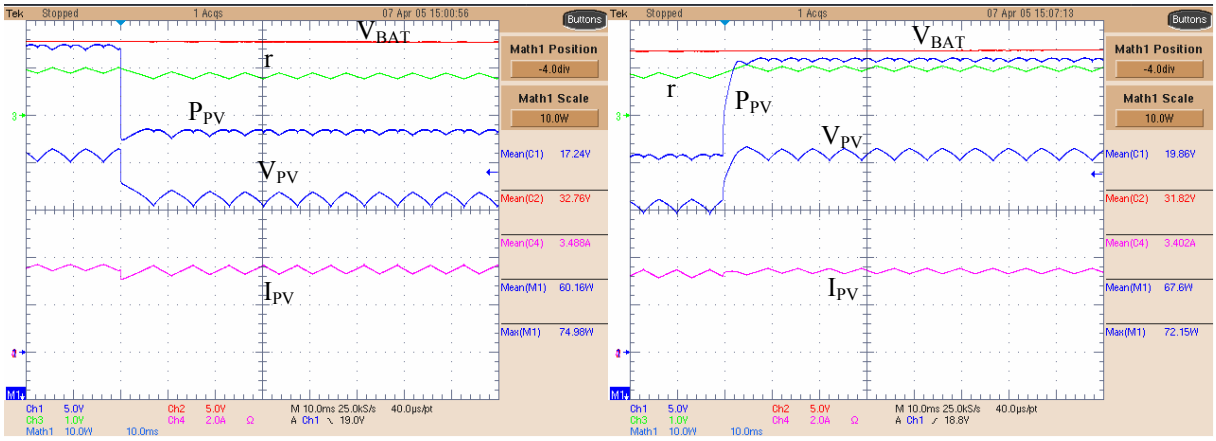

a) connection *b) disconnection*

Fig. 3.38 Response to a series connection of an additional 5 V dc source.

Due to the input saturation of the analog multiplier, the maximum value of r is limited. Hence, the system does not work for low irradiation values since the analog multiplier cannot provide the reference required by the input current.

3.5 Conclusion

In this chapter, some energy processing functions performed by power gyrators have been presented. First, it has been shown that G-gyrators can be indirectly used to perform current addition by connecting in parallel the output ports of the power gyrators. It has been also demonstrated that this parallel connection can be improved by including a control loop for balancing the current distribution. This improvement has been demonstrated by means of simulation in the case of a master-slave current distribution. It has been demonstrated by both simulation and experimental test in the case of a democratic current sharing.

We have also studied the combination of *v-i* and *i-v* conversion in order to generate new architectures suitable for high power system applications. It has been verified by means of simulation and experimentally that a structure of the type *v-i-v* can be efficiently implemented by a cascade connection of several paralleled G-gyrators and a power R-gyrator at the output stage.

Finally, it has been shown that power gyrators can be used as impedance matching circuits. It has been proved that a power gyrator can be used to track the maximum power point of a PV array. The tracking is performed by varying the conductance g (or the resistance r) of the power gyrator. The variation of g (r) is determined by a suitable MPPT algorithm. In our case, an algorithm based on the notion of extremum seeking control has been used [27]. It has been demonstrated that a BOF converter-based R-gyrator can be used to charge a battery whose nominal voltage is higher than the open circuit voltage of the PV array. Also, it has been shown that a BIF converter-based G-gyrator can be used to charge a battery whose nominal voltage is smaller than the open circuit voltage of the PV array. The Cuk converter-based G-gyrator with controlled input current has been proved to be a versatile solution for solar battery chargers since it can be used to charge any battery irrespective of its nominal voltage.

CHAPTER 4

4 VOLTAGE REGULATION BY MEANS OF GYRATORS

4.1 Introduction

It has been demonstrated in the previous chapters that power gyrators can be systematically designed by means of either sliding-mode or PWM-nonlinear control techniques for variable switching or constant switching frequency respectively. The gyrators constructed with such techniques perform the *v-i* and *i-v* conversions and can be regulated for maximum power point tracking.

We will show in this chapter that power gyrators can also be employed to regulate the system output voltage. It will be demonstrated that this regulation can be individually performed and that it can also be carried out by means of the parallel connection of power gyrators of type G.

4.2 Voltage regulation by means of a single G-gyrator

Fig. 4.1 shows the block diagram of a dc-to-dc switching regulator based on a BIF-G gyrator operating at variable switching frequency.

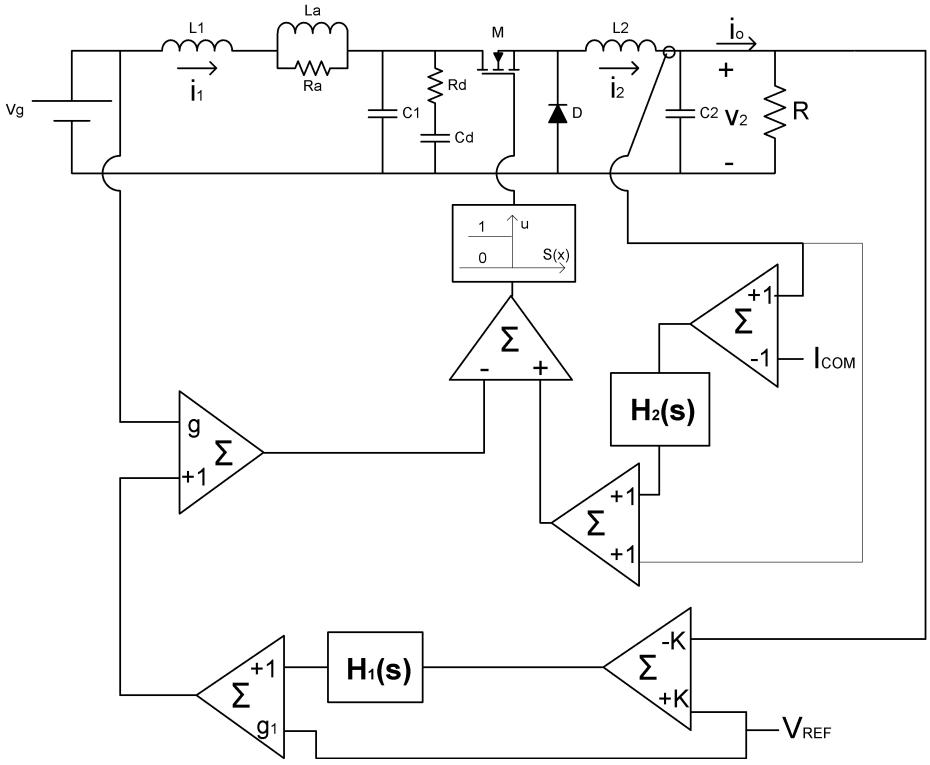

Fig. 4.1 Block diagram of a dc-to-dc switching regulator based on a BIF-G-Gyrator with variable switching frequency

The regulator consists of two control loops. An inner loop process the output current by means of the transfer function $H_2(s)$ and establishes a reference I_{COM} in steady-state for the output current. Another loop provides the voltage regulation through $H_1(s)$ and the variation of the product gV_g. Note that in steady-state, we can write

$$S(x) = gV_g + g_1 V_{REF} - I_2 = 0 \tag{4.1}$$

$$V_2 = RI_2 \tag{4.2}$$

From (4.1) and (4.2) we derive

$$V_2 = RgV_g + g_1 RV_{REF} \tag{4.3}$$

Expression (4.3) shows the dependence of the output voltage on the reference voltage V_{REF}. The nature of voltage step-down of the switching regulator has to be preserved in (4.3), i.e., it has to be guaranteed that $v_2 < V_g$.

It has been assumed in (4.1) that $I_{COM} = I_2$ because in the case of voltage regulation based on a single gyrator no current control loop will be employed as illustrated in Fig. 4.2. I_{COM} and $H_2(s)$ will be used when paralleling several G-gyrators. In such case I_{COM} will establish the reference current for each gyrator and it will be obtained by weighting the output current values of each gyrator as follows

$$I_{COM} = \mu_1 I_{21} + \mu_2 I_{22} + \cdots + \mu_n I_{2N} \tag{4.4}$$

where I_{21}, I_{22}, ... , I_{2N} are respectively the output currents of gyrator 1, gyrator 2, … , gyrator N whose output ports are connected in parallel.

For the democratic sharing $\mu_1 = \mu_2 = ... = \mu_N = \frac{1}{N}$, i.e., I_{COM} is the mean value of all output currents.

In the case of a master-slave current distribution $\mu_1 = 1$, $\mu_2 = \mu_3 = ... = \mu_N = 0$ and therefore $I_{COM} = I_{21}$.

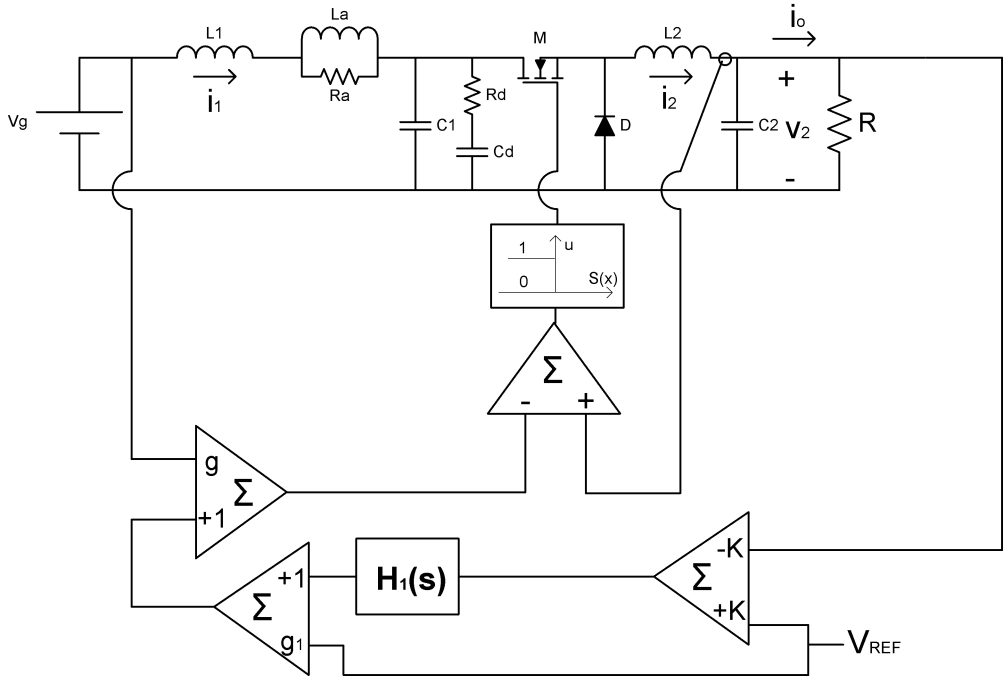

Fig. 4.2 Block diagram of a dc-to-dc switching regulator based on a single BIF-G-gyrator with variable switching frequency

4.2.1 Switching regulator dynamic model

In steady state output current I_2 and input voltage V_g of a G-gyrator are related as follows

$$I_2 = \langle i_2 \rangle_{SS} = gV_g \tag{4.4}$$

Fig. 4.3 illustrates both steady and transient states of output current i_2 for a constant input voltage. We assume that the transient state is due to a load perturbation.

Current i_2 is varying between i_M and i_m related by the hysteretic width ΔH as follows

$$i_M = i_m + \Delta H \tag{4.5}$$

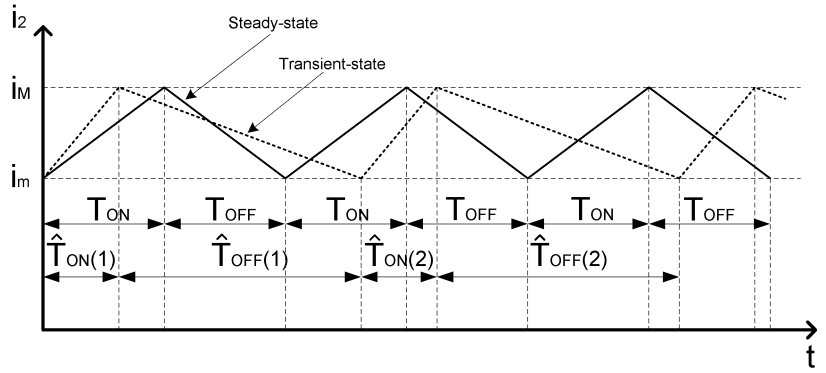

Fig. 4.3 Steady-state and transient-state of output current i_2 in a G-gyrator for a constant input voltage

The average value of output current i_2 in one cycle in steady-state will be given by

$$\langle i_2 \rangle_{SS} = \frac{i_M + i_m}{2} \frac{T_{ON}}{T_{ON} + T_{OFF}} + \frac{i_M + i_m}{2} \frac{T_{OFF}}{T_{ON} + T_{OFF}} = \frac{i_M + i_m}{2} \tag{4.6}$$

Similarly, the average value in a generic i^{th} cycle in transient-state will be expressed as

$$\langle i_2 \rangle_{TS} = \frac{i_M + i_m}{2} \frac{\hat{T}_{ON}(i)}{\hat{T}_{ON}(i) + \hat{T}_{OFF}(i)} + \frac{i_M + i_m}{2} \frac{\hat{T}_{OFF}(i)}{\hat{T}_{ON}(i) + \hat{T}_{OFF}(i)} = \frac{i_M + i_m}{2} \tag{4.7}$$

Therefore

$$\langle i_2 \rangle_{SS} = \langle i_2 \rangle_{TS} = gV_g \tag{4.8}$$

where the input voltage is assumed to be constant.

Therefore, for a constant input voltage, the average value of the output current remains constant when a load perturbation appears. The load perturbation changes the current slope during T_{ON} and T_{OFF} and therefore the switching period.

On the other hand, as shown in section 2.2.1.1.1, a step change in the input voltage results in a current change as illustrated in Fig. 4.4.

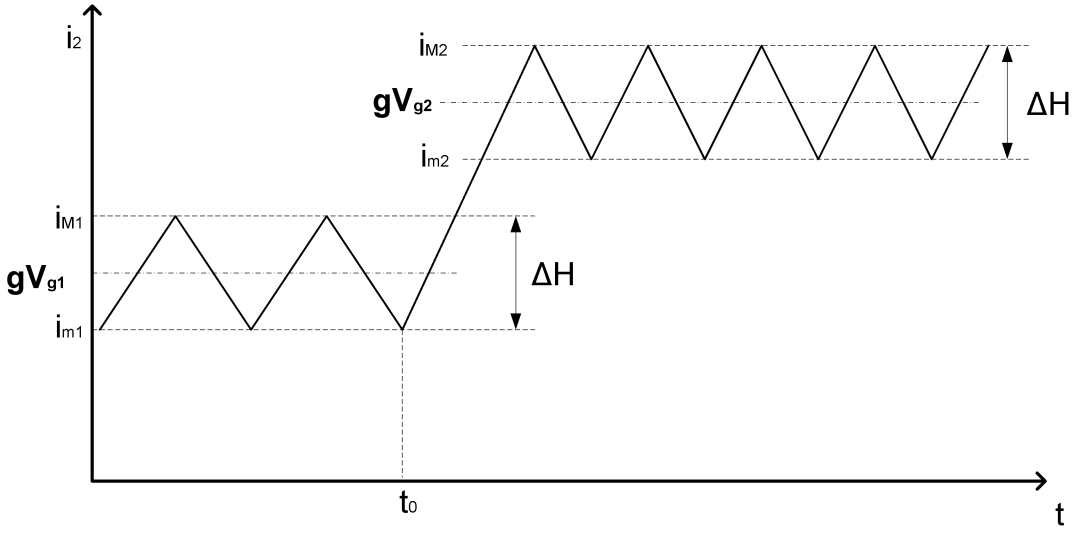

Fig. 4.4 Steady-state and transient-state of output current i_2 in a G-gyrator for a step change in the input voltage.

In this case, the average value follows exactly the dynamics imposed by the input voltage variation which changes abruptly at instant t_0 from V_{g1} to V_{g2}.

The switching frequency in the new steady-state has also changed because the slope of the current depends on the value of V_g. However, the current ripple is the same in all the states since is fixed by the hysteretic comparator.

Therefore, the perturbed state $\hat{i}_2$ corresponding to the average value of the output current will be given by

$$\hat{i}_2(t) = g\hat{v}_g(t) \tag{4.9}$$

where $\hat{v}_g(t)$ is the perturbed value of the input voltage.

Moreover, the output voltage perturbation $\hat{v}_o(t)$ is related to $\hat{i}_2(t)$ as follows

$$\hat{V}_2(s) = \hat{I}_2(s)\frac{R}{RC_2 s + 1} \tag{4.10}$$

where $\hat{V}_2(s)$ and $\hat{I}_2(s)$ are the Laplace transforms of perturbed output voltage and perturbed output current respectively.

On the other hand, the open-loop output impedance $Z_{oo}(s)$ will be given by

$$Z_{OO}(s) = \left.\frac{\hat{V}_2(s)}{\hat{I}_o(s)}\right|_{\hat{v}_g(s)=0} = \frac{R}{RC_2 s + 1} \tag{4.11}$$

where $\hat{I}_o(s)$ is an output load perturbation.

Taking into account (4.9), (4.10) and (4.11), the dynamic model corresponding to the block diagram depicted in Fig. 4.2 can be represented as shown in Fig. 4.5.

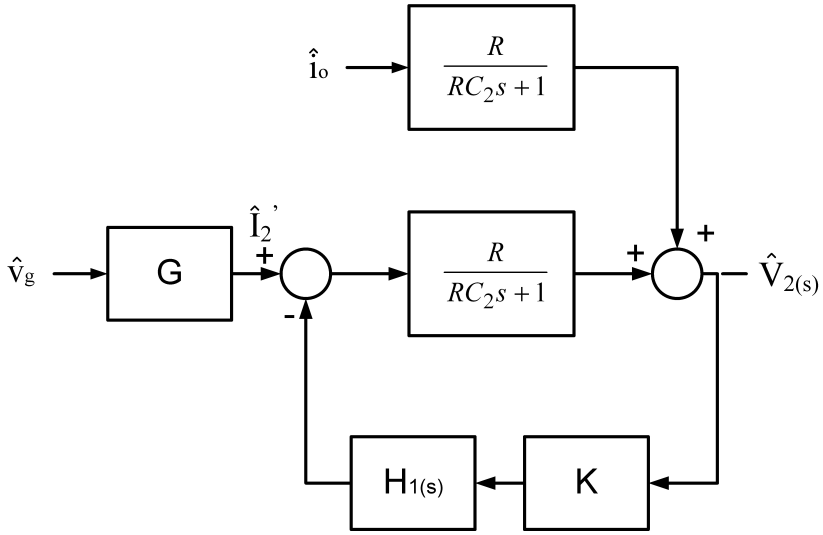

Fig. 4.5 Dynamic model of the gyrator-based voltage switching regulator depicted in Fig. 4.2.

The transfer function $\frac{\hat{V}_2(s)}{\hat{I}_2'(s)}$ will be given by

$$\frac{\hat{V}_2(s)}{\hat{I}_2'(s)} = \frac{\dfrac{R}{RC_2s+1}}{1+\dfrac{R}{RC_2s+1}K\,H_1(s)} = \frac{R}{RC_2s+1+RK\,H_1(s)} \tag{4.12}$$

and the regulator audiosusceptibility will be expressed as

$$A(s) = \frac{\hat{V}_2(s)}{\hat{v}_g(s)} = \frac{GR}{RC_2s+1+RK\,H_1(s)} \tag{4.13}$$

Assume now a step change of the input voltage at instant t_0 as depicted in Fig. 4.6

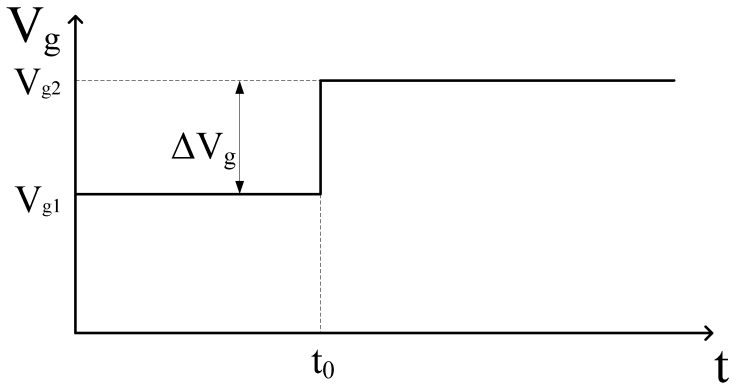

Fig. 4.6 Step change of the input voltage

The steady-state value of the output perturbation ΔV_2 can be calculated by means of the final value theorem.

$$\Delta v_2 = \hat{v}_2(\infty) = \lim_{s\to 0} s\hat{V}_2(s) = \lim_{s\to 0} s\hat{V}_g(s)A(s) \tag{4.14}$$

where $\hat{v}_g(s) = \dfrac{\Delta v_g}{s}$

Hence, (4.14) becomes

$$\Delta v_2 = \lim_{s\to 0} s\frac{\Delta v_g}{s}\frac{GR}{RC_2 s + 1 + RKH_1(s)} = \frac{GR}{1 + RKH_1(0)}\Delta v_g \tag{4.15}$$

Note that if $H_1(0) \to \infty$, $\Delta v_2 = 0$ and therefore no steady-state tracking error of the desired output voltage will remain.

The most simple transfer function having a pole at the origin of the s plane is a PI controller expressed as

$$H_1(s) = K_P + \frac{K_I}{s} \tag{4.16}$$

On the other hand, a step change of the load current as shown in Fig. 4.7 will produce a perturbation in the output voltage given by

$$\hat{V}_2(s) = \hat{I}_o(s)Z_{of}(s) \tag{4.17}$$

where $Z_{of}(s)$ is the closed-loop output impedance and $\hat{I}_o(s) = \dfrac{\Delta i_o}{s}$

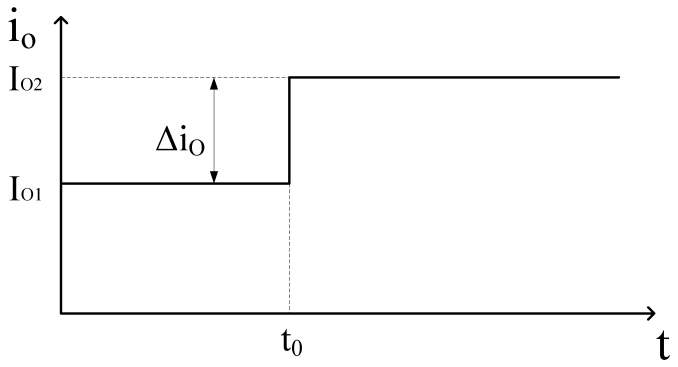

Fig. 4.7 Step change of the load current

From Fig. 4.5, it can be deduced that

$$Z_{of}(s) = \left.\frac{\hat{V}_2(s)}{\hat{I}_o(s)}\right|_{\hat{v}_g(s)=0} = \frac{Z_{oo}(s)}{1 + T(s)} \tag{4.18}$$

where

$$T(s) = \frac{R}{RC_2 s + 1}KH_1(s) \tag{4.19}$$

The steady-state value of the output perturbation Δv_2 will be in this case

$$\Delta v_2 = \hat{v}_2(\infty) = \lim_{s\to 0} s \frac{\Delta i_o}{s} \frac{Z_{oo}(s)}{1+T(s)} = \Delta i_o \frac{R}{1+T(0)} \tag{4.20}$$

where $T(0) = RKH_1(0)$

Again, if $H_1(0) \to \infty$, the steady-state tracking error of the desired output voltage will be zero.

4.2.2 Circuit realization of the voltage control loop

The feedback path depicted in Fig. 4.2 can be implemented by means of the circuit scheme illustrated in Fig. 4.8.

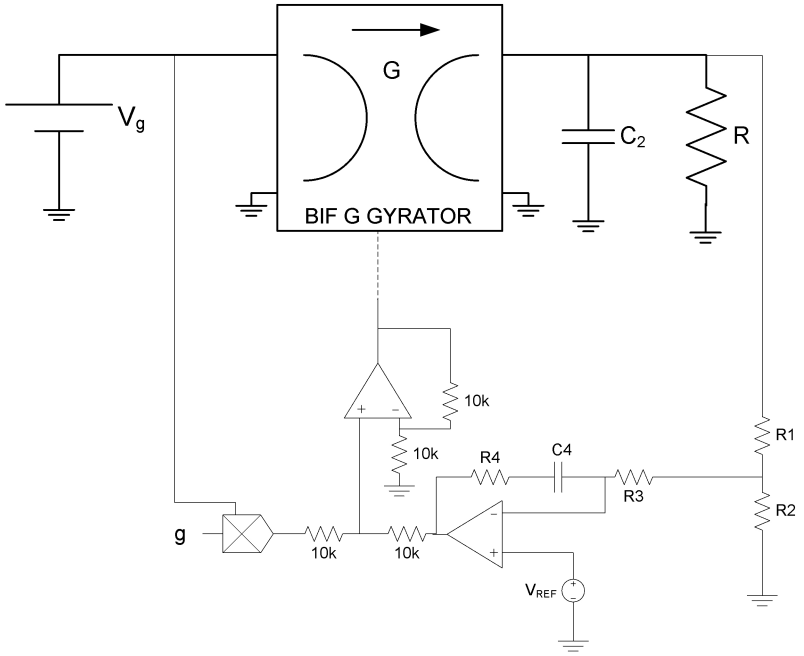

Fig. 4.8 Circuit implementation of the feedback path depicted in Fig. 4.2

The analysis of the circuit illustrated in Fig. 4.8 shows that the gain *K* of the block diagram depicted in Fig. 4.5 is given by

$$K = \frac{R_2}{R_1 + R_2} \tag{4.21}$$

The transfer function $H_1(s)$ will be expressed as

$$H_1(s) = \frac{Z_2(s)}{Z_1(s)} \tag{4.22}$$

where

$$Z_2(s) = R_4 + \frac{1}{C_4 s} \quad \text{and} \quad Z_1(s) = R_3 + \frac{R_1 R_2}{R_1 + R_2} \overset{\Delta}{=} R_6 \tag{4.23}$$

Therefore, the PI parameters K_P and K_I are given by

$$K_P = \frac{R_4}{R_6} \tag{4.24}$$

$$K_I = \frac{1}{C_4 R_6} \tag{4.25}$$

Finally, by simple comparison of Figs. 4.2 and 4.8, we find that $g_1 = 1$.

4.2.3 Simulated and experimental results

A practical implementation of the block diagram depicted in Fig. 4.2 is shown in Fig. 4.9 for the set of parameters $V_g = 20\ V$, $R = 1\ \Omega$, $g = 0.5\ \Omega^{-1}$, $L_1 = 12\ \mu H$, $C_1 = 12\ \mu F$, $C_d = 100\ \mu F$, $R_d = 2.2\ \Omega$, $L_2 = 35\ \mu H$, $C_2 = 6.6\ \mu F$, $L_a = 22\ \mu H$, $R_a = 1.2\ \Omega$ and C_4 =1.5 nF $R_3 = 2.5\ k\Omega$, $R_4 = 5\ k\Omega$, $R_1 = 15\ k\Omega$ and $R_2 = 1\ k\Omega$.

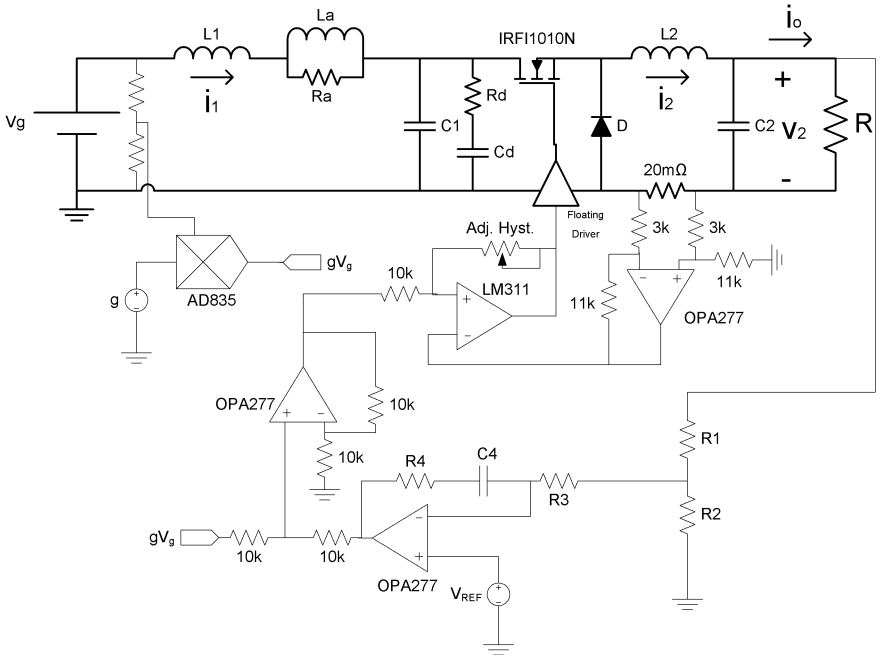

Fig. 4.9 Practical implementation of a voltage regulator based on a single BIF-G-gyrator with variable switching frequency

Figs. 4.10 and 4.11 show respectively the simulated output voltage response to input voltage variations and output load perturbations. The input voltage variations are of step-type passing from 20 V to 24 V and returning to 20 V, and the load perturbations are also abrupt changes from 2 Ω to 1 Ω and return to 2 Ω . In both cases the control attenuates the influence of the input perturbation by forcing a fast transient-state with low overshoot and a recovery of the steady-state with zero tracking error.

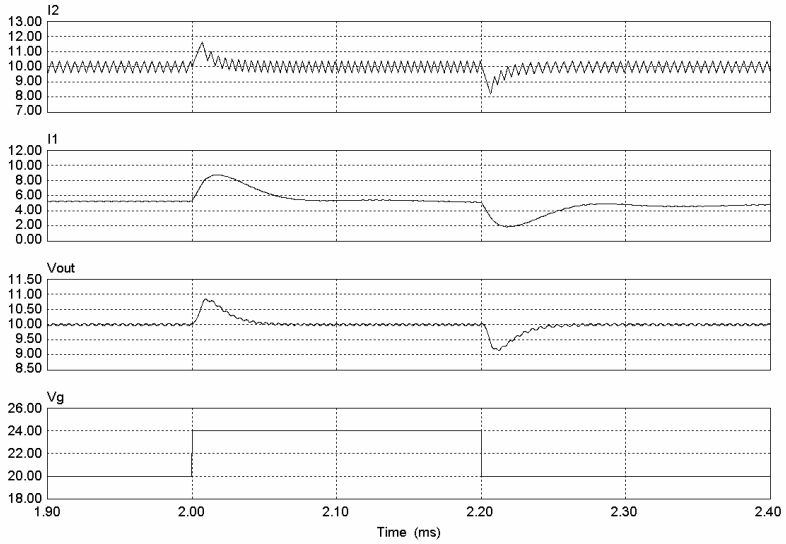

Fig. 4.10 *Simulated output response of the gyrator-based voltage regulator for input voltage perturbations of step-type.*

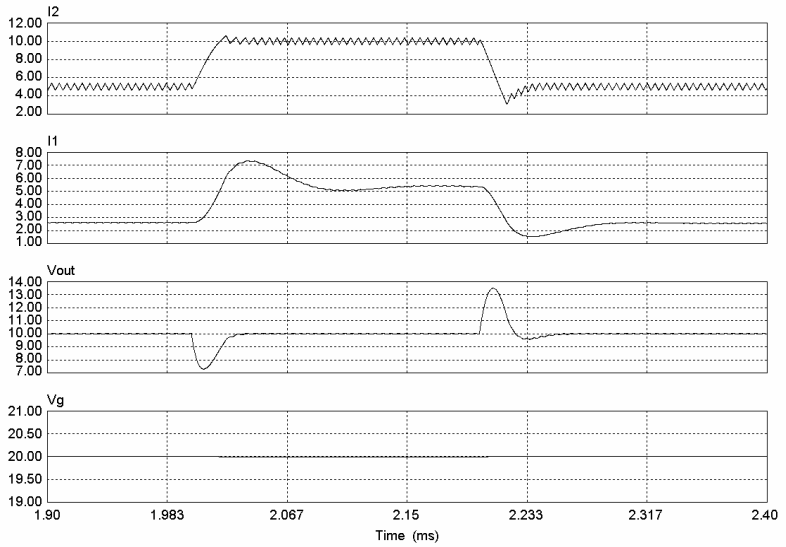

Fig. 4.11 *Simulated output response of the gyrator-based voltage regulator for output load perturbations of step-type*

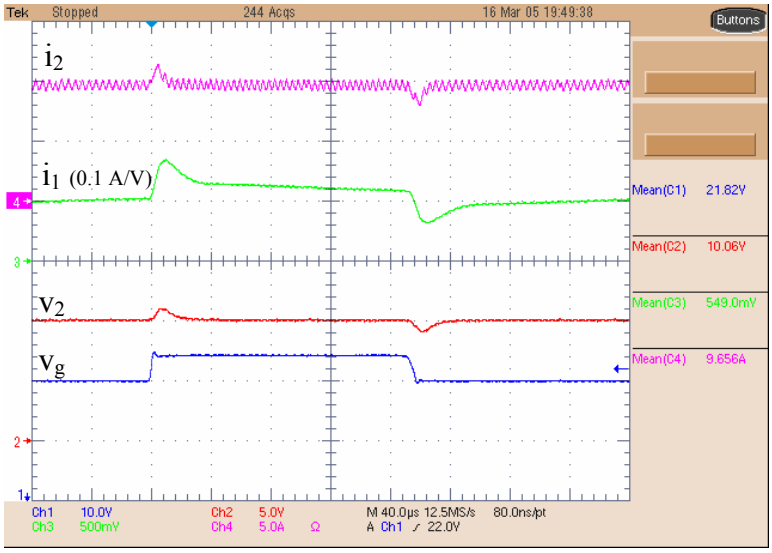

Fig. 4.12 *Experimental output response of the gyrator-based voltage regulator for input voltage perturbations of step-type*

Figs. 4.12 and 4.13 are in correspondence with figs 4.10 and 4.11 respectively and show the experimental results of the prototype of Fig. 4.9 for the step variations and load changes above described.

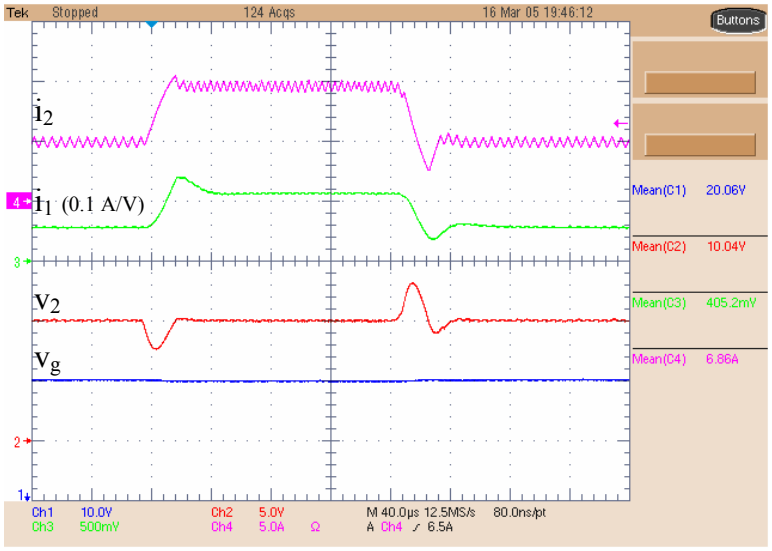

Fig. 4.13 *Experimental output response of the gyrator-based voltage regulator for input voltage perturbations of step-type.*

4.3 Voltage regulation based on paralleled gyrators

Fig 4.14 shows a simplified block diagram that describes the democratic or master-slave current-sharing schemes for a *n* G-gyrators connected in parallel at the output port, with only the first and j^{th} gyrator shown. To generate a common reference I_{COM}, each gyrator provides a

measurement of its output current i_{2j} which is then processed by a linear circuit which multiplies i_{2j} by μ_j and then adds the signals $\mu_j i_{2j}$ to obtain I_{COM} . When the gains μ_1 through μ_n are equal to $1/n$, we have the democratic current-sharing scheme. When μ_1 and μ_2 through μ_n are zero, we have the master-slave current-sharing scheme with gyrator 1 being the master and the others the slaves. In each gyrator, for example gyrator j, the signal I_{COM} is compared to the output of that gyrator to get a current-error signal. The current-error signal is processed by the block with transfer function $H_{2j}(s)$. The signal $H_{2j}(i_{2j}-i_{COM})$ is added to the reference current i_{COM} of gyrator j in order to drive its output current i_{2j} to approximately to i_{COM}, thus ensuring that all converters maintain approximately equal output currents. A common external loop for all gyrators establishes the output voltage regulation though $H_1(s)$ and the variation of the product $g_j V_{gj}$ as in the case of voltage regulation based on a single g-gyrator.

The stability of the parallel connection illustrated in Fig. 4.14 will be analyzed in the next sections. We will proceed first by modeling the dynamic behavior of the active current sharing in a generic gyrator.

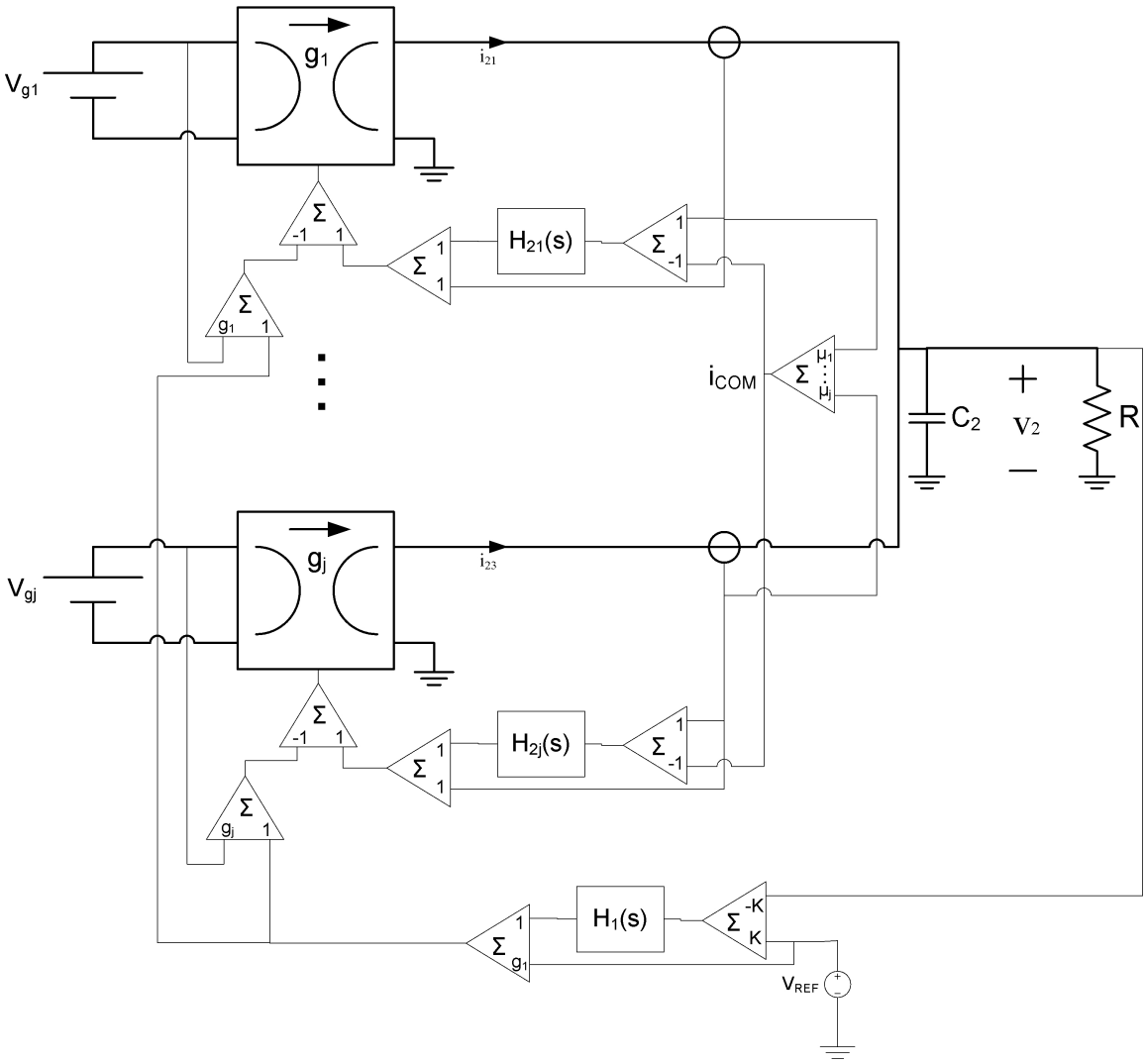

Fig. 4.14 Voltage regulation based on n-paralleled gyrators with active current-sharing.

4.3.1 Dynamic model of the current loop

Consider the j^{th} gyrator in the block diagram of Fig. 4.14.

In steady-state, the gyrator output current is given by

$$I_{2j} = g_j V_{gj} \tag{4.26}$$

Perturbing (4.26) leads to the following dynamic relation

$$\hat{i}_{2j} = g_j \hat{v}_{gj} \tag{4.27}$$

On the other hand, we can write in the Laplace domain

$$\hat{I}_{2j}(s) + \hat{I}_{2j}(s)H_2(s) - \hat{I}_{COM}(s)H_2(s) = g\hat{V}_{gj}(s) \tag{4.28}$$

Solving $\hat{I}_{2j}(s)$ for in (4.28) yields

$$\hat{I}_{2j}(s) = \frac{g_j \hat{V}_{gj}(s)}{1+H_2(s)} + \hat{I}_{COM}(s)\frac{H_2(s)}{1+H_2(s)} \tag{4.29}$$

Equation (4.29) can be modeled as shown in Fig. 4.15 where the input from the voltage regulation loop has been also included.

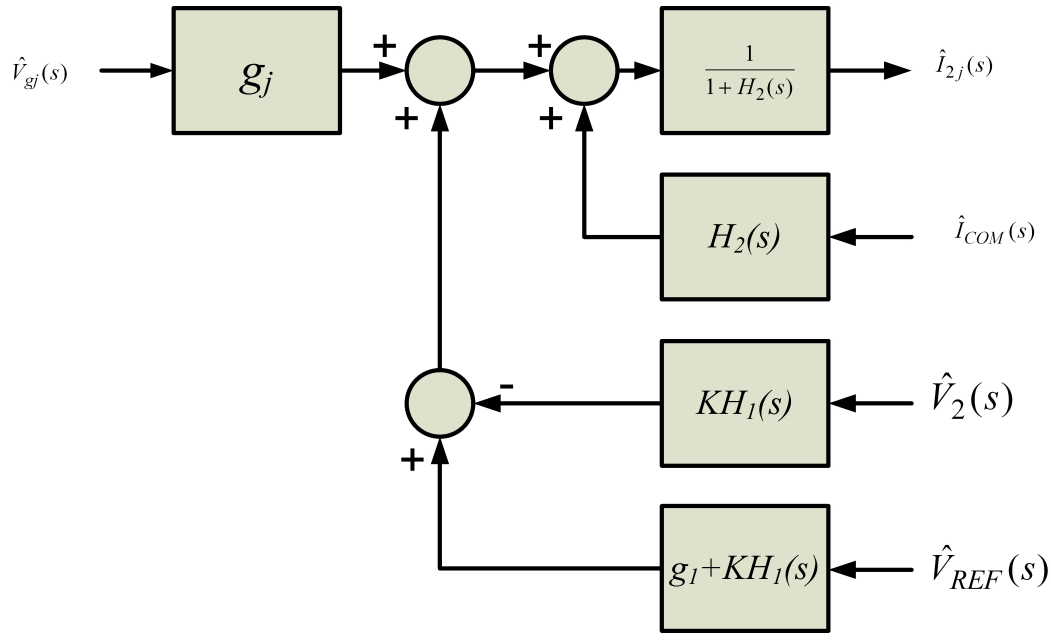

Fig. 4.15 Dynamic model of the j^{th} gyrator in the paralleled connection depicted in Fig. 4.14

The dynamic model of Fig. 4.15 can be described in terms of the circuit representation of Fig. 4.16.

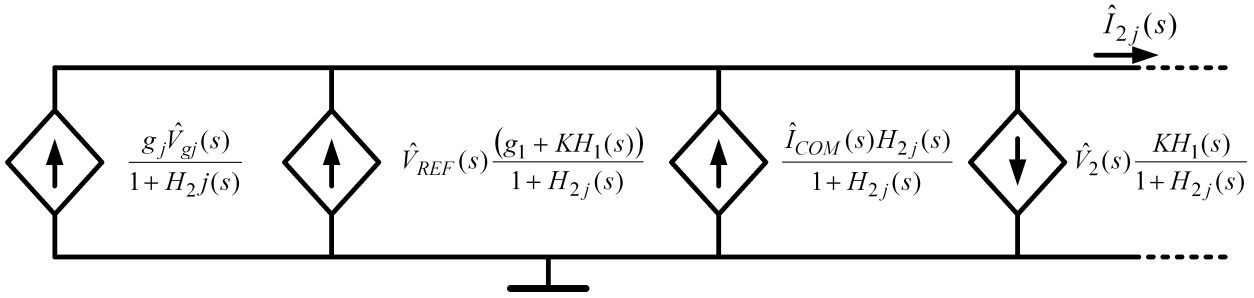

Fig. 4.16 Circuit configuration of the dynamic model described in the block diagram of fig. 4.15

4.3.2 Dynamic model of the n-paralleled gyrators

The circuit of the fig. 4.16 will be used to describe the dynamic behavior of the paralleled connection depicted in fig. 4.14. Without loss of generality, it will be assumed $g_1=1\ \Omega^{-1}$ as well as $g_j=g$ and $H_{2j}(s)=H_2(s)$ for $j= 1, ..., n$. Therefore, the resulting dynamic model for the paralleled connection of n gyrators is the circuit shown in fig. 4.17, which, in turn, can be simplified as illustrated in fig. 4.18.

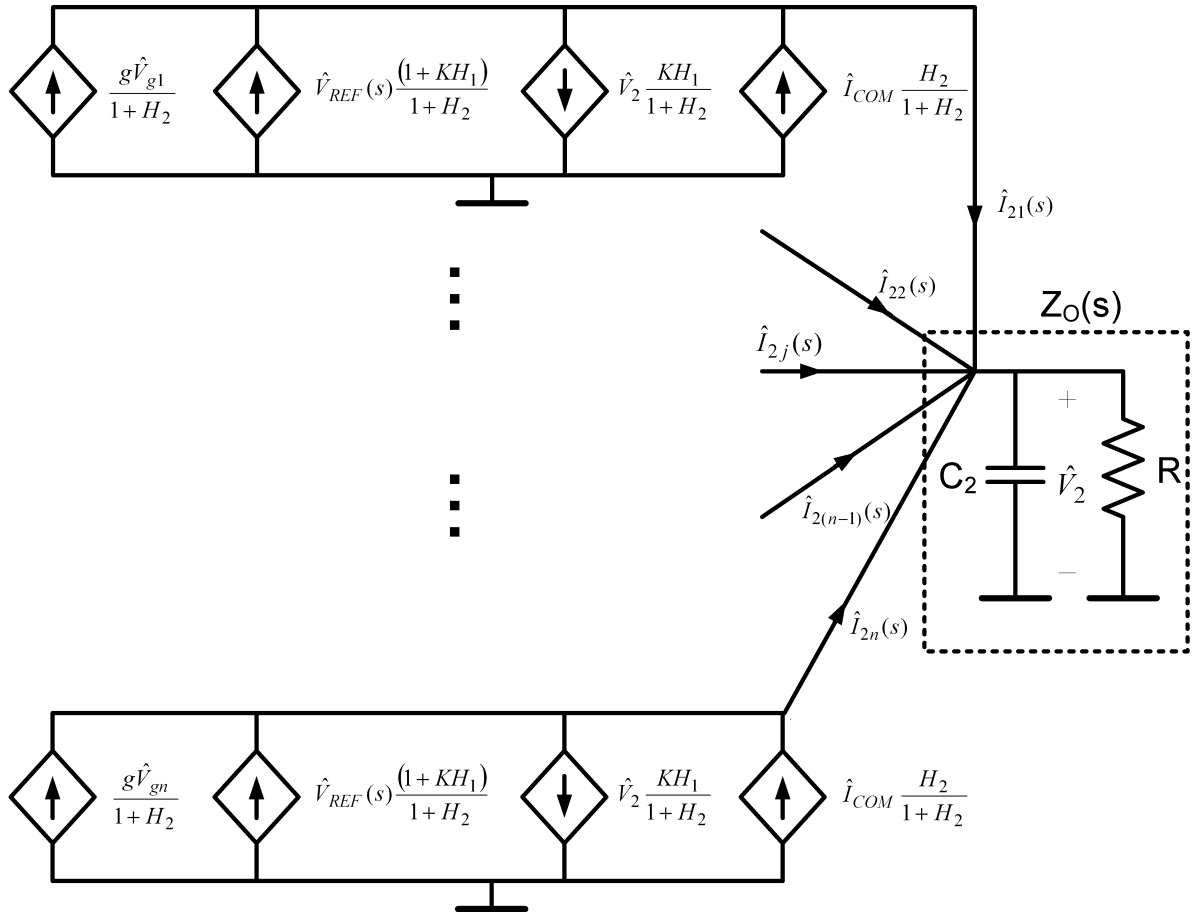

Fig. 4.17 Dynamic model of the voltage regulator based on the gyrators paralleling depicted in fig. 4.14

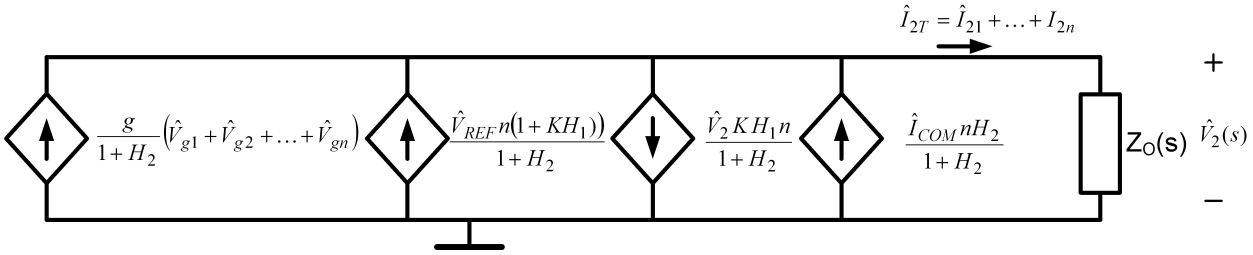

Fig. 4.18 Simplified version of the circuit depicted in Fig. 4.17

4.3.3 Stability analysis for democratic sharing

The stability of the paralleled connection of fig. 4.14 will be ensured in a perturbation in the reference voltage when $\hat{v}_{g1} = \hat{v}_{g2} = \ldots = \hat{v}_{gn} = 0$ will result in a stable transient state for $v_2(t)$ and all gyrator currents $i_{21}(t)$, $i_{22}(t)$, $i_{2n}(t)$.
Therefore, assuming $\hat{v}_{gj} = 0$ for *j = 1, ..., n*, the circuit of 4.18 will be described by the following equation

$$\left[\hat{V}_{REF}(s)\frac{(1+KH_1(s))n}{1+H_2(s)} - \frac{KH_1(s)n\hat{V}_2(s)}{1+H_2(s)} + \frac{H_2(s)n}{1+H_2(s)}\hat{I}_{COM}(s)\right]Z_O(s) = \hat{V}_2(s) \qquad (4.30)$$

After grouping some terms, we obtain

$$\hat{V}_{REF}(s)\frac{(1+KH_1(s))}{1+H_2(s)}nZ_O(s) = \hat{V}_2(s)\left[1+\frac{KH_1(s)nZ_O(s)}{1+H_2(s)}\right] - \hat{I}_{COM}(s)\frac{H_2(s)nZ_O(s)}{1+H_2(s)} \qquad (4.31)$$

Taking into account that $\hat{I}_{COM}(s) = \dfrac{\mu_1\hat{I}_{21}(s) + \ldots + \mu_n\hat{I}_{2n}(s)}{n}$ equation (4.31) becomes

$$\begin{aligned}\hat{V}_{REF}(s)\frac{1+KH_1(s)}{1+H_2(s)}nZ_O(s) &= \hat{V}_2(s)\left[1+\frac{KH_1(s)nZ_O(s)}{1+H_2(s)}\right] - \\ &-\left[\frac{H_2(s)nZ_O(s)}{1+H_2(s)}\right]\left[\mu_1\hat{I}_{21}(s) + \ldots + \mu_n\hat{I}_{2n}(s)\right]\end{aligned} \qquad (4.32)$$

There are two transfer functions whose stability is required. These transfer functions are from the regulator reference voltage $\hat{v}_{REF}(s)$ to the regulator output voltage $\hat{V}_2(s)$, and from the regulator reference voltage to any gyrator output current $\hat{I}_{2j}(s)$. Hence, for the democratic sharing

$$\hat{V}_{REF}(s)\frac{1+KH_1(s)}{1+H_2(s)}nZ_O(s)=\hat{V}_2(s)\left[1+\frac{KH_1(s)nZ_O(s)}{1+H_2(s)}\right]-\left[\frac{H_2(s)nZ_O(s)}{1+H_2(s)}\right]\hat{I}_{2t}(s)=$$

$$=\hat{V}_2(s)\left[1+\frac{KH_1(s)nZ_O(s)}{1+H_2(s)}-\frac{H_2(s)nZ_O(s)}{1+H_2(s)}\right] \tag{4.33}$$

From (4.33) we derive

$$\frac{\hat{V}_2(s)}{\hat{V}_{REF}(s)}=\frac{(1+KH_1(s))nZ_O(s)}{KH_1(s)nZ_O(s)+1} \tag{4.34}$$

and

$$\left.\frac{\hat{I}_{2t}(s)}{\hat{V}_{REF}(s)}\right|=\frac{(1+KH_1(s))n}{KH_1(s)nZ_O(s)+1} \tag{4.35}$$

On the other hand,

$$\hat{I}_{2t}(s)=\hat{I}_{21}(s)+\ldots+\hat{I}_{2n}(s) \tag{4.36}$$

Therefore,

$$\frac{\hat{I}_{21}(s)}{\hat{V}_{REF}(s)}+\ldots+\frac{\hat{I}_{2n}(s)}{\hat{V}_{REF}(s)}=\frac{(1+KH_1(s))n}{KH_1(s)nZ_O(s)+1} \tag{4.37}$$

Assuming, equal influence of the reference voltage in all currents we can write

$$\frac{\hat{I}_{21}(s)}{\hat{V}_{REF}(s)}=\ldots=\frac{\hat{I}_{2n}(s)}{\hat{V}_{REF}(s)}=\ldots=\frac{(1+KH_1(s))}{KH_1(s)nZ_O(s)+1} \tag{4.38}$$

It can be observed that if transfer function (4.38) represents a stable system, it will be implied that transfer function (4.34) will also correspond to a stable system.

Let's assume now that voltage comparison is performed by means of a PI controller given by $H_1(s)=K_P+\frac{K_I}{s}$ while the current compensation is carried out by means of a low-pass filter whose transfer function is $H_2(s)=\frac{K_C}{s+p}$.

Hence, transfer function (4.38) becomes

$$\frac{\hat{I}_{2j}(s)}{\hat{V}_{REF}(s)} = \frac{1 + K\left(K_P + \dfrac{K_I}{s}\right)}{K\left(K_P + \dfrac{K_I}{s}\right)n\left(\dfrac{R}{RC_2 s + 1}\right) + 1} \tag{4.39}$$

After rearranging numerator and denominator, (4.39) becomes

$$\frac{\hat{I}_{2j}(s)}{\hat{V}_{REF}(s)} = \frac{(RC_2 s + 1)((1 + KK_P)s + KK_I)}{RC_2 s^2 + s(1 + KK_P nR) + KK_I nR} \tag{4.40}$$

The denominator polynomial is of second order and all the coefficients are positive. Therefore, we can conclude that transfer function (4.40) will correspond to a stable system and that no stability problems will arise in the system depicted in Fig. 4.14 irrespective of the number of power gyrators in parallel connection.

4.3.4 Simulation and experimental results

A practical implementation of the block diagram depicted in Fig. 4.14 is shown in Fig. 4.19 for the case of $n = 3$, democratic current sharing and the set of parameters $g = 0.5\ \Omega^{-1}$, $L_1 = 12\ \mu H$, $C_1 = 12\ \mu F$, $C_d = 100\ \mu F$, $R_d = 2.2\ \Omega$, $L_2 = 35\ \mu H$, $C_2 = 6.6\ \mu F$, $L_a = 22\ \mu H$ and $R_a = 1.2\ \Omega$ for each gyrator. The nominal input voltage of each gyrator is $V_{g1} = 20\ V$, $V_{g2} = 18\ V$ and $V_{g3} = 16\ V$. The output load is $R = 0.333\ \Omega$. The parameters of the voltage regulation loop are $C_4 = 1.5\ nF$, $R_3 = 2k7\ \Omega$, $R_4 = 5k6\ \Omega$, $R_1 = 15\ k\Omega$ and $R_2 = 1\ k\Omega$. The objective of the control is a regulated output voltage of 10 V.

Figs. 4.20 and 4.21 show respectively the simulated and experimental responses to ± 4 V input voltage perturbations of step type superposed on the nominal input voltage of gyrator 1. The input voltage of gyrators 2 and 3 remain constant at 18 V and 16 V respectively. It can be observed in both figures that there is a very small influence of the input voltage perturbation the regulated output voltage. The voltage control loop ensures a fast response with very small overshoot. Note that the internal current loop guarantees that the each gyrator delivers practically the same amount of current. The paralleled system delivers 201 W to an output load of 0.5 Ω with an efficiency of 90.3 %.

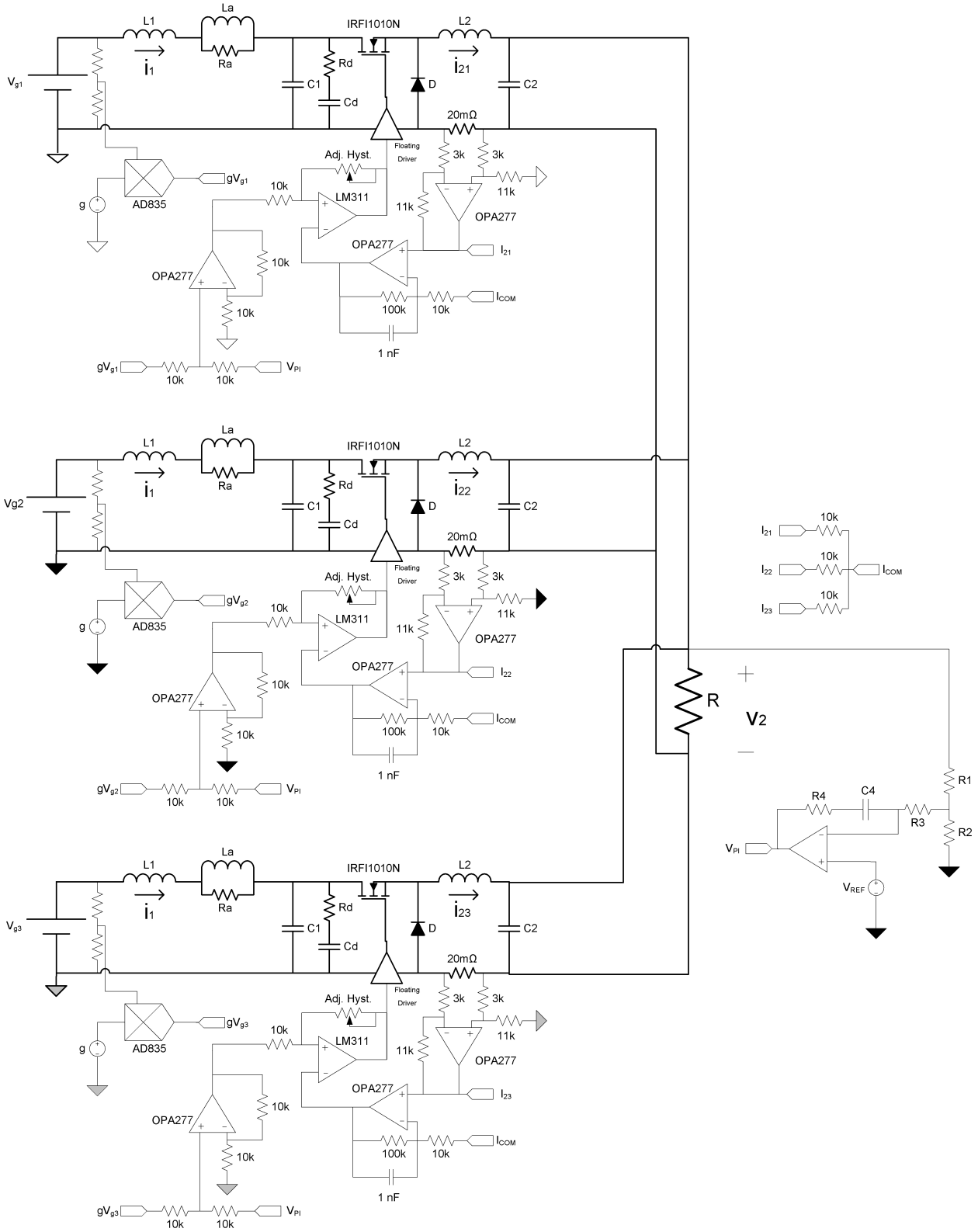

Fig. 4.19 *Practical implementation of a voltage regulator based on the parallel connection of three G-gyrators with democratic current sharing*

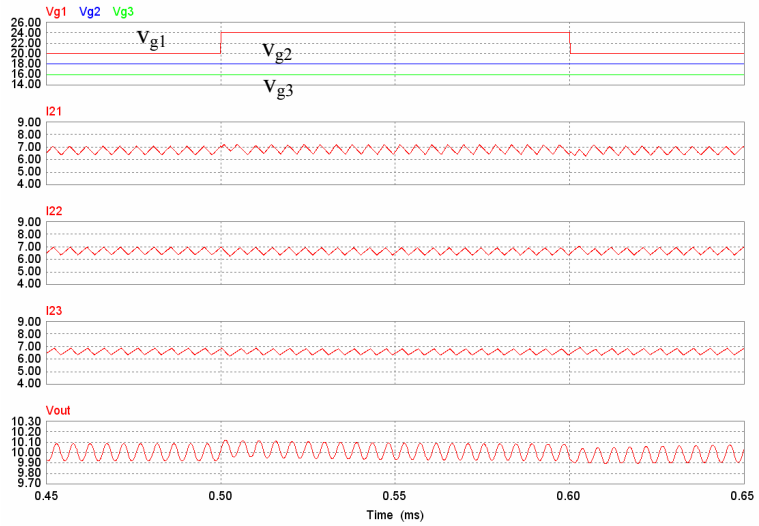

Fig. 4.20 *Simulated response of the circuit depicted in Fig. 4.19 to and input voltage perturbations of step-type in gyrator 1.*

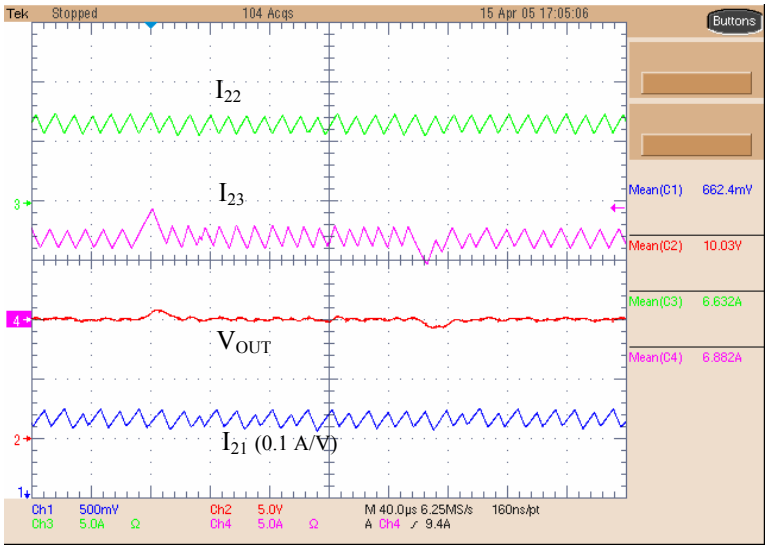

Fig. 4.21 *Experimental response of the circuit depicted in Fig. 4.19 to and input voltage perturbations of step-type in gyrator 1.*

On the other hand, figures 4.22 and 4.23 illustrate respectively the simulated and experimental behavior of the circuit of Figure 4.19 when load perturbations of step type are introduced. In this case, the load changes from 0.5 Ω to 0.333 Ω and returns to 0.5 Ω. The input voltage of each gyrator remains at its nominal value. Note that the control loop attenuates the influence of the load perturbation on the output voltage by means of a fast recovery of the steady-state (10 V) with small overshoot. It can be observed that the internal current loop action results in a balanced distribution of the gyrator output currents when absorbing the load perturbation. The parallel connection of the 3 G-gyrators delivers 300 W to the load with a 90 % efficiency.

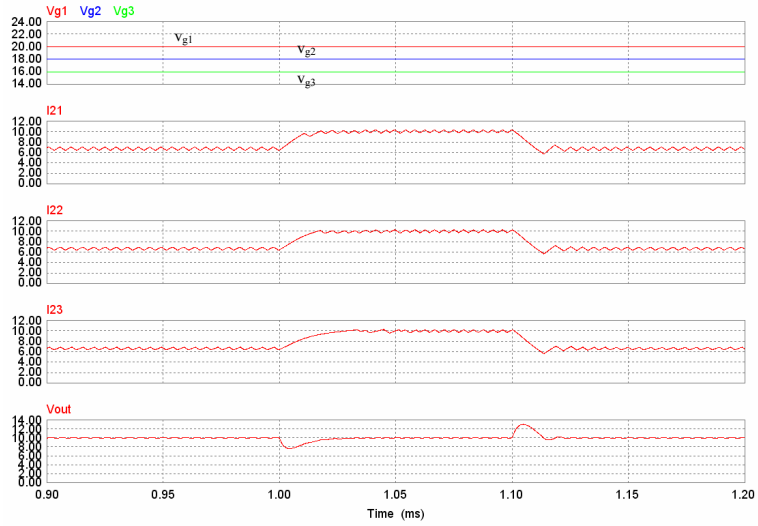

Fig. 4.22 *Simulated response of the circuit depicted in Fig. 4.19 to load perturbations of step-type*

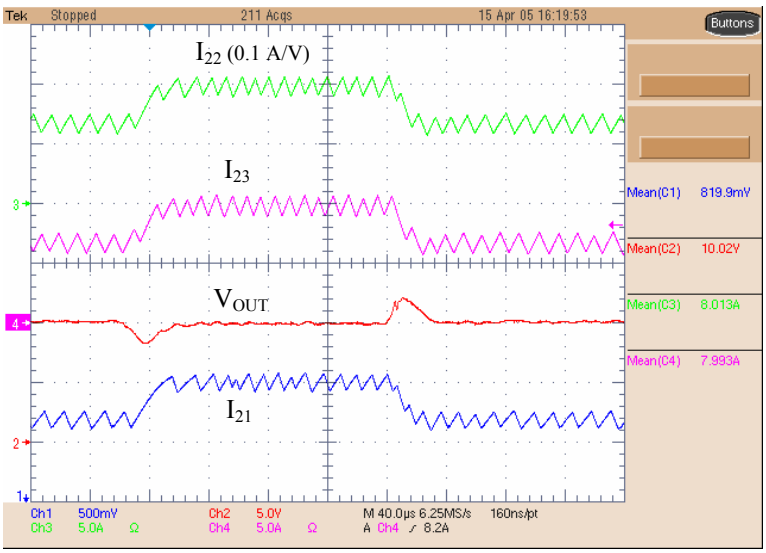

Fig. 4.23 *Experimental response of the circuit depicted in Fig. 4.19 to load perturbations of step-type*

Figure 4.24 shows the effect of gyrator 1 turning-off. It can be observed that gyrator 2 and gyrator 3 deliver the output by uniformly increasing their respective output currents. Similar balanced current distribution is observed in Fig. 4.25 by illustrating the effect of gyrator 1 turning-on.

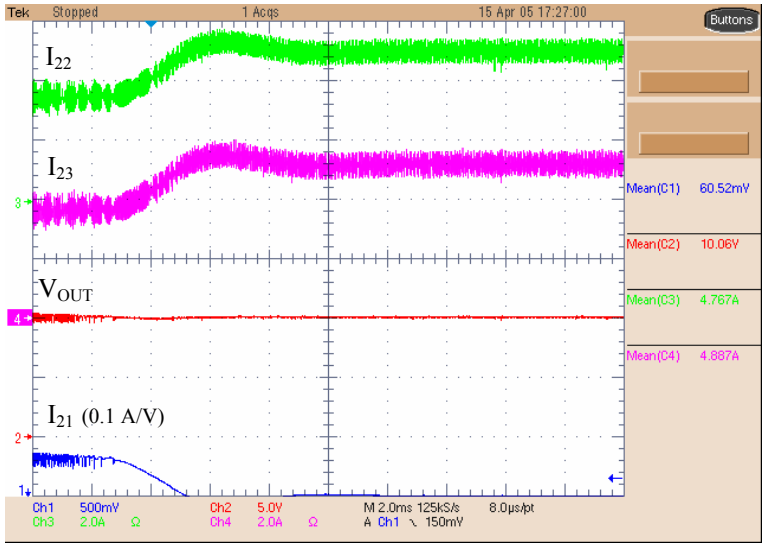

Fig. 4.24 *Effect of gyrator 1 turning-off in the response of the circuit depicted in Fig. 4.19*

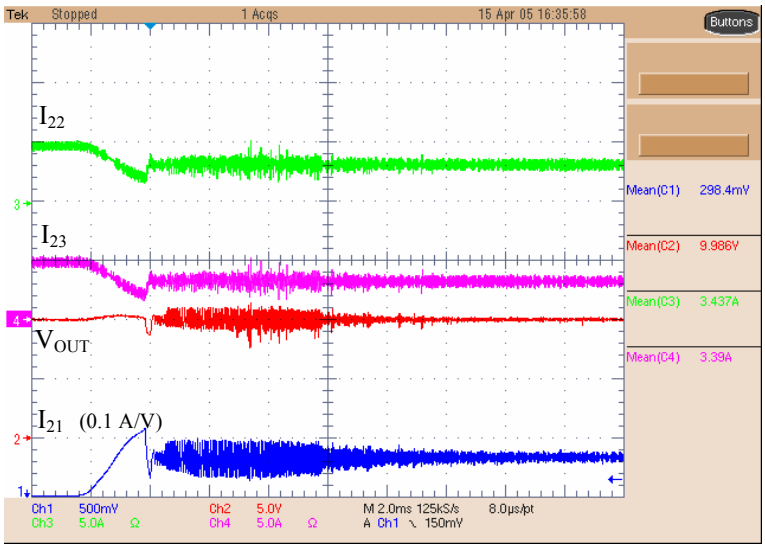

Fig. 4.25 *Effect of gyrator 1 turning-on in the response of the circuit depicted in Fig. 4.19*

4.4 Conclusions

In this chapter, it has been proved that DC voltage regulation can be performed by means of G-gyrator. The investigation has been carried out for a single gyrator and also for a more complex architecture based on the parallel connection of the gyrator output ports.

The voltage regulation analysis has required to develop first a dynamic model of both cases investigated, i.e., a switching regulator based on a single gyrator and a switching regulator based on n-parallel gyrators with active current sharing. Based on the dynamic model, a voltage regulation loop has been designed in both cases to ensure voltage regulation and meet standard requirements on transient response.

The dynamic model of n-parallel gyrators with democratic current sharing has shown that the system is stable irrespective of the number of gyrators in parallel connection.

The theoretical predictions have been verified by means of simulations and experiments using a BIF converter-based G-gyrator as a building block for the single case and for the parallel connection. A prototype based on three paralleled BIF-G gyrators has been tested showing a 90% efficiency when delivering 300 W to the load and exhibiting a fast recovery of the steady-state for input voltage variations and load perturbations.

CHAPTER 5

5 CONCLUSION AND FUTURE WORK

CONCLUSION AND FUTURE WORK

In this thesis, it has been shown that a power gyrator can be synthesized by imposing its output port equation, i.e., $I_2 = gV_1$ or $V_2 = rI_1$ by means of sliding-mode control to the steady-state of certain converters of 4^{th} order. A preliminary analysis has shown that BIF and Cuk converters can behave as G-gyrators if damping networks are inserted in the power stage and certain parametric conditions are accomplished. Moreover, it has been demonstrated that BOF converters can exhibit unconditionally stable R-gyrator characteristics either in sliding-mode or in limit cycles. The G-gyrators based on BIF and Cuk converters make possible the transformation of a voltage source at the input port into a current source at the output port. The BOF converter-based R-gyrators transform a current source at the input port into a voltage source at the output port.

BIF converter-based G-gyrators have been proved to be more efficient that G-gyrators based on the Cuk converter and, hence, have been chosen as candidates for converter paralleling. Fig. 5.1 shows the scheme of a BIF converter-based G-gyrator that delivers 101 W with 90 % efficiency. Its corresponding prototype is shown in figure 5.2

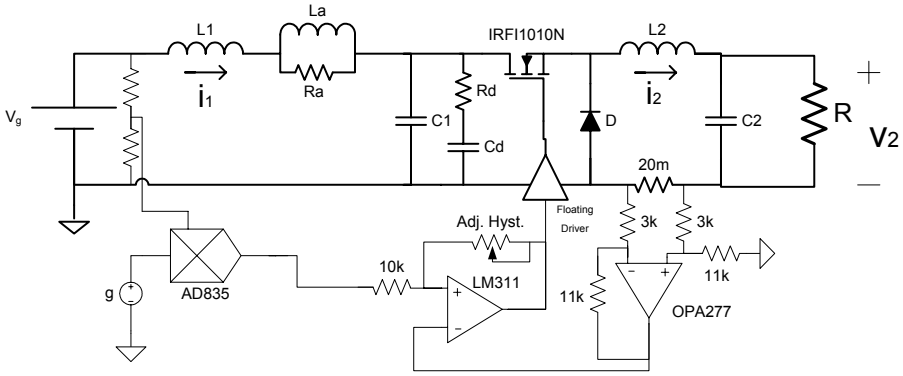

Fig.5.1 Circuit scheme of a BIF converter-based G-gyrator

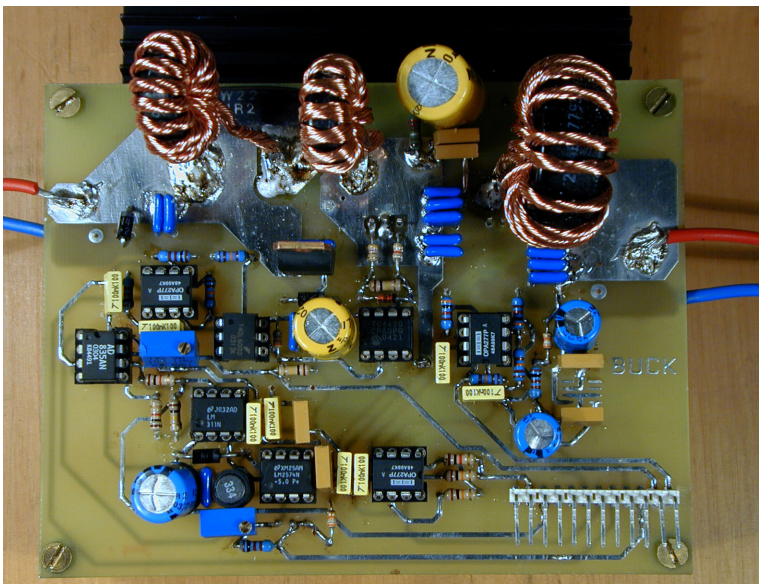

Fig.5.2 A 101 W BIF converter-based G-gyrator

On the other hand, another solution to the G-gyrator synthesis problem has been found. It consists in controlling the gyrator input current instead of the output current. It has been shown that BOF and Cuk converters make possible the realization of unconditionally stable gyrators of this type.

As a result of our classification, two new categories of switching regulators have been presented, namely, R and G semigyrators. They meet the power gyrator requirements of nonpulsating input and output currents in only one port. As a consequence, they will have higher EMI levels. It has been shown that the buck converter can be used in an unconditionally stable G-semigyrator operation. In addition, it has been demonstrated that the boost converter and the boost-shunt converter can present unconditionally stable R-semigyrator characteristics.

The synthesis of all gyrators has been solved first by means of the sliding-mode approach which implies variable switching frequency operation. The transition to constant switching frequency operation has been automatically carried out by using the equivalence between sliding-mode control and PWM zero dynamics-based nonlinear control reported in [20].

In addition to voltage to current and current to voltage conversion which are intrinsic to the nature of G and R gyrators respectively, impedance matching and voltage regulation by means of power gyrators have been investigated.

The most important case of impedance matching analyzed in this thesis has been the MPPT problem in photovoltaic arrays. It has been demonstrated that the application of an extremum seeking control algorithm [27] to a BIF converter-based G-gyrator makes possible an efficient and stable maximum power point tracking. It has been also shown that this algorithm can be efficiently adapted with the same purpose to a BOF converter-based R-gyrator. It has been experimentally verified the validity of both approaches by developing two battery chargers. Thus, a 12 V battery has been charged from a standard solar array (around 20 V of open circuit voltage) and by using a BIF converter-based G-gyrator as interface. Similarly, with the same PV array, a 24 V battery has been charged by means of a BOF converter-based R-gyrator. However, a Cuk converter-based G-gyrator with controlled input current has been proved to be the most versatile system for PV battery chargers. Due to its step-up or step-down characteristics, a Cuk converter-based G-gyrator with controlled input current can be used to charge indistinctly a 12 V or a 24 V battery from a standard solar array. Figure 5.3 shows the circuit scheme of this gyrator whose corresponding prototype is depicted in Figure 5.4.

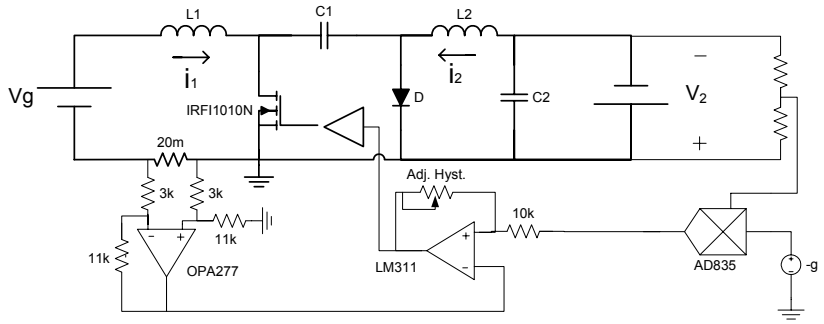

Fig.5.3 Circuit scheme of a Cuk converter-based G-gyrator with controlled input current.

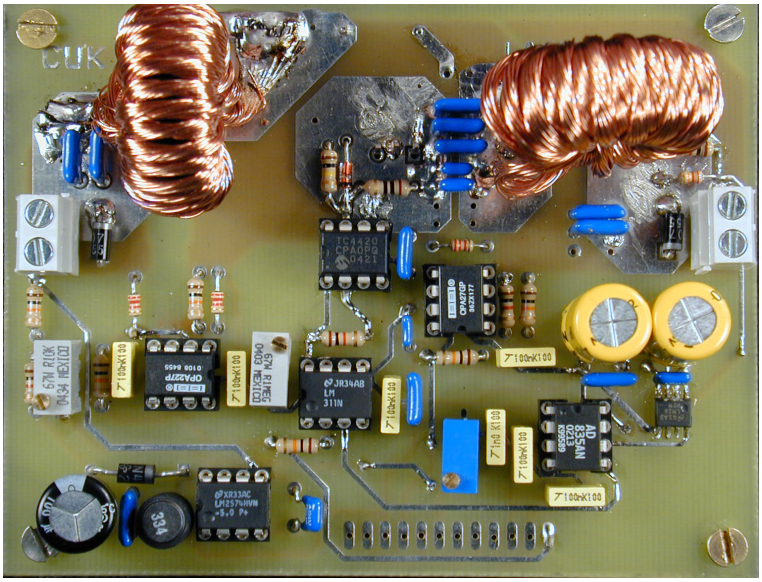

Fig.5.4 A 75 W Cuk converter-based G-gyrator with con trolled input current.

Voltage regulation by means of power gyrators has been also investigated. The regulation has been studied in the case of a single gyrator and for the parallel connection of the output ports of multiple gyrators. In both cases, a dynamic model of the voltage switching regulator has been established. With regard to voltage regulation based on gyrator paralleling, the stability of two transfer functions has been investigated namely, the regulator reference voltage to the regulator output voltage and the regulator reference voltage to any gyrator output current. Assuming democratic sharing in the internal current loops, it has been demonstrated that both transfer functions describe a stable system irrespective of the number of power gyrators in the parallel connection.

The experimental results of Chapter 4 have proved that voltage regulation based on the parallel connection of power G-gyrators is an efficient and robust solution of the design of paralleled converters with current sharing. Fig. 5.5 shows a prototype of BIF converter-based G-gyrator used in the paralleled connection of 3 power gyrators for voltage regulation.

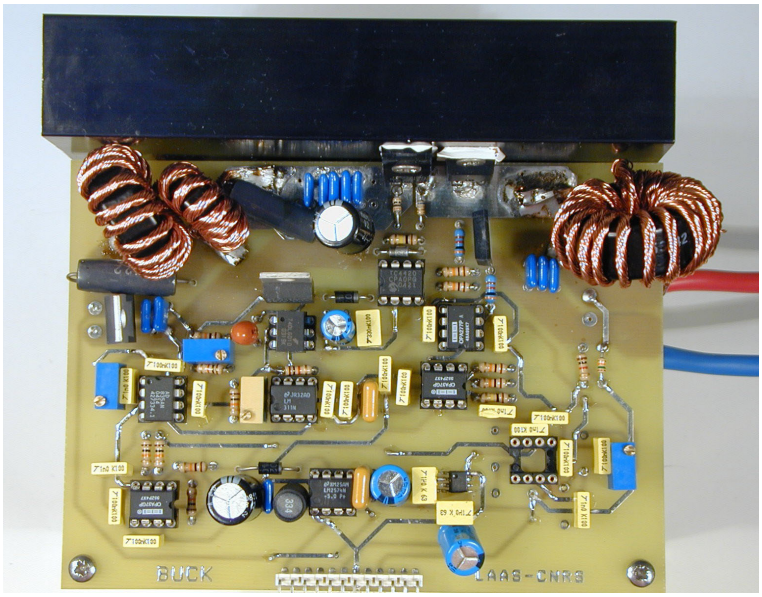

Fig.5.5 A 100 W BIF converter-based G-gyrator used in the gyrators paralleling

Figure 5.6 shows the final prototype corresponding to a voltage regulator based on the parallel connection of three G-gyrators of the type depicted in Fig. 5.5

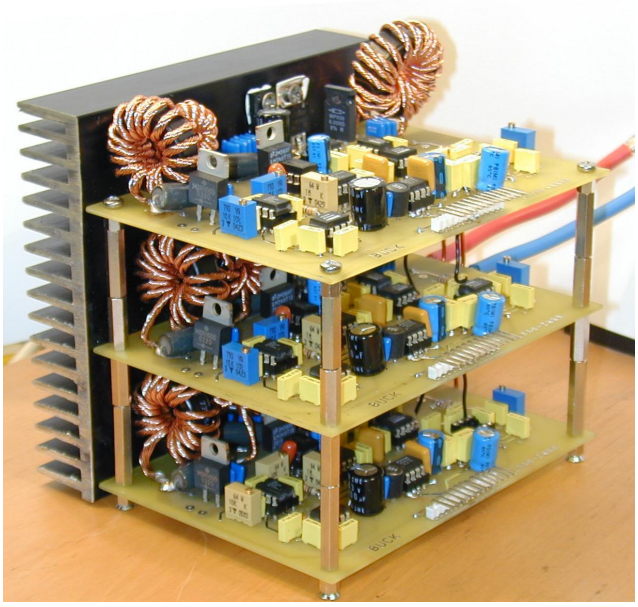

Fig.5.6 DC-to-DC switching regulation based on the parallel connection of 3 power G-gyrators with democratic current sharing

Thus far, the work done in this thesis has already included the classification and synthesis of power gyrators, analyses of the newly introduced gyrator structures, and their corresponding control schemes. In addition to the work in this thesis, the research that should continue in this area would be focused on the following targets: 1) the design of a gyrator-based DC to AC

conversion system, 2) the study of parallel connected gyrator-based inverters for high power applications, and 3) microelectronic realization of the main circuit blocks of a power gyrator.

The design of a power current source of sinusoidal type is an open problem. Although some realizations can be found in the technical literature, as for example, a bidirectional power gyrator based on two out of phase Cuk converters developed by Singer [8], no systematic studies concerning topology selection, stability analysis and efficiency measurement have been performed so far. Potential applications of such power structures are AC grid connection of the electric power produced by renewable energy sources, and the realization of AC buses for power distribution in vehicles.

In high power applications which supply large currents to the loads, power inverters can be connected in parallel at their outputs to form a distributive power system. The concept of uniform distribution of power flow among the inverter modules is very important for the reasons of cost effectiveness, long term reliability, and future expansion. However, in practice, these inverter modules may not have identical performance characteristics, this producing unbalance of currents drawn from the outputs. The modules delivering higher currents than the others will have their life-time shortened and degrade the system reliability. For these reasons, the current distribution control for parallel connected gyrator-based inverters has to be studied.

Finally, the last subject that needs to be considered as a future work is the microelectronic realization of the main circuit blocks of a power gyrator. The block diagram depicted in Figure 5.7 represents the circuits that could be integrated. Note that the system represented in Figure 5.7 could be used in the design of all types of gyrators, .i.e., G-gyrators, G-gyrators with controlled input current and R-gyrators. A voltage regulation loop could be added as in the microelectronic realization of a sliding-mode controller [36]

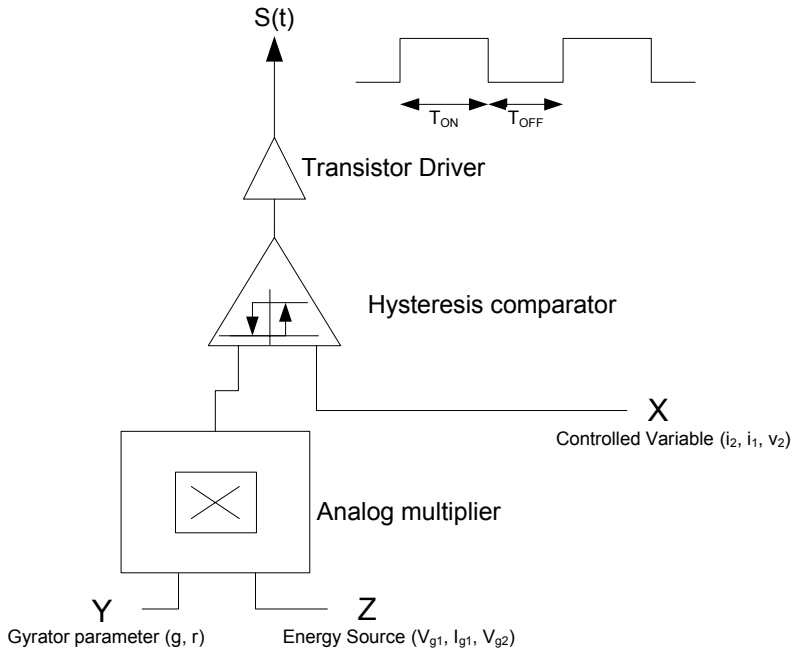

Fig.5.7 Gyrator circuit blocks suitable of microelectronic integration

6 REFERENCES

[1] Tellegen, BDH. "The gyrator, a new electric network element" Philips Res. Reports 3, pp81-101

[2] Hogan, C.L. "The ferromagnetic Faraday effect at microwave frequencies and its applications. The microwave gyrator" Bell Systems Technical Journal 31, pp 1-31, 1952

[3] Sharpe, G.E " The pentode gyrator" IRE Trans. On Circuit Theory, CT-4 pp 321-323, 1957

[4] Riordan, R.H.S "Simulated inductors using differential amplifiers" Electronic Letters 3, pp 30-51, 1967

[5] Voorman, J.O. "The gyrator as a monolithic circuit in electronic systems" Ph.D. Thesis, University of Nijmen, The Netherlands, 1977

[6] Miguel, J.M., "Contribución a la síntesis de giradores mediante "nulors". Método topológico y directo" Ph.D. Thesis, Polytechnic University of Catalonia, Barcelona, Spain, 1983 (In Spanish)

[7] Singer, S., "Gyrators application in power processing circuits" IEEE Trans. On Ind. Elect, vol IE-34, no 3, pp 313-318, 1987

[8] Singer, S., "Loss-free gyrator realization" *IEEE Transactions on Circuits and Systems*, Vol. 35, No.1, , pp 26-34, 1988

[9] Singer, S. and Erickson R. W., "Canonical modeling of power processing circuits based on the POPI concept", *IEEE Transactions on Power Electronics,* Vol. 7 , No.1, 1992, pp 37 – 43.

[10] Eshani, M., Husain, I., and Bilgic M.O., "Inverse Dual Converter (IDC) for High-Power DC-DC Applications" IEEE Trans. on Power Electronics, Vol. 8, No. 2, pp-216-223, 1993

[11] Eshani, M., Husain and Bilgic M.O., "Power converters as natural gyrators" IEEE Transactions on Circuits and Systems-I: Fundamental Theory and Applications, Vol. 40, No.12, pp 946-949, 1993

[12] Shmilovitz, D., Yaron, I., Singer, S. "Transmission-Line-Based Gyrator" *IEEE Transactions on Circuits and Systems*, Vol. 45, No. 4, 1998, pp 428-433.

[13] Venkataraman, R., "Sliding Mode Control of Power Converters", Ph.D. Dissertation, California Institute of Technology 1986

[14] Sira-Ramirez, H. "Sliding motions in bilinear switched networks" *IEEE Transactions on Circuits and Systems*, Vol. 34, No. 8, 1987, pp 919-933.

[15] Utkin, V.I. "Sliding Modes and Their Application in Variable Structure Systems" MIR, Moscow, 1974

[16] Itkis, U. "Control Systems of Variable Structure" John Wiley, New York 1976.

[17] Middlebrook, R.D. "Power Electronics: An Emerging Discipline" Advances in Switched-Mode Power Conversion, TESLAco, 1981, pp 11-15

[18] Middlebrook, R.D. "Design techniques for preventing input filter oscillations in switched-mode regulators" Advances in Switched-Mode Power Conversion, TESLAco, 1981

[19] Calvente, J., Martinez-Salamero, L., Garcés, P., and Romero, A., "Zero dynamics-based design of damping networks for switching converters" IEEE Transactions on Aerospace and Electronic Systems, Vol. 39, No. 4, pp 1292-1303, 2003

[20] Martinez L., Poveda A., Majo J., Garcia de Vicuña L., Guinjoan F., Marpinard J.C., and Valentin M., " Lie Algebras Modelling of Bidirectional Switching Converters" Proceedings of ECCTD'93, European Conference on Circuit Theory and Design, Davos, Switzerland, August 30 – September 3, 1993 pp 1425-1429

[21] Martinez L., Poveda A., Font J., Garcia de Vicuña L., Guinjoan F., Sanchez, A.F., Marpinard J.C., and Valentin M., " On the synthesis and control of bidirectional switching converters" Proceedings of PESC'93, Power Electronics Specialists Conference, Seatlle, WA, 1993 pp 197-202

[22] Calvente, J., "Control en modo deslizante aplicado a sistemas de acondicionamiento de potencia de satellites" Ph.D. Dissertation (In Spanish). Polytechnic University of Catalonia, Barcelona, Spain, 2001. Available at http://www.tdx.cesca.es

[23] Singer, S., "Switching networks for realization of variable DC transformers coupled to rectangular arrays" IEE Proceedings, Vol. 129 Pf G, No. 3, June 1982, pp 69-75

[24] Singer, S. and Braunstein A., " A general model of maximum power point tracking" Proceedings of MELECON'85 IEEE Mediterranean Electrotechnical Conference, Madrid, Spain pp 147-151

[25] Singer, S. and Braunstein A., " Maximum power transfer from a nonlinear energy source to an arbitrary load" IEEE Proceedings, Pt G, 1987 pp 1-7

[26] Singer, S., "Canonical Approach to Energy Processing Network Synthesis" IEEE Trans. On Circuits and Systems, Vol. 10, CAS-33, No. 8, August 1986 pp 767-774

[27] Leyva, R., Queinnec I., Alonso, C., Cid-Pastor, A., Lagrange D. and Martinez-Salamero L., " Maximum power point tracking of PV systems using extremum seeking control" IEEE Trans. on Aerospace and Electronic Systems. (Accepted for publication)

[28] Garabandic, D.S. and Petrovic T.B. "Modelling Parallel Operating PWM DC/DC Power Supplies" IEEE Trans. on Industrial Electronics, Vol 42, No. 5, October 1995 pp 545-551

[29] Thottuvelil V. J. and Verghese G.C., "Analysis and Control Design of Paralleled DC/DC Converters with Current Sharing" IEEE Transactions on Power Electronics, Vol 13, No. 4, July 1998, pp 635-644

[30] Ricart R., "Analsysis and design of a isolated power gyrator" Final Report, Industrial Electronics and Automatic Control Engineering, School of Electrical and Computer Engineering, Tarragona, Spain, 2004

[31] Capel A. and Barnaba A., "Evaluation of Bus Impedance on the Spot Multimission Platform" ESA Journal, 1983, Vol. 7, pp 277-298

[32] A. Cid-Pastor, L. Martínez-Salamero, C. Alonso, B. Estibals, J. Alzieu, G. Schweitz, and D. Shmilovitz , " Analysis and design of power gyrators in sliding-mode operation" IEE Proceedings Electric Power Applications Vol. 152, No. 4, July 2005, pp 821-826

[33] Cid-Pastor A., Alonso C., Estibals B., Lagrange D. and Martinez-Salamero L. "Automatic measurement system for testing photovoltaic conversion chains" IES, 2004. IECON 2004, 30th Annual conference of IEEE. Vol 3, 2-6 nov. 2004, Pusan, Korea, pp 3076-3081

[34] Cid-Pastor A., Alonso C., Cugat-Curto J.F., Estibals B. and Martinez-Salamero L. "Design of feedback control laws for dc-to-ac conversion in photovoltaic systems", AMC'04. The 8th IEEE International Workshop on Advanced Motion Control, 25-28 March 2004, Kawasaki, Japan, pp 93-98

[35] Martinez-Salamero L., Valderrama-Blave H., Giral R., Alonso, C. Estibals B., and Cid-Pastor, A." Self-Oscillating dc-to-dc switching converters with transformer characteristics" IEEE Trans. on Aerospace and Electronic Systems. Vol. 41, No.2 April 2005, pp 710-716

[36] Alarcón E., Romero A., Poveda A., Porta S. and Martinez-Salamero L. " Current-mode analogue integrated circuit for slidind-mode control of switching power converters" IEE Electronics Letters 31st January 2002 Vol. 38 No.3 pp 104-106, 2002

[37] Bábáa I.M.H., Wilson T.G. and Yu Y. "Analitic solutions of limit cycles in a feedback-regulated converter system with hysteresis" IEEE Trans. Autom. Contr., vol. AC-13, Oct. 1968, pp 524-531.

[38] Giral R., Martinez-Salamero L., Herranz J., Calvente J., Guinjoan F., Poveda A., and Leyva R. " Compensating networks for sliding-mode control". Proc. IEEE Int. Conf. on Circuits and Systems, ISCAS'95, pp. 2055-2058.

7 APPENDIX A

DESIGN OF A BIF CONVERTER-BASED G-GYRATOR

The expression of the characteristic equation of a BIF-converter-based G-gyrator is given by

$$\left(s+\frac{1}{RC_2}\right)P(s)=0$$

where

$$P(s)=s^3+\left(\frac{1}{R_dC_d}+\frac{1}{R_dC_1}-\frac{g^2R}{C_1}\right)s^2+\left(\frac{1}{L_1C_1}-\frac{g^2R}{R_dC_dC_1}\right)s+\frac{1}{L_1C_1R_dC_d} \tag{A.1}$$

If *P(s)* is written as $P(s)=s^3+m\,s^2+n\,s+p$, the polynomial will not have their roots in the right half-plane if the following conditions given by Routh's criterium, are fulfilled

$$\begin{aligned} &m>0\\ &n>0\\ &p>0\\ &mn-p>0 \end{aligned} \tag{A.2}$$

Applying conditions (A.2) to polynomial (A.1) results in

$$R_dC_d<\frac{C_1+C_d}{g^2R} \tag{A.3}$$

$$R_dC_d>g^2RL_1 \tag{A.4}$$

$$\frac{1}{L_1C_1R_dC_d}>0 \tag{A.5}$$

$$g^2R{R_d}^2{C_d}^2+g^2RL_1(C_1+C_d)<(g^4R^2L_1+C_d)R_dC_d \tag{A.6}$$

It can be observed that (A.5) is always accomplished. (A.3) and (A.4) establish the margin values of R_dC_d for a stable system. On the other hand, expression (A.6) can be expressed as follows

$$y=ax^2+bx+c<0 \tag{A.7}$$

where $x = R_dC_d$ and $a > 0$, $b < 0$ and $c > 0$.

Therefore (A.7) can be expressed as

$$y=g^2R\,x^2+(g^4R^2L_1+C_d)\,x+g^2RL_1(C_1+C_d)<0 \tag{A.8}$$

Equation (A.7) is depicted in figure A.1 where X_1 and X_2 are given by

$$x_1 = \frac{-b - \sqrt{b^2 - 4ac}}{2a} \qquad x_2 = \frac{-b + \sqrt{b^2 - 4ac}}{2a} \tag{A.9}$$

and

$$x_1 < \frac{-b}{2a} < x_2 \tag{A.10}$$

which leads to

$$x_1 < \frac{g_2 R L_1}{2} + \frac{C_d}{2g^2 R} < x_2 \tag{A.11}$$

$$\min(R_d C_d) < \frac{g_2 R L_1}{2} + \frac{C_d}{2g^2 R} < \max(R_d C_d) \tag{A.12}$$

Also, we can write

$$R_d C_d < \frac{C_1 + C_d}{g^2 R} \tag{A.13}$$

$$R_d C_d > g^2 R L_1 \tag{A.14}$$

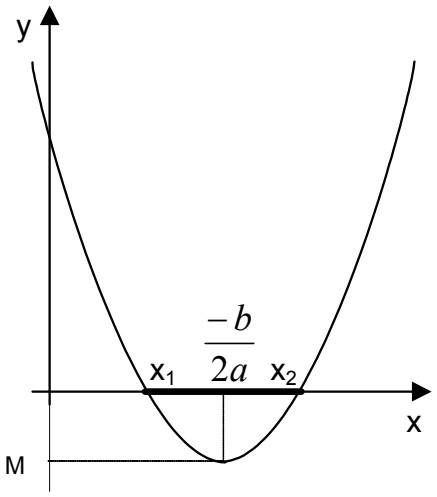

Fig.A.1 Generic representation of function (A.8)

Bounds (A.11) –(A.14) are summarized in Fig. A.2.

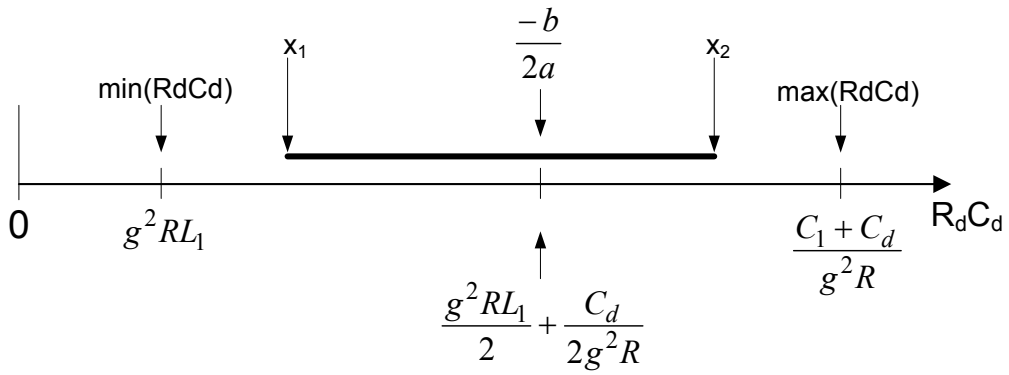

Fig.A.2 Stability region in terms of R_dC_d

Moreover, the term $\frac{\sqrt{b^2-4ac}}{2a}$ is given by

$$\frac{\sqrt{b^2-4ac}}{2a}=\frac{\sqrt{\left(g^4R^2L_1+C_d\right)^2-4g^4R^2L_1(C_1+C_d)}}{2g^2R}= \tag{A.15}$$

$$=\frac{\sqrt{g^8R^4{L_1}^2+{C_d}^2+4g^4R^2L_1C_1-2g^4R^2L_1C_d}}{2g^2R}$$

(A.15) can be simplified by assuming

$${C_d}^2=4g^4R^2L_1C_1-2g^4R^2L_1C_d \tag{A.16}$$

which results in

$$C_d=g^4R^2L_1+\sqrt{g^8R^4{L_1}^2+4g^4R^2L_1C_1} \qquad C_d>0 \tag{A.17}$$

Assuming C_d given by (A.17) results in the following values for X_1 and X_2

$$\begin{aligned} x_1&=\frac{C_d}{2g^2R} \\ x_2&=g^2RL_1+\frac{C_d}{2g^2R} \end{aligned} \tag{A.18}$$

It is derived from (A.18) that

$$\min(R_dC_d)<x_1 \quad and \quad x_2<\max(R_dC_d) \tag{A.19}$$

The previous analysis can be summarized in a design algorithm as depicted in the flowchart of Fig. A.3.

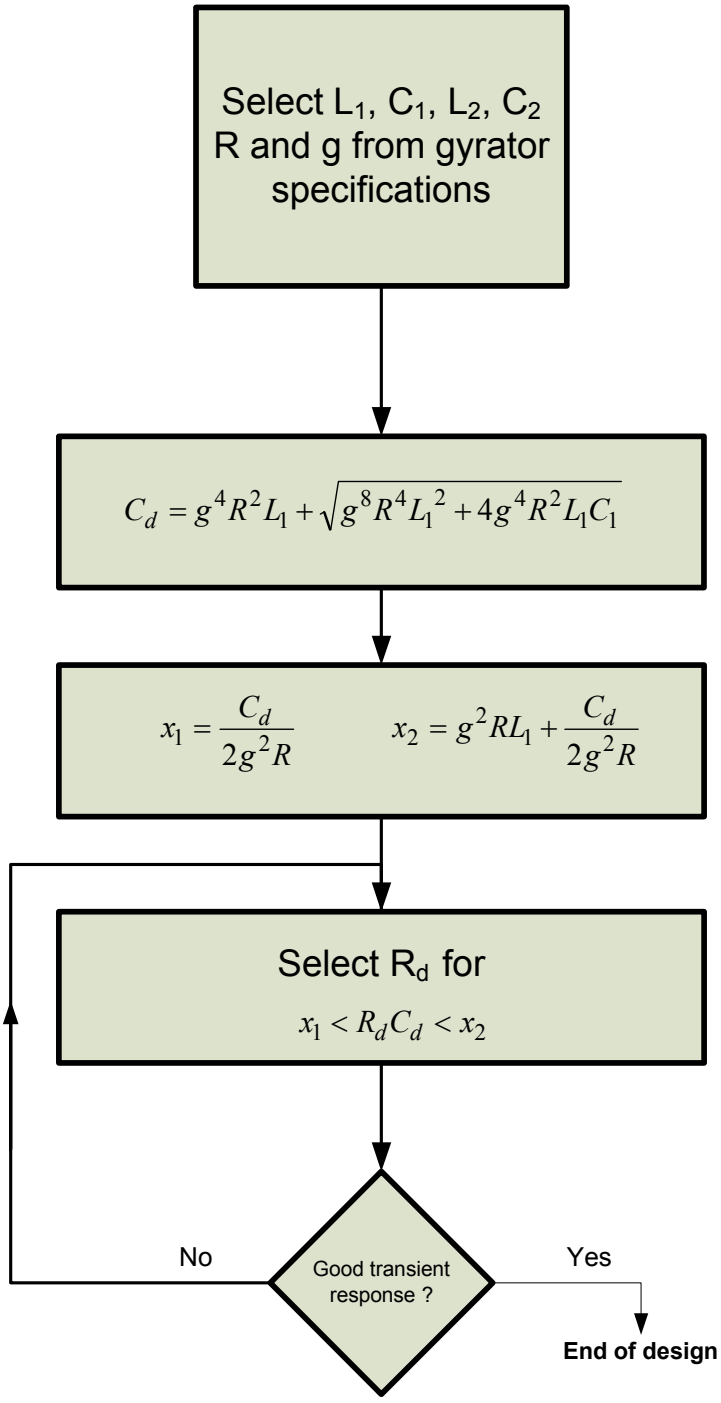

Fig.A.3 Design algorithm for R_d and C_d in a BIF converter-based G-gyrator

8 APPENDIX B

DESIGN OF A CUK CONVERTER-BASED G-GYRATOR

The expression of the characteristic equation of a Cuk-converter-based G-gyrator is given by

$$\left(s+\frac{1}{RC_2}\right)P(s)=0$$

where

$$P(s)=s^3+\left(\frac{1}{R_dC_d}+\frac{1}{R_dC_1}-\frac{g^2R}{C_1(gR+1)}\right)s^2+\left(\frac{1}{L_1C_1(gR+1)}-\frac{g^2R}{R_dC_dC_1(gR+1)}\right)s+\frac{1}{L_1C_1R_dC_d(gR+1)} \tag{B.1}$$

Applying the Routh's criterium results in the following stability conditions

$$R_dC_d<\frac{(C_1+C_d)(1+gR)}{g^2R} \tag{B.2}$$

$$R_dC_d>g^2RL_1 \tag{B.3}$$

$$\frac{1}{L_1C_1R_dC_d(gR+1)}>0 \tag{B.4}$$

$$g^2R{R_d}^2{C_d}^2+g^2RL_1(C_1+C_d)(1+gR)<(g^4R^2L_1+C_d(1+gR))R_dC_d \tag{B.5}$$

Using a similar procedure to that developed in Appendix A leads to the design algorithm depicted in Fig. B.1

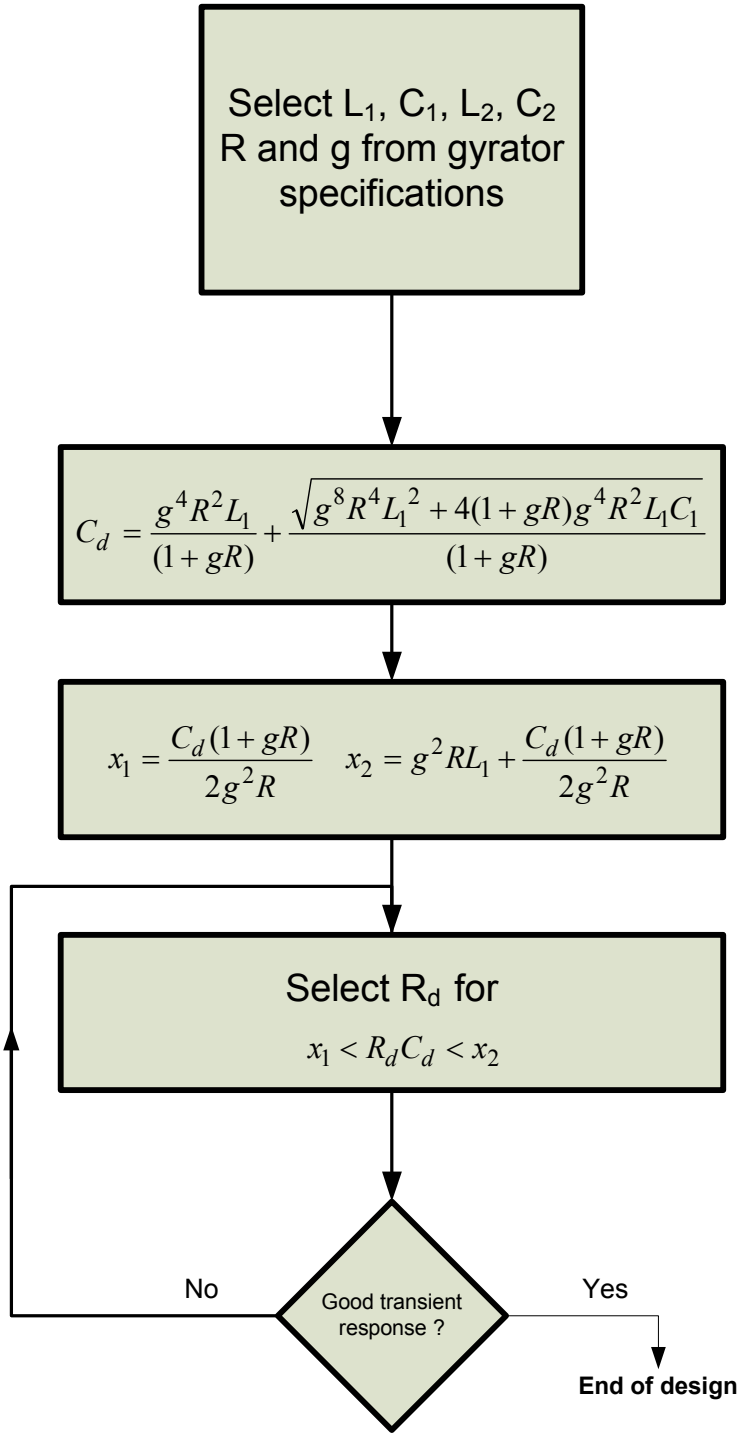

Fig.B.1 Design algorithm for R_d and C_d in a Cuk converter-based G-gyrator

9 APPENDIX C

EXTREMUM SEEKING CONTROL

The block diagram of an extremum seeking problem is depicted in Fig. C.1. The equations describing the system behavior are given as follows

$$\frac{dx}{dt} = K\varepsilon \tag{C.1}$$

where $\varepsilon = \pm 1$ and K is a constant

$$g = \frac{dy}{dt} \tag{C.2}$$

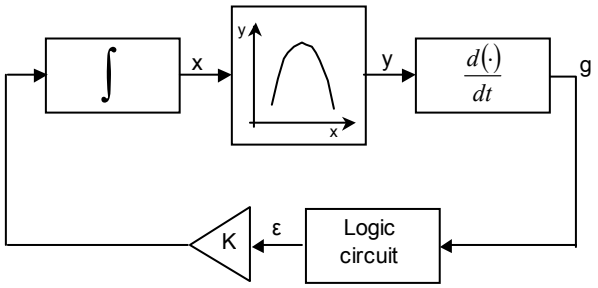

Fig.C.1 Block diagram of an extremum seeking control system

The logic circuitry subsystem implements the following function:

$$\left.\begin{array}{l}\text{Change instantaneously the sign of K if } g < 0\\ \text{Keep the sign of K if } g > 0\end{array}\right\} \tag{C.3}$$

Taking into account (C.1)-(C.3), four cases can be considered

$$\left.\frac{dx}{dt}\right|_{t^+} = K \;\; if \;\; \left.\frac{dy}{dt}\right|_{t^-} < 0 \;\; and \;\; \left.\frac{dx}{dt}\right|_{t^-} = -K \tag{C.4}$$

$$\left.\frac{dx}{dt}\right|_{t^+} = K \;\; if \;\; \left.\frac{dy}{dt}\right|_{t^-} > 0 \;\; and \;\; \left.\frac{dx}{dt}\right|_{t^-} = K \tag{C.5}$$

$$\left.\frac{dx}{dt}\right|_{t^+} = -K \;\; if \;\; \left.\frac{dy}{dt}\right|_{t^-} < 0 \;\; and \;\; \left.\frac{dx}{dt}\right|_{t^-} = K \tag{C.6}$$

$$\left.\frac{dx}{dt}\right|_{t^+} = -K \;\; if \;\; \left.\frac{dy}{dt}\right|_{t^-} > 0 \;\; and \;\; \left.\frac{dx}{dt}\right|_{t^-} = -K \tag{C.7}$$

where t^- and t^+ correspond to instants of analysis and decision of the logic subsystem respectively.

Since $\frac{dy}{dx} = \frac{dy/dt}{dx/dt}$, (C.4)-(C.7) can be expressed in compact form as follows

$$\left.\frac{dx}{dt}\right|_{t^+} = K \;\; if \;\; \left.\frac{dy}{dx}\right|_{t^-} > 0 \tag{C.8}$$

$$\left.\frac{dx}{dt}\right|_{t^+} = -K \;\; if \;\; \left.\frac{dy}{dx}\right|_{t^-} < 0 \tag{C.9}$$

Equations (C.8) and (C.9) can be also reduced to only one expression

$$\frac{dx}{dt} = K\, sign\left(\frac{dy}{dx}\right) \tag{C.10}$$

It can be observed in (C.10) that the equilibrium point $\frac{dx}{dt} = 0$ will correspond to an extremum of the *y-x* curve in Fig. C.1, where $\frac{dy}{dx} = 0$. Note also in (C.10) that the system dynamics change with constant slope, which can be either positive or negative, this depending on the sign of the slope of the *y-x* curve.

In order to demonstrate that the equilibrium point is stable, a positive definite function *V(t)* is defined in a concave domain of *y(x)*

$$V(t) = \frac{1}{2}\left(\frac{dy}{dx}\right)^2 \tag{C.11}$$

Hence

$$\dot{V}(t) = \frac{dy}{dx}\frac{d^2y}{dx^2}\frac{dx}{dt} = \frac{dy}{dx}\frac{d^2y}{dx^2}\left(K\, sign\left(\frac{dy}{dx}\right)\right) \tag{C.12}$$

The concavity of *y(x)* implies

$$\frac{d^2y}{dx^2} < 0 \tag{C.13}$$

On the other hand,

$$\frac{dy}{dx}\, sign\left(\frac{dy}{dx}\right) > 0 \tag{C.14}$$

Therefore, choosing a positive value for *K* will imply *V'(t)<0*, i.e., a negative definite function, which demonstrates the global stability of the system given by (C.10).

Since the *v-p* characteristics of a solar array is a concave function, the previous analysis can be applied to solve the problem of maximum power point tracking [27].

10 APPENDIX D

PWM ZERO-DYNAMICS-BASED NONLINEAR CONTROL

In the continuous conduction mode, the average value of the converter state vector $\overline{X}$ satisfies the following bilinear equation

$$\dot{\overline{X}} = \Gamma\left(\overline{A_1 X + b_1 V_g}\right) + (1-\Gamma)\left(\overline{A_2 X + b_2 V_g}\right) \qquad \text{(D.1)}$$

where the symbol (—) stands for average value and $A_1 X + b_1 V_g = \dot{X}$ during T_{ON} and $A_2 X + b_2 V_g = \dot{X}$ during T_{OFF}.

Γ is the converter duty cycle and $\overline{X}^+ = \left[\overline{X}_1, \overline{X}_2, \ldots, \overline{X}_n\right]$ where $\overline{X}_1, \overline{X}_2, \ldots, \overline{X}_n$ represent respectively the average values of the state vector components $x_1, \ldots, x_n$.

To derive the control strategy, we choose the averaged state variable $\overline{X}_1$ which can lead the whole set of variables to a stable equilibrium point following the dynamics

$$\dot{\overline{X}}_1 = -\alpha\left(\overline{X}_1 - \overline{X}_1^*\right) \qquad \alpha > 0 \qquad \text{(D.2)}$$

where $\overline{X}_1^*$ is the reference signal to be reached by $\overline{X}_1$ in the equilibrium and $1/\alpha$ is the time constant that measures the convergence process. The application of this technique to second and fourth order non-isolated converters reveals that one stable equilibrium point can be reached as depicted in Table D.I where the corresponding control law is also represented. As shown in the same table, similar conclusions are derived from the use of sliding mode control taking the constant of the discontinuity surface $\overline{X}_1^*$.

The comparison between Γ and the equivalent control in the sliding-mode shows that the expression of the nonlinear continuous PWM control in the equilibrium point is exactly the equivalent control u_{eq}. The expression of Γ has an additional term which takes into account the transient regime previous to the steady-state. This additional term constitutes the main advantage of the nonlinear continuous PWM nonlinear control with respect to the sliding mode control. In the sliding case there is no information in the closed-loop model about the transient regime that takes place between the converter start-up and the instant in which the controlled variable reaches the discontinuity surface [20].

TABLE D.I

Converter	SLIDING MODE CONTROL		NONLINEAR PWM CONTROL	
	Sliding Control	u_{eq}	Decoupled variable dynamics	Γ
BUCK	S(x) = i – K u = 1 S(x) < 0 u = 0 S(x) > 0	$\frac{v}{V_g}$	$\dot{I}_L = -\alpha(I_L - I_L^*)$	$\frac{V_{CO} - L\alpha(I_L - I_L^*)}{v_g}$
BOOST	S(x) = i – K u = 1 S(x) > 0 u = 0 S(x) < 0	$\frac{v - V_g}{V_g}$	$\dot{I}_L = -\alpha(I_L - I_L^*)$	$\frac{V_{CO} - V_g + L\alpha(I_L - I_L^*)}{v_g}$
BUCK-BOOST	S(x) = i – K u = 1 S(x) > 0 u = 0 S(x) < 0	$\frac{v}{v + V_g}$	$\dot{I}_L = -\alpha(I_L - I_L^*)$	$\frac{V_{CO} + L\alpha(I_L - I_L^*)}{v_g}$
BIF	S(x) = v_{C1}-V_g u = 1 S(x) > 0 u = 0 S(x) < 0	$\frac{i_{L1}}{i_{L2}}$	$\dot{V}_{C1} = -\alpha(V_{C1} - V_{C1}^*)$	$\frac{I_{L1} + \alpha C_1(V_{C1} - V_{C1}^*)}{I_{L2}}$
BOF	S(x) = i_{L1} – K u = 1 S(x) < 0 u = 0 S(x) > 0	$\frac{v_{C1} - V_g}{v_{C1}}$	$\dot{I}_{L1} = -\alpha(I_{L1} - I_{L1}^*)$	$\frac{V_{C1} - V_g + \alpha L_1(I_{L1} - I_{L1}^*)}{V_{C1}}$
CUK	S(x) = i_{L1} – K u = 1 S(x) < 0 u = 0 S(x) > 0	$\frac{v_{C1} - V_g}{v_{C1}}$	$\dot{I}_{L1} = -\alpha(I_{L1} - I_{L1}^*)$	$\frac{V_{C1} - V_g + \alpha L_1(I_{L1} - I_{L1}^*)}{V_{C1}}$
SEPIC	S(x) = i_{L1} – K u = 1 S(x) < 0 u = 0 S(x) > 0	$\frac{v_{C1} + v_{CO} - V_g}{v_{C1} + v_{CO}}$	$\dot{I}_{L1} = -\alpha(I_{L1} - I_{L1}^*)$	$\frac{V_{CO} + V_{C1} - V_g + \alpha L_1(I_{L1} - I_{L1}^*)}{V_{CO} + V_{C1}}$

VITA

NAME: Angel Cid-Pastor

EDUCATION: B. Eng., Enginyeria Tecnica Industrial en Electronica Industrial, Rovira i Virgili University, Tarragona, Spain, December 1999.

M.S. (with honors), Enginyeria Superior en Automatica I Electronica Industrial, Rovira i Virgili University, Tarragona, Spain, September 2002.

D.E.A. Conception de Circuits Microélectroniques et Microsystèmes, Institut National des Sciences Appliquées, Toulouse, France, July 2003.

TEACHING: Teaching Assistant, IUT Genie Civil, Paul Sabatier University, Toulouse , France 2003-2005

RESEARCH: Research Assistant, GAEI-ETSE-URV Tarragona, Spain, 1999-2002
Research Assistant, CIP, LAAS-CNRS, Toulouse, France 2002-2005
Research Assistant, LME, EDF R&D, Moret Sur Loing, France, 2002-2005

SCHOLARSHIPS: "1999 Dermot O'Sullivan Power Electronics Project", Sponsored by the European Space Agency. Research performed in the laboratory of Industrial Electronics and Automatic Control of ETSE-URV during the period January-July 1999.

PUBLICATIONS:

Journal papers:

A. Cid-Pastor, L. Martínez-Salamero, C. Alonso, B. Estibals, J. Alzieu, G. Schweitz, and D. Shmilovitz , " Analysis and design of power gyrators in sliding-mode operation" IEE Proceedings Electric Power Applications, Vol. 152, No. 4, July 2005, pp 821-826

Martinez-Salamero L., Valderrama-Blave H., Giral R., Alonso, C. Estibals B., and Cid-Pastor, A." Self-Oscillating dc-to-dc switching converters with transformer characteristics" IEEE Trans. on Aerospace and Electronic Systems. Vol 41, No. 2 April 2005, pp 710-716

Leyva, R., Queinnec I., Alonso, C., Cid-Pastor, A., Lagrange D. and Martinez-Salamero L., " Maximum power point tracking of PV systems using extremum seeking control" IEEE Trans. on Aerospace and Electronic Systems. (Accepted for publication)

J. Maixe, L. Martinez-Salamero, R. Leyva, E. Vidal-Idiarte and A. Cid-Pastor, "Resonant Converter with Inherent Short-Circuit Protection" IEEE Trans. on Circuits and Systems II, TCAS-II, Vol. 52, Issue 6, June 2005, pp 313-316

R. Leyva, A. Cid-Pastor, C. Alonso, I Queinnec, S. Tarbouriech and L. Martinez-Salamero, "Passivity-Based Integral control of a boost converter for Large-signal stability", IEE Proc. Control Theory & Applications (Accepted for publication).

Conference papers:

Cid-Pastor A., Alonso C., Cugat-Curto J.F., Estibals B. and Martinez-Salamero L. "Design of feedback control laws for dc-to-ac conversion in photovoltaic systems", AMC'04. The 8th IEEE International Workshop on Advanced Motion Control, 25-28 March 2004, Kawasaki, Japan, pp 93-98

Cid-Pastor A., Alonso C., Estibals B., Lagrange D. and Martinez-Salamero L. "Automatic measurement system for testing photovoltaic conversion chains" IES, 2004. IECON 2004, 30th Annual conference of IEEE. Vol 3, 2-6 nov. 2004, Pusan, Korea, pp 3076-3081

A. Cid-Pastor, L. Martínez-Salamero, C. Alonso, J. Calvente and G. Schweitz, "Synthesis of PWM-Based Power Gyrators" IEEE Int. Symposium on Ind. Elect. ISIE 2005 June 20-23 2005, Dubrovnik Croatia.

A. Cid-Pastor, L. Martinez-Salamero, C. Alonso, R. Leyva and J. Calvente, "Seguimiento del punto de maxima potencia de un panel fotovoltaico mediante giradores" SAAEI 2005, Seminario Anual de Automática, Electrónica Industrial e Instrumentacion, Santander, Septembre 2005 (Accepted for publication) (In Spanish)

A. Cid-Pastor, L. Martinez-Salamero, C. Alonso and B. Estibals, "Analisis y diseno de giradores de potencia en modo deslizante" Actas del SAAEI-EPF 2004, Seminario Anual de Automática, Electrónica Industrial e Instrumentacion- Electronique de Puissance du Futur, Toulouse, Septembre 2004 (In Spanish)

R. Leyva, C. Alonso, I. Queinnec, Cid-Pastor A. and L. Martinez-Salamero, "Analisis mediante Lyapunov de un MPPT en paneles fotovoltaicos » Actas del SAAEI-EPF 2004, Seminario Anual de Automática, Electrónica Industrial e Instrumentacion- Electronique de Puissance du Futur, Toulouse, Septembre 2004 (In Spanish)

H. Valderrama-Blavi, C. Alonso, L. Martínez-Salamero, M. F. Shraif, A. Cid-Pastor, R. Pedrola, J. Calvente, 'Multilevel Inverters Adapted to Photovoltaic Energy conversion' Proceedings of EPE-PEMC 2002 Dubrovnik & Cavtat, 2002.

V. Boitier, C. Alonso, D. Lagrange, D. Medale, P. Marcoul, A. Cid-Pastor, G. Schweitz, J. Alzieu. 'Chargeurs de Batterie Solaire: Mesures des rendements'.V. Boitier, C. Alonso, Proceedings of EPF-2002, Montpellier November 2002. (In French)